Remote Sensing of Water Vapour in Venus' Middle Atmosphere

Mary Elizabeth Koukouli

St Peter's College

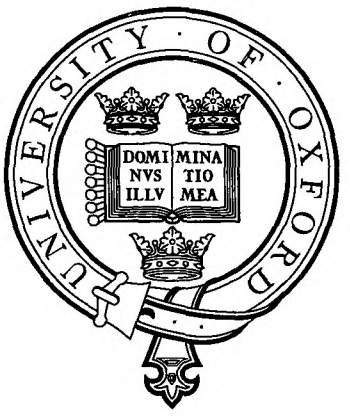

A thesis submitted to the Faculty of Physical Sciences for the degree of Doctor of Philosophy in the University of Oxford.

Michaelmas Term 2002

Remote Sensing of Water Vapour in Venus' Middle Atmosphere

A thesis submitted to the Faculty of Physical Sciences for the degree of Doctor of Philosophy in the University of Oxford by M. E. Koukouli, St Peter's College, Michaelmas Term 2002.

Abstract

The *Pioneer Venus Orbiter Infrared Radiometer* and *Venera 15 Fourier Transform Spectrometer* observations of thermal emission from Venus' middle atmosphere between 10°S and 50°N were used to determine global maps of temperature, cloud optical depth and water vapour abundance. The spectral regions observed include the strong 15 μm carbon dioxide band and the 45 μm fundamental rotational water band. The main aim of this thesis is to reconcile the water vapour abundance results from these two sets of observations reported in previous studies. New radiative transfer and retrieval models have been developed for this purpose based on new correlated-k absorption tables calculated with up-to-date spectral line data. The H_2SO_4 cloud opacity and scattering properties have been recalculated from new refractive index data using Mie theory.

For the first time these two sets of observations have been analysed using the same retrieval tools. From the *Pioneer Venus Orbiter Infrared Radiometer* observations we report a high abundance of water vapour in the early afternoon at the equatorial cloud-top region and a strong day-night variability in the cloud-top pressure. From the *Venera 15 Fourier Transform Spectrometer* observations we report medium local variability in water vapour abundance, with highest values in the near-equatorial region and slight decrease towards the polar region.

It is found that serious constraints are placed on the validation of the retrievals by the lack of adequately accurate H_2SO_4 optical properties data in the shorter wavelengths and by the poor vertical resolution when sensing the complex but interesting cloud region which prohibits its rigorous modelling. The proposed European Space Agency *Venus Express* mission will carry a number of high resolution infrared and UV instruments that will shed new light to the interesting question of water vapour abundance in Venus' middle atmosphere.

To Ingo

ett stort tack för ditt oändliga tålamod,
ständiga stöd och aldrig sviktande käreksfulla
tillgivenhet under tre år.

Acknowledgements

Contrary to tradition, I thank the most important people of all first; my three parents, **Irini, Dimitris and Zaza** who have shaped me into who I am and without whose constant support, encouragement and unfailing trust from day one of my life I would not be here today. You are the most wonderful and important people in my life and I look forward to many more years together with you!

I would then like to thank the following people, inside and outside AOPP; the **Bodossaki Foundation** and in particular **Dr Mantzavinos and Dr Vlastos** whose generosity has permitted me to spend three years working on my thesis unhindered by financial worries. **Patrick Irwin** for supervising the first two years of my D.Phil., for having a clear project ready for my attention upon arrival and for sharing his radiative transfer knowledge. **Fred Taylor** for supervising my first and third years here, for always being keen to share his vast knowledge on Venus with me and for being prompt in reading and correcting this thesis. Everyone at St Peter's College, in particular the Master, **Prof J P Baron**, the Bursar, **Dr C D Daukes** and the Tutor for Graduates, **Dr Gavin Williams** for helping me financially to present my work at conferences and advance my research. **Vassily Moroz, Ludmilla Zasova and Nikolai Ignatiev** for trusting me with the Venera 15 FTS spectra and for answering all my inexperienced questions without delay.

Many many heartfelt and grateful thanks to **Anu Dudhia**, *locum* supervisor, for never failing to answer a question, small or big, with the same spicy humour. My gratitude to the **EODG** group for their willingness to be educated on the world of Venus and for allowing me to participate in their weekly meetings. *Mille grazie* to **Chiara Piccolo** for her constant sisterly support and her hawk's eye with mistakes in this thesis. *Merci* to **Thierry Fouchet** for also reading this thesis and asking all the difficult, albeit fair, questions. **Colin Wilson** merits a whole phrase to himself, for he put up with my moods and grievances and short periods of lucid happiness "when the darn code worked", and managed to faithfully share an office with me for three long years. *Ευχαριστώ πολύ* to a number of Oxford-based friends, and most especially **Manolis** and **Marianna** for putting up with my constant whinging and for always offering a shoulder for me to lean on. Space prevents me from thanking all the friends whose frequent contact with news from home proved a useful anchor in times of great dizziness and disillusionment with this D.Phil. Among these, **Christina** shines through her willingness to move along with the technological times and to stay constantly in touch during my seven years in the U.K.

Foreword

The work described in this thesis has been performed by myself during three academic years I have spent in the Atmospheric, Oceanic and Planetary Physics subdepartment of Oxford University, starting in October 1999 and ending in September 2002. As a personal preference and for purely aesthetic reasons, the personal pronoun **I** is not used in this thesis, even though I obviously worked on this thesis alone. Where it could not be avoided, the personal pronoun **we** is preferred instead. More often than not however **we** was used to signify that both reader and writer should focus their attention on a specific point or result.

The computer code used to analyse the *Pioneer Venus Orbiter Infrared Radiometer* and *Venera 15 Fourier Transform Spectrometer* measurements is based on a rich deposit of `FORTRAN 77` routines developed over the years by numerous members of the Planetary Atmospheres Group, most notably Simon Calcutt and Patrick Irwin. This vast library of radiative transfer analysis tools, known as `Radtran`, was utilised as a starting point only. In the following, a short summary of my precise input to this thesis is given.

The initial data reduction of both *Pioneer Venus Orbiter Infrared Radiometer* and *Venera 15 Fourier Transform Spectrometer* observations was performed by me, as well as the diagnostic analysis on the information content of the data and the confirmation on the data-reduction choices. The forward model used to simulate the thermal radiance emitted from Venus' middle atmosphere was adapted to Venus' conditions, notably to agree with temperature, cloud and optical depth requirements. I created special correlated-k tables in order to calculate the transmittance of the gaseous species in Venus' atmosphere. I also performed an extensive search for data on the H_2SO_4 optical properties in the infrared range, paramount for the calculation of the transmittance of the H_2SO_4 Venus cloud. The disappointing realisation that no modern measurements exist for optical properties around 45μm led to the necessary retrieval of correction coefficients for the cloud extinction parameters. The aerosol correction coefficients retrieval algorithm was written and executed by myself. The main retrieval algorithm I used in conjunction with the adapted forward model is based on the theory of another member of the Atmospheric Physics group, Clive Rodgers. I wrote and performed all post-retrieval error analysis in `IDL`.

The final interpretation of the results and physical explanations are my own.

Contents

Abstract i

Acknowledgements iii

Foreword iv

1 Introduction 1

1.1 The Planet Venus; A General Introduction 4

1.2 The Atmosphere of Venus 9

1.3 The Sulphuric Acid Clouds of Venus 13

1.4 Winds on Venus 17

1.5 Overview and Main Aim of this Thesis 19

2 Water Vapour in Venus' Middle Atmosphere 21

2.1 Remote sensing measurements from the Earth 22

2.2 Remote sensing measurements from Satellites 23

2.3 *In Situ* measurements 26

2.4 Remote sensing measurements from *PV OIR* and *Venera 15* 32

2.5 Synopsis 35

3 The Pioneer Venus OIR and Venera 15 FTS Instruments 38

3.1 *Pioneer Venus Orbiter Infrared Radiometer* 39

3.2 *Venera 15 Fourier Transform Spectrometer* 43

3.3 Synopsis 49

4 Joint Retrievals: Theory And Methodology **52**

4.1 Radiative Transfer Equation 53

4.2 The Atmospheric Model 55

4.2.1 Molecular Absorption Coefficient Calculation 59

4.2.2 Cloud Absorption Coefficient Calculation 66

4.2.3 Synopsis of presented material 67

4.3 The Forward Model 68

4.4 The Retrieval Method 70

4.4.1 Optimal Estimation Retrieval Technique 70

4.4.2 Error Analysis and Formalisms 75

4.4.3 Diagnostic Tools 81

4.4.4 Aerosol Correction Coefficient Retrieval 91

4.5 Synopsis 98

5 Joint Retrievals: Results **100**

5.1 *PV OIR* Results 100

5.2 *Venera 15* Results 107

5.3 Joint Results 119

5.4 Validation of Results 121

5.5 Synopsis 129

6 Physical Explanations **130**

6.1 Introduction 131

6.2 The existence of wet spots 132

6.2.1 The presence of H_2O and SO_2 133

6.2.2 Convection and other dynamical effects 135

6.3 The disappearance of wet spots 136

6.4 Venus' cloud revisited 140

6.5 Synopsis 143

7 Conclusions **145**

7.1 Synopsis 145

7.2 Limitations 147

7.3 The Future 148

A A priori Information **150**

A.1 The importance of *a priori* information revealed 152

B Radiative Transfer and Retrieval Equations **154**

B.1 Levenberg-Marquard Method 154

B.2 Different retrieval methods 155

C Line Strengths **158**

List of Figures

1.1 Venera 13 lander images of the surface of Venus. 6

1.2 Colour-coded topographic map of Venus from Magellan radar observations (NASA.) 7

1.3 M. V. Lomonosov (1711-1765), the discoverer of Venus' atmosphere. . 9

1.4 Vertical profiles of temperature vs. pressure at 30°N latitude, as measured on Venus by *PV OIR* and on Earth by Nimbus 7. Adapted from Houghton et al. (1984). 11

1.5 Temperatures above the clouds derived from three Pioneer probes and Venera 11 and 12. Adapted from Seiff (1983). 11

1.6 Vertical structure of the Venus cloud system as in Knollenberg and Hunten (1980). 15

1.7 Venus' sulphur cycle, by Carter Emmart, as seen in Grinspoon (1997). 16

1.8 Longitudinally averaged retrograde zonal wind velocities vs latitude. (Adapted from Schubert (1980).) 18

2.1 Water vapour abundance in Venus' atmosphere vs altitude. 27

2.2 Variation of water vapour abundance with spectral region investigated. 30

2.3 Global coverage of Venus' disk by spacecraft and Earth-based studies 31

2.4 Temperature, cloud and water vapour retrievals as in Schofield et al. (1983). 33

2.5 Water vapour mixing ratios vs latitude and local solar time, as in Ignatiev et al. (1999). 37

3.1 The Pioneer Venus Orbiter revolving around Venus (artist's impression.) 39

3.2 *PV OIR* planetary coverage. 42
3.3 The Venera 15 orbiter. 44
3.4 *Venera 15* FTS planetary coverage. 45
3.5 *Venera 15* on-board and on-Earth averaged spectra. 46
3.6 Viewing angle distribution of the *Venera 15* on-board spectra with latitude. 48
3.7 Viewing angle distribution of the *Venera 15* on-Earth spectra with latitude. 48

4.1 Temperature and pressure *a priori* profiles vs altitude (km). 56
4.2 Atmospheric gases volume mixing ratio and aerosol concentration profiles vs altitude. 57
4.3 Theoretical and experimental transmission function calculations for H_2O as seen in Schofield et al. (1983). 65
4.4 Schematic representation of the iterative retrieval process employed. . 75
4.5 Retrieval diagnostics and example for the *PV OIR* case study. 78
4.6 Retrieval diagnostics and example for the on-board *Venera 15* case study. 79
4.7 Investigation into possible forward modelling errors in the *Venera 15* spectra. 82
4.8 Degrees of freedom for chosen spectral points of a random on-board *Venera 15* spectrum. 86
4.9 Information content and degrees of freedom of a random on-board *Venera 15* spectrum. 86
4.10 Degrees of freedom for chosen spectral points of a random on-Earth *Venera 15* spectrum. 87
4.11 Information content and degrees of freedom of a random on-Earth *Venera 15* spectrum. 87
4.12 Example temperature retrieval from the *PV OIR* measurements. . . . 90
4.13 Example temperature retrieval from the *Venera 15* measurements. . . 90

4.14 Refractive index data of Jones (1976), Palmer and Williams (1975) and Biermann et al. (2000). 93
4.15 Mie theory calculations of single scattering cross-sections. 95
4.16 Original and corrected cloud extinction cross-sections. 96

5.1 *PV OIR* temperature retrievals. 102
5.2 *PV OIR* temperature retrieval error. 103
5.3 *PV OIR* cloud-top pressure and cloud fractional scale height retrievals. 104
5.4 *PV OIR* cloud-top pressure variation with longitude. 106
5.5 *PV OIR* cloud-top pressure variation with latitude. 106
5.6 *PV OIR* water vapour abundance retrievals. 108
5.7 *PV OIR* water vapour abundance variation with longitude. 109
5.8 *PV OIR* water vapour abundance variation with latitude. 109
5.9 *Venera 15* temperature retrievals. 111
5.10 *Venera 15* temperature error retrievals. 112
5.11 *Venera 15* cloud-top pressure and cloud fractional scale height retrievals. 113
5.12 *Venera 15* cloud-top pressure variation with longitude. 114
5.13 *Venera 15* cloud-top pressure variation with latitude. 114
5.14 *Venera 15* water vapour abundance retrievals. 116
5.15 *Venera 15* water vapour abundance variation with longitude. 117
5.16 *Venera 15* water vapour abundance variation with latitude. 117
5.17 Measured and modelled *Venera 15* spectrum with small cosine viewing angle. 118
5.18 Measured and modelled *Venera 15* spectrum with average cosine viewing angle. 119
5.19 *PV OIR* and *Venera 15* temperature retrievals. 120
5.20 *PV OIR* and *Venera 15* cloud-top pressure retrievals. 122
5.21 *PV OIR* and *Venera 15* water vapour abundance retrievals. 123

5.22 *PV OIR* and *Venera 15* cloud-top pressure and water vapour abundance retrievals. 126

6.1 *PV OIR* and *Venera 15* cloud-top pressure variation with longitude. . 142

6.2 *PV OIR* and *Venera 15* water vapour abundance variation with longitude. 142

A.1 A priori temperature field corresponding to retrieved temperature field shown in figures 5.1 and 5.9. 150

C.1 CO_2 line strengths in cm^{-1}/molecule cm^{-2}. 158

C.2 H_2O line strengths in cm^{-1}/molecule cm^{-2}. 159

C.3 CO line strengths in cm^{-1}/molecule cm^{-2}. 159

C.4 SO_2 line strengths in cm^{-1}/molecule cm^{-2}. 160

List of Tables

1.1 Main characteristics of three terrestrial planets; Venus, Earth, Mars. . 3

1.2 Composition of the terrestrial planetary atmospheres; Venus, Earth, Mars, in percent fraction per unit volume. 3

1.3 Clouds in the terrestrial planets; Venus, Earth, Mars. 14

2.1 Earth based spectroscopic water abundance measurements; 1967 to 1975 (von Zahn et al., 1983). The altitude from where the observations were taken on Earth is given on the second column. 24

2.2 Water in Venus' atmosphere; recent Earth-based results. The findings are displayed from higher to lower atmospheric altitudes, given on the second column. 25

2.3 Vega 1, 2; Water vapour measurements (Surkov et al., 1986) 26

2.4 Water in Venus' Atmosphere; *in situ* and fly-by results. The findings are tabulated from higher to lower altitudes. 28

3.1 Characteristics of the *PV OIR* channels used in this study. For the mean altitude sounded by each channel refer to Fig. $4.5_{(2)}$. 40

4.1 Information content and degrees of freedom for different amount of measurements in the *PV OIR* data set. 85

A.1 A priori values for all parameters required for the nominal forward model calculations and retrievals. 151

A.2 Water vapour mixing ratios [ppm] observed by *Venera 11* (Young et al., 1984). 152

Chapter 1

Introduction

Water vapour is an important constituent in Venus' atmosphere, not because of its high abundance levels but rather because of its radiative qualities which make it the second most effective greenhouse gas in the planet's atmosphere. Phillips et al. (2001) report that if all 30 ppm of water were removed from the atmosphere of Venus, the surface would cool by 68.8 K, if one could ignore the effects of the clouds for the purposes of the argument. As a result of its importance, there exists an abundance of Earth-based, spacecraft and *in situ* studies investigating the amount, origin and role of water vapour in Venus' atmosphere. Most latitudes, longitudes and atmospheric layers have been covered in these studies but a consensus has not been reached on neither the absolute abundance nor on the distribution of the species. Differences between experimental and analysis techniques used have attributed to this fact, alongside the variability of the constituent itself in the atmosphere.

In this work the efforts undertaken to analyse jointly the *Pioneer Venus Orbiter*

Infrared Radiometer Experiment (*PV OIR*) and *Venera 15 Fourier Transform Spectrometer* (*Venera 15 FTS*) water vapour observations are presented. Although extensive work has already been successfully performed in retrieving temperature, cloud optical depth and water vapour mixing ratio as a function of altitude from these two datasets, it is believed that there exists plenty of room for improvement. New radiative transfer models, retrieval techniques and molecular line databases available nowadays will improve the analysis, and the novel approach in co-studying two different satellite measurements is bound to bring new insights and ideas to the water vapour abundance question. The main purpose of this thesis is to re-analyse to the *PV OIR* and *Venera 15* observations with the most appropriate contemporary tools and present a comprehensive global map for the water vapour abundance in Venus' middle atmosphere profiting from the spatial resolution of the *PV OIR* data and the spectral resolution of the *Venera 15* data.

In the following, a short introduction to the world of Venus and its atmosphere is presented, discussing the major basic facts about the planet, its general characteristics and its atmosphere. Since this is the introductory chapter, precise references are not usually given but most information can be found in *Venus*, 1983, and *Venus II*, 1997, edited by S. W. Bougher, Hunten, D. M. and Phillips, R. J., Space Science Series, University of Arizona Press. In the end of this chapter, an outline of the remainder of the thesis is given.

	Venus	Earth	Mars
Orbital and Rotational Data			
Mean distance from Sun [A.U.]	0.723	1.000	1.523
Eccentricity	0.0068	0.0167	0.0934
Obliquity [°]	2.6	23.45	23.98
Orbital Period [Days]	224.701	365.256	686.980
Sidereal Period [Hours]	5832.24	23.9345	24.6229
Solar Day [Days]	116.75	1	1.0287
Solid Body Data			
Mass [10^{24}kg]	4.870	5.976	0.6421
Radius [km]	6051.5	6378 [6357]	3398
Surface Gravity [m s^{-2}]	8.60	9.78	3.72
Atmospheric Data			
Composition	See Table 1.2		
Mean Molecular Weight	43.44	28.98	43.29
Mean Surface Temperature [K]	730	288	220
Mean Surface Pressure [Pa]	92	1	0.007
Mass [10^{16}kg]	47700.	530.0	1

Table 1.1: Main characteristics of three terrestrial planets; Venus, Earth, Mars.

%	Venus	Earth	Mars
Carbon Dioxide	0.965	0.0003	0.95
Nitrogen	0.035	0.77	0.027
Oxygen	~ 0	0.21	0.0013
Argon	0.00007	0.01	0.016
Water Vapour	~ 0.0001	~ 0.01	~ 0.0003
Sulphur Dioxide	0.00015	0.2 ppb	~ 0
Carbon Monoxide	0.00004	0.12 ppm	0.0007

Table 1.2: Composition of the terrestrial planetary atmospheres; Venus, Earth, Mars, in percent fraction per unit volume.

1.1 The Planet Venus; A General Introduction

Venus is Earth's closest neighbour, the second rock from the Sun. Considered Earth's twin for many decades, Venus must have been separated at birth as she exhibits almost no Earth-like characteristic other than a similar mass and radius. Her small obliquity insures that no seasons affect her rocky surface where the temperatures rise to 500°C with an associated pressure 90 times that of the Earth's. Her atmosphere is composed almost solely of carbon dioxide and is enshrouded by sulphuric acid clouds that contribute greatly to the runaway greenhouse effect that causes the high temperatures on its surface. These clouds also do not allow a direct view of the surface; until the first UV telescope turned its curious eye on her, the complicated patterns created by the cloud motions were thought to belong to the planetary surface.

In more detail, Venus belongs to the family of terrestrial planets, alongside Earth, Mars and Mercury. Known since ancient times due to its brilliant colour, brightness and unusual appearances in the sky, Venus is a planet similar to the Earth in mass and radius but has no moon and no magnetic field shielding it from cosmic rays and solar winds. Venus' obliquity is only 2.6°, compared to ~24° of the Earth and Mars and orbits in the prograde direction about the Sun in a nearly circular orbit every 224.7 Earth days. Her rotation relative to the stars, the sidereal motion, is retrograde every 243.01 Earth days. If the Sun could be seen from the surface of the planet, it would make roughly one complete circuit of the Venusian sky in half a Venus year. Hence, the length of the Venus day, also known as the solar day, is 116.75 Earth

days. The solar day is calculated as follows: $(1/224.7+1/243.01)^{-1} = \tau_{solar}$. Hence, one Venus year contains 1.925 Venus days. With respect to its relative position to the Earth, the Venus-Earth system realises a complete cycle in 583.92 Earth days, known as the sinodic period.

From the above basic numerical facts, a very interesting coincidence arises: the sinodic period is almost $\frac{8}{5}$ of the terrestrial year, as $\frac{5}{8}$ 583.92 $=$ 364.95.[1] In simple terms, this means that every eight Earth years, Venus will complete five of her cycles and present the same face to the Earth again. It is thought that this "five-to-eight" resonance has its origins in the times of creation of the solar system when planetesimals collided and formed planets.

Since Venus is closer to the Sun than the Earth, the planet shows phases when viewed with a telescope; sometimes it appears as a crescent, others half-illuminated and others nearly full. Galileo Galilei's (1564-1642) astounding observation of this phenomenon in late 1610 was the first irrevocable piece of important evidence in favour of Copernicus's heliocentric theory of the solar system. As an inferior planet Venus revolves around the Sun faster than the Earth. And as the two planets are moving in the same direction around the Sun, Venus appears for a few months in the early morning, some hours before sunrise, then disappears only to be seen as a bright moon-like object emerging after sunset for a further few months before she disappears again. And when she re-appears in the early morning, one Venus cycle has been completed and the next one begins. Venus was thus given two names by the

[1] To be precise, the terrestrial year is 365.24 days which explains the use of the word "almost". However, this only amounts to a discrepancy of two every 2,920 days.

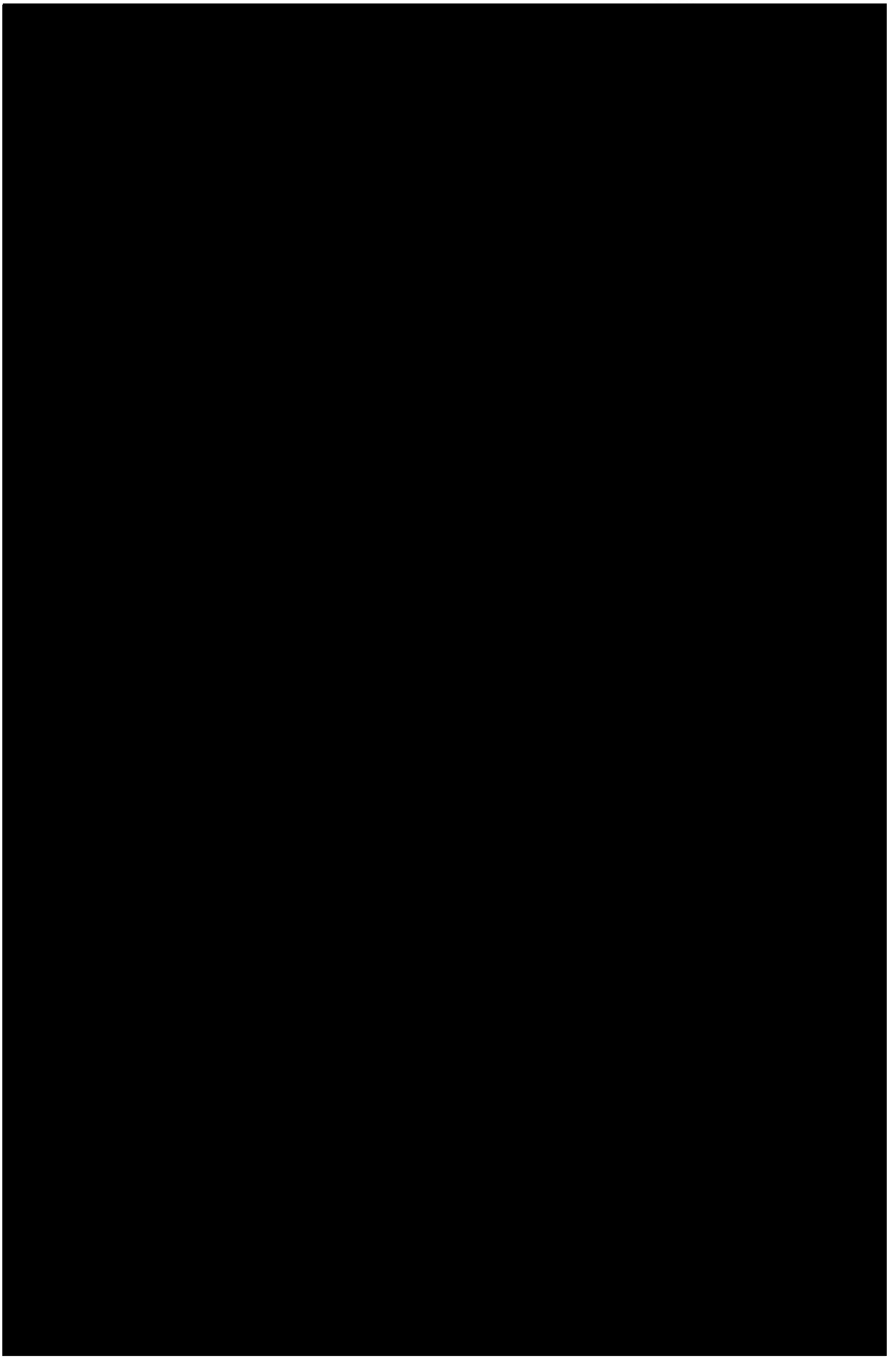

Figure 1.2: Colour-coded topographic map of Venus from Magellan radar observations. Aphrodite Terra appears as the bright feature along the equator with an area the size of South America (NASA.)

ancient Greeks to honour her double appearance in the celestial sphere: "Eosforos", the dawn bearer and "Hesperos", the evening star.

The main orbital and solid body characteristics of the three terrestrial planets that retain an atmosphere are given in table 1.1 for easy comparison and reference. Also tabulated are the atmospheric data, which will be discussed more analytically in section 1.2.

Venus was explored by a fleet of American and Soviet spacecraft starting with Mariner 2 in 1962, the first successful spacecraft to fly-by Venus, up to the Magellan orbiter in 1990, which produced global detailed maps of Venus' surface using radar mapping, altimetry and radiometry techniques with a resolution of $\sim$100 m. In

between, more than twenty missions have explored Venus, including the Soviet Venera 7 in 1970 which was the first spacecraft to land on another planet, Venera 9 in 1975 which returned the first photographs of the surface and the American Pioneer Venus Orbiter in 1978 which carried seventeen atmospheric environment experiments and four entry probes.

In figure 1.1, photographs of Venus' surface taken by the Venera 13 lander in 1982 are shown. Flat rocks and a barren environment seem to be the landscapes of our neighbouring planet. Magellan's observations further revealed that the surface of Venus is mostly covered by volcanic materials. Volcanic surface features, such as vast lava plains, fields of small lava domes and large volcanoes are common. A colour-coded composite of these observations is shown in figure 1.2. The planetary elevation is calculated over the mean radius of the planet, 6050 km. Venus has two major continents, Aphrodite Terra and Ishtar Terra, which occupy only a few percent of the total surface area. Aphrodite Terra, seen in figure 1.2, is a long, narrow area which stretches over 150° in longitude and contains a few peaks higher than 8 km. Ishtar Terra contains the highest elevation region, Maxwell Montes, around 65°N which rises to altitudes of 10.5 km above mean planetary radius. The remainder of the surface of Venus is covered mostly by volcanic materials. Although Venus has a dense atmosphere, the surface shows no evidence of substantial wind erosion, and there has been only slight evidence of limited wind transport of dust.

Figure 1.3: M. V. Lomonosov (1711-1765), the discoverer of Venus' atmosphere.

1.2 The Atmosphere of Venus

On June 6, 1761, at the University Observatory of Saint Petersburg, Russia, Mikhail Lomonosov (1711 - 1765) observed a transit of Venus, a rare passage of the planet directly in front of the Sun. He was able to get a fairly good measurement of Venus' diameter and found that it was very similar to the Earth's. But the edge of Venus' disk, instead of appearing sharp, as he had expected, was fuzzy and indistinct, and a grey halo surrounded the planet. Disappointment must have turned to wonder as he realised the true source of his annoyance; he had discovered the atmosphere of Venus. In his own words, he had found evidence of "an atmosphere equal to, if not greater, than that which envelops our Earthly sphere".

The atmosphere of Venus is composed of CO_2 (96.5%) and N_2 (3.5%) with a number of trace gases like H_2O, CO and SO_2 in the parts per million scale. As such,

it resembles the atmosphere of Mars which is also made of CO_2 and N_2 and is very different from the terrestrial atmosphere where N_2 and O_2 play the leading part. The composition of the atmospheres of the three planets is tabulated in table 1.2. The surface pressure on Venus is ~90 atmospheres and the temperature around 750 K, making its atmosphere much heavier that either that of the Earth or Mars. This high surface temperature cannot be explained purely on the basis of its closer proximity to Sun, which gives Venus about twice the solar radiation flux than the Earth, and thus stronger heating. It has been long established that the planet suffers from a massive greenhouse effect due in part to its cloud coverage, as will be seen in section 1.3.

The atmosphere of Venus may be divided into three natural regions, a troposphere (surface to 60 km), a mesosphere (60 to 90 km) and thermosphere (above 90 km). On Earth we find a troposphere (surface to 12 km), a stratosphere (12 to 45 km), mesosphere (45 to 85 km) and, as on Venus, a thermosphere (above 85 km). Vertical profiles of temperatures on Venus and Earth as a function of pressure at 30°N latitude, as measured by the Pioneer Venus OIR and Nimbus 7 spacecraft respectively, are shown in figure 1.4. Throughout the troposphere and mesosphere the temperature decreases with height, from around 740 K to 100 K on Venus and from 280 K to 210 K on Earth. No temperature inversions can be seen since UV absorbing species that cause the Earth's stratosphere do not exist in Venus' CO_2 dominated atmosphere. On Venus' dayside the temperature above 85-90 km rises to an exospheric value of around 300 K due to solar EUV absorption

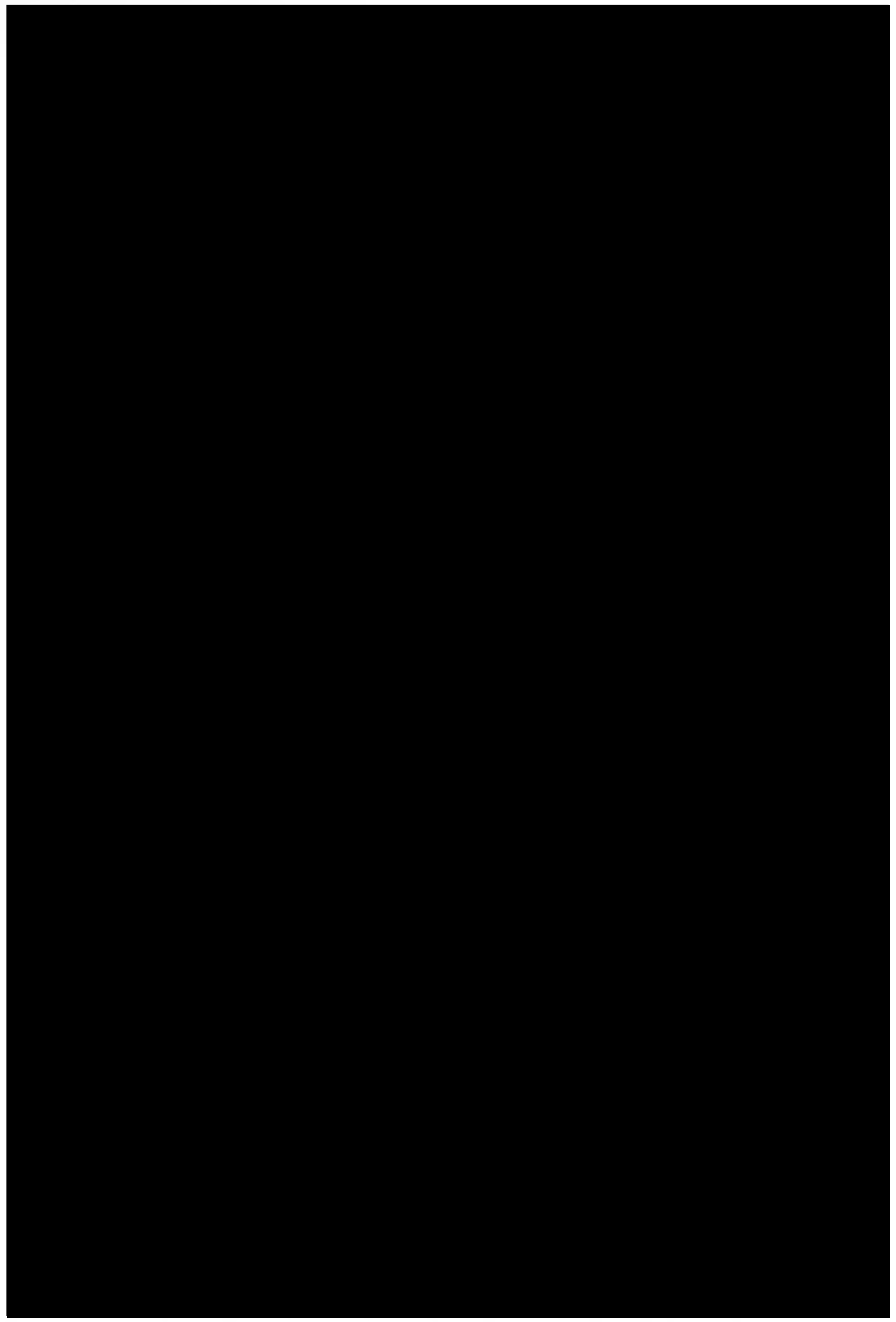

Figure 1.4: Vertical profiles of temperature vs. pressure at 30°N latitude, as measured on Venus by *PV OIR* and on Earth by Nimbus 7. Adapted from Houghton et al. (1984).

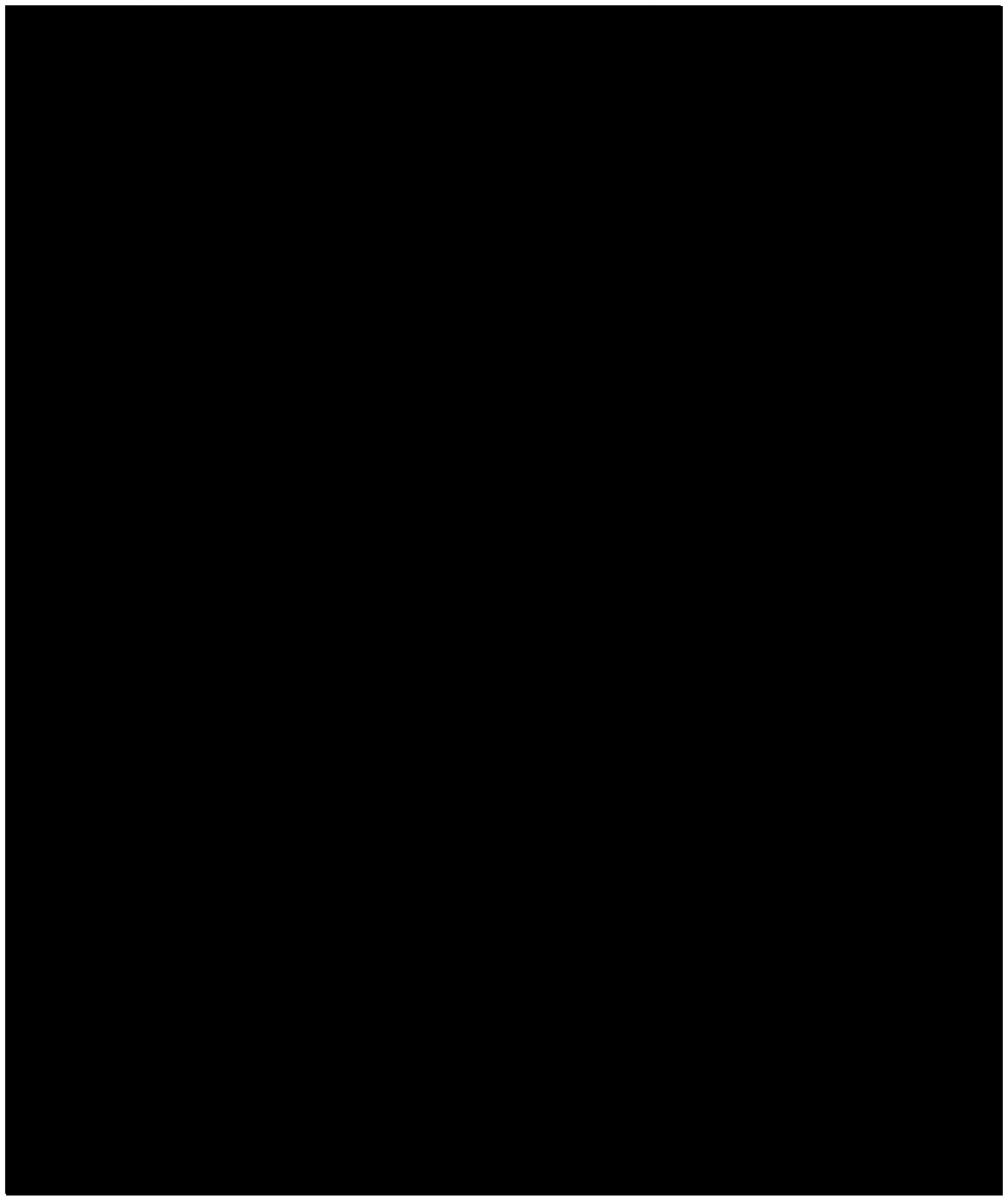

Figure 1.5: Temperatures above the main cloud regions derived from three Pioneer probes and Venera 11 and 12. Adapted from Seiff (1983).

and therefore behaves like the thermosphere on Earth, where temperatures rise from around 180 K to around 1000 K. The nightside upper atmosphere on Venus differs from that on Earth in that Venus' slow rotation period causes solar heating to be absent for far too long to maintain the high temperatures found on the dayside. Night side temperatures on Venus' thermosphere above 85-90 km in fact do not rise above 100 K, hence giving it the name "cryosphere" ("sphere of cold" in Greek.) The Venus temperature structure above the clouds and the thermosphere/cryosphere region is shown in figure 1.5 as observed by three Pioneer probes and Venera 11 and 12.

Due to its slow rotation rate and its obliquity, the troposphere of Venus is almost isothermal in equatorial and middle latitudes. Near the poles of Venus, starting at 60° N, a long-lived dramatic instability occurs, known as the "polar collar", which takes the form of a ribbon of very cold air about 10 km deep and 1000 km in radius, centred on the pole. Inside the polar collar temperatures are about 40 K cooler than outside the feature. Poleward of the inner region of the collar lies the "polar dipole", a feature consisting of two well-defined warm regions circulating rapidly around the pole with a period of 2.7 days. So far, it has been extremely difficult to physically model either one as a predictable feature of the atmosphere, even though they are highly stable features and have been observed by a number of spacecraft.

1.3 The Sulphuric Acid Clouds of Venus

Engulfing our neighbouring planet completely and all the time, sulphuric acid clouds have played a key role in the evolution of the planet and its atmosphere. Venus is covered by one global cloud layer whose main constituent is the strong aqueous solution of sulphuric acid, $H_2SO_4 \cdot H_2O$, which is formed from the photochemical combination of H_2O and SO_2 near the cloud tops[2]. The cloud layer is very opaque at visible and infrared wavelengths and reflects back ~80% of the solar incident radiation, absorbing more than half of the rest. The ~2.5% of the original sunlight that reaches the surface has an orange-coloured hue as the blue and violet colours have been absorbed by the clouds.

The main cloud layer of Venus spans from 50 km altitude to an upper boundary near 65 km, with haze layers expanding down to 30 km and upwards to 70 km, as seen in figure 1.6. Earth-based polarimetry experiments (Hansen and Honevier, 1974) showed that the cloud particles are spherical droplets, with an effective radius of $\sim 1\mu$m. The cloud optical thickness of unity was found in these studies to occur at a pressure of $\sim$ 50 mbars ($\sim$ 68 km) around 1 μm wavelengths. Mie scattering theory (Hansen and Travis, 1974) was used to model the optical properties of the Venus cloud. From the precise limits of the observed refractive index, it was confirmed that it is composed of concentrated sulphuric acid droplets containing between 75% and 90% H_2SO_4. The yellow colour of the clouds is attributed to sulphur, whereas it has lately been postulated that the unknown UV-blue absorber

[2]For the remainder of the thesis the aqueous sulphuric acid solution the Venus clouds are made of will be referred to as the "H_2SO_4 cloud" for simplicity.

Table 1.3: Clouds in the terrestrial planets; Venus, Earth, Mars.

that has puzzled scientists since the Pioneer Venus times is disulphur monoxide, S_2O (Na and Esposito, 1997).

The similarities and differences of the clouds found in the three terrestrial planets have been summarised in table 1.3. Further to their omnipresence, the Venus clouds are orders of magnitude thicker than the terrestrial or Martian ones blocking the view of the surface to all but radio wavelengths. Water plays a role in all three cloud compositions, being the major constituent in Earth's atmosphere, a minor constituent in Mars' atmosphere and locked in the sulphuric acid droplets that mainly compose Venus' clouds. The main production process is chemistry for Venus' H_2SO_4 clouds and condensation for Earth's and Mars' H_2O clouds. For the case of Mars, a second source of cloud exists in the form of dust which is lifted in the atmosphere through violent storms that frequently plague the planet. The variability of Venus' clouds is insignificant and incomparable to the daily variability of the Earth's clouds and the yearly variability of Mars' clouds.

Figure 1.6: Vertical structure of the Venus cloud system as in Knollenberg and Hunten (1980). The above data represent direct computations from the Cloud Particle Size Spectrometer (LCPS) on board the Sounder probe during the Pioneer Venus mission. A density of 2 g cm^{-3} was assumed for the mass loading computations.

In terms of a detailed vertical structure of the Venus cloud system, the Cloud Particle Size Spectrometer (LCPS) on board the Pioneer Venus Sounder probe has provided us with excellent *in situ* measurements. The actual amount of cloud droplets in the atmosphere is given by the mass loading of the atmosphere which is shown as the rightmost curve of figure 1.6. The first 30 km of the atmosphere are composed of clear CO_2 air, with the thin haze extending upwards until the altitude where the temperature drops to ~400 K and pressures of ~1 atmosphere and the atmosphere is able to sustain H_2SO_4 droplets. Then, between 44 and 48 km

altitude, a four orders of magnitude increase in the density of the cloud defines the beginning of the main cloud deck which extends upwards to 65 km altitude. Above that altitude, another haze layer spans a further 10 km. Vertical mixing from below the main cloud layer enriches it with sulphur dioxide and water. At the region of the cloud top a thin, but highly active photochemically layer exists and is the main production region of the sulphuric acid droplets. A three-dimensional cartoon of the cloud structure in Venus' atmosphere is shown in figure 1.7, viewed from an artist's perspective.

Figure 1.7: The Venusian Sulphur Cycle, by Carter Emmart, as seen in Grinspoon (1997). This cartoon demonstrates the complexity of photochemistry at work within the cloud layers.

1.4 Winds on Venus

Unlike the Earth's lower atmosphere, which is mainly driven from below by absorption of sunlight at the surface, Venus' atmospheric circulation is largely driven from above by the absorption of sunlight within and above the upper cloud layer. The cloud cover has a important influence on the atmospheric circulation by controlling the amount and distribution of solar energy absorption (Schubert, 1980).

One of the least explained phenomena of atmospheric circulation on Venus is its zonal retrograde super-rotation; the entire atmosphere, above the lowest scale height, extending upwards to >90-100 km, participates in the global super-rotation which was first observed in Earth-based ultraviolet pictures of the planet. The large-scale albedo feature known as the "dark horizontal Y" was observed to re-appear approximately every 4 Earth days, indicating a zonal rotation of the cloud level atmosphere with equatorial wind speeds of about 110 m s^{-1}, which is considerably faster than the rotation speed of the planet at the equator of 2 m s^{-1}. This super-rotation is only known to exist in the atmospheres of two solid body planets of our solar system, Venus and Saturn's largest moon, Titan. In the case of Venus the super-rotation is thought to reach the lower thermosphere, up to an altitude of around 100 km. At the cloud altitudes the wind speed and characteristics have been inferred from feature tracking in ultraviolet images of Mariner 10, Venera 9, Pioneer Venus etc. Above the clouds, in the absence of diagnostic features, analysis of Doppler shifts of selected molecular lines have procured further wind information. In figure 1.8, averaged retrograde zonal wind velocities are shown as measured by

experiments on board the Mariner 10 and Pioneer Venus satellites. The wind is maximum over the equator with speeds of ~ 100 m s^{-1} and drops off evenly towards the poles. The solid curve represents the predicted zonal wind calculated for solid body retrograde rotation.

Figure 1.8: Longitudinally averaged retrograde zonal wind velocities vs latitude, inferred from tracking of small-scale cloud features from ultraviolet images of Venus. Triangles, Pioneer Venus, by Rossow et al. (1980); circles, Mariner 10, by Limaye and Suomi (1981); squares, Mariner 10, by Travis (1978). The solid curve is the zonal wind velocity calculated for solid body retrograde rotation with equatorial speed of 92.4 m s^{-1}. Adapted from Schubert (1980).

To date, the only large scale model describing the circulation of Venus' atmosphere is the Venus Thermosphere General Circulation Model (VTGCM) (Bougher et al., 1988). While results from the VTGCM have been very useful in comparing terrestrial planetary thermospheres, its lower boundary lies at 95 km altitude, well above the region of interest for the distribution of water vapour. Further modelling is being prohibited by the inability to identify a suitable physical mechanism that

explains the cloud-top super-rotation. One interesting result from the simulations which is of potential relevance to the water vapour question is that solar conditions (both with respect to seasons on Venus and with respect to solar activity) do not affect the temperature structure on Venus below the homopause level at ~135 km altitude (Bougher and Roble, 1991).

1.5 Overview and Main Aim of this Thesis

In chapter 1, the general characteristics of the planet Venus and its atmosphere have been reviewed. After this brief introduction, the previous water vapour abundance observations and the exact problem this thesis will try to tackle are presented and discussed in chapter 2. In chapter 3, the details of the two different satellites and instruments used in this study are discussed thoroughly. Chapter 4 contains all the mathematical and computational background necessary to analyse the observations and resolve the problem, leading into chapter 5, in which the results from the new analysis are presented. In chapter 6, a number of different physical explanations are put forward in order to verify the observations and in chapter 7 the tentative conclusions of this work are summarised.

The main aim of this thesis is to analyse jointly the *PV OIR* and *Venera 15* observations with new retrieval tools and validate the existence of a local water vapour enhancement in the early afternoon region of the equatorial Venus atmosphere, observed by the *PV OIR* instrument. A further aim is to bridge any disagreement in the results of the two experiments announced in previous studies and give a

qualitative physical explanation of the retrieved temperature, cloud top pressure and water vapour abundance global maps.

Chapter 2

Water Vapour in Venus' Middle Atmosphere

In order to place the re-analysis of *PV OIR* and *Venera 15* data in a global context, other water vapour abundance observations and analytical studies are presented and discussed in this chapter. Earth-based, *in situ* and fly-by studies have yielded a plethora of different absolute water vapour abundances and distributions with altitude, latitude and longitude. Even though Janssen and Klein (1981) derive an upper limit of *3000 ppm* for water vapour abundance from brightness temperature observations near the 1.35 cm wavelength, there seems to be no consensus as to what the lower limit might be.

2.1 Remote sensing measurements from the Earth

Earth-based measurements of water vapour on Venus were rendered very difficult for many decades due to interference by the absorption of terrestrial atmospheric water vapour. Unusual and extremely dry conditions are required to obtain such measurements. A surface temperature of -15°C and H_2O abundance in the Earth's atmosphere of less than 400 $pr\mu m$ (precipitable microns)[1] are now considered good atmospheric conditions for such studies (Encrenaz et al., 1995). Even so, a number of observations of the lower atmosphere of Venus had already been completed in the pre-1975 era using both airborne and ground-based Fourier spectrometers. These measurements are presented in table 2.1 and refer to water vapour content above the Venus clouds. The altitude these observations were made is given in the second column of the table. The observations of the full disk yield on average an order of magnitude less water vapour than the partial coverage ones (von Zahn et al., 1983). This is attributed to the fact that the full disk measurements average out possible wet spots (Barker, 1975b).

Recent Earth-based studies were performed using the observational powers of the Canada-France-Hawaii FTS telescope to record high-resolution near-infrared spectra of the night side of Venus (Bézard et al., 1990), the IRAM radio telescope in Pico Valeta, Spain, to detect the 1.327 mm line of HDO (Encrenaz et al., 1991), the IRTF telescope at Mauna Kea Observatory to probe into the 1.27 and 2.3 μm

[1] A precipitable micron is a unit of column-integrated water density. 1 pr μm is equal to 10^{-4} g cm^{-2} which is equal to $3.34611 \cdot 10^{18}$ molecules cm^2 of H_2O. To convert to parts per million *ppm* a total atmospheric density profile is required. For Venus, it can be assumed roughly that 1 pr $\mu m \cong 2$ *ppm*.

thermal emission windows (Bell III et al., 1991), to name but a few such studies. For the extended observations catalogue refer to table 2.2 where a complete list of measurements, region of Venus observed and consequent water vapour abundance results is presented.

2.2 Remote sensing measurements from Satellites

Mariner 2, launched on August 27 1962, was the first spacecraft to flyby another planet on December 14, 1962 when it passed within 34,833 kilometres from the surface of Venus. Since then, Venus has been visited by more or less twenty spacecraft which carried an assortment of experiments primed to study water vapour abundance. Two fly-by missions are particularly remarkable for their water vapour findings; the infrared radiometer experiment on board Mariner 10 that measured limb darkening curves of Venus' upper atmosphere in the 11.5 and 45 μm spectral region (Taylor, 1975) and the Near Infrared Mapping Spectrometer, NIMS, which observed the 1.18 μm spectral window during the Galileo fly-by (Drossart et al., 1993). The results from these two missions are presented in table 2.4. The results from the two main satellite water vapour abundance experiments, the *PV OIR* and the *Venera 15* FTS, are discussed in the separate section 2.4.

Water Column Abundance pr μm	Observation Level km	Water bands μm	Coverage of disk	Reference
<20	**0.7**	1.2 to 2.5		Connes and Connes (1966)
<16	**2.1**	0.82	partial	Owen (1967)
$< 10^{-4}$	**2.1**	0.82	partial	Belton et al. (1968)
<16 to 40	**2.1**	0.82	partial	Schorn et al. (1969)
<0.3 to 25	**2.1**	0.82	partial	Barker (1975b)
<1	**2.3**	0.82	full	Traub and Carleton (1975)
<1	**11.3-12.6**	1.4 and 1.9	full	Kuiper and Forbes (1967)
2	**12.2**	1.4, 1.9 and 2.7		Kuiper et al. (1969)
0.4 ± 0.1	**12.2**	1.4, 1.9 and 2.7	full	Fink et al. (1972)
<8	**14.6**	0.82	full	Gull et al. (1974)

Table 2.1: Earth based spectroscopic water abundance measurements; 1967 to 1975 (von Zahn et al., 1983). The altitude from where the observations were taken on Earth is given on the second column.

Water Vapour Abundance [ppm]	Altitude [km]	Solar Lat/Lon observed	Line or window detected	Reference
3.5±2.0	**> 65**	whole disk	1.324 mm	(Encrenaz et al., 1991)
1.0(+1.0, -0.5)	**> 65**	whole disk	1.635 mm	(Encrenaz et al., 1995)
7.0(+5.0, -4.0)	**> 65**	Venus at 0.65° phase	1.324 mm	(Encrenaz et al., 1995)
0.8	**> 65**	30°N night-side	1.74 & 2.3 μm (window)	(Bézard et al., 1990)
40	**0-55**	30°N night-side	1.74 & 2.3 μm	(Bézard et al., 1990)
40±20	**0-45**	North Hemisphere Night-Side	1.23 & 2.3 μm	(Crisp et al., 1991a)
30(+15,-10)	**30-40**	5°N, 25°N and 15°S	2.3 μm	(de Bergh et al., 1995)
20±10	**30-50**	50% of nightside	1.0, 1.1 & 1.8 μm	(Meadows and Crisp, 1996)
45±15	**0-30**	50% of nightside	1.0, 1.1 & 1.8 μm	(Meadows and Crisp, 1996)
30±6	**23.5-33**		1.23, 1.74 & 2.3 μm	(Pollack et al., 1993)
30±10	**15-25**	15°S	1.74 μm	(de Bergh et al., 1995)
30±10	**12**		1.23, 1.74 and 2.3 μm	(Pollack et al., 1993)
30±15	**0-15**	15°S	1.1-1.3 μm	(de Bergh et al., 1995)
3.5 - 15	**0**		1.23, 1.74 & 2.3 μm	(Pollack et al., 1993)

Table 2.2: Water in Venus' atmosphere; recent Earth-based results. The findings are displayed from higher to lower atmospheric altitudes, given on the second column.

Table 2.3: Vega 1, 2; Water vapour measurements (Surkov et al., 1986)

2.3 *In Situ* measurements

The most impressive studies of Venus' atmosphere, technology-wise, are undoubtedly the descent probes and balloons that have braved the hostile territory with a number of different experimental techniques in order to measure water vapour *in situ*. A selection of these studies is described below:

The Pioneer Venus (P V) Large and Sounder probes both carried a neutral mass spectrometer to study, among other species, the water vapour abundance during their descent through the sulfurous clouds (Hoffman et al., 1983; Donahue and Hodges, 1993) and a gas chromatograph mounted on the P V Sounder probe further measured the chemical composition of the atmosphere in three distinct altitudes (Oyama et al., 1980). Spectrometers on board the Venera 11, 13 and 14 descent probes recorded spectra of sunlight penetrating into the lower atmosphere of Venus (Ignatiev et al., 1997), a gas-chromatograph on board Venera 13 and 14 measured an important number of minor atmospheric constituents including water (Mukhin et al., 1982), humidity measurements were obtained from using an electrolytic sensor on Venera 13 and 14 (Surkov et al., 1982) and the spectral and angular distribution of solar radiation scattered in the Venus atmosphere was

observed by Venera 13 and 14 (Moroz et al., 1982). Last but not least, the Vega 1 and 2 balloons carried a hydrometer mounted on their landing rings. Humidity measurements were carried out successfully for their 40 hours long journey (Zasova et al., 1996). The extended list of satellite and *in situ* results is presented in table 2.4.

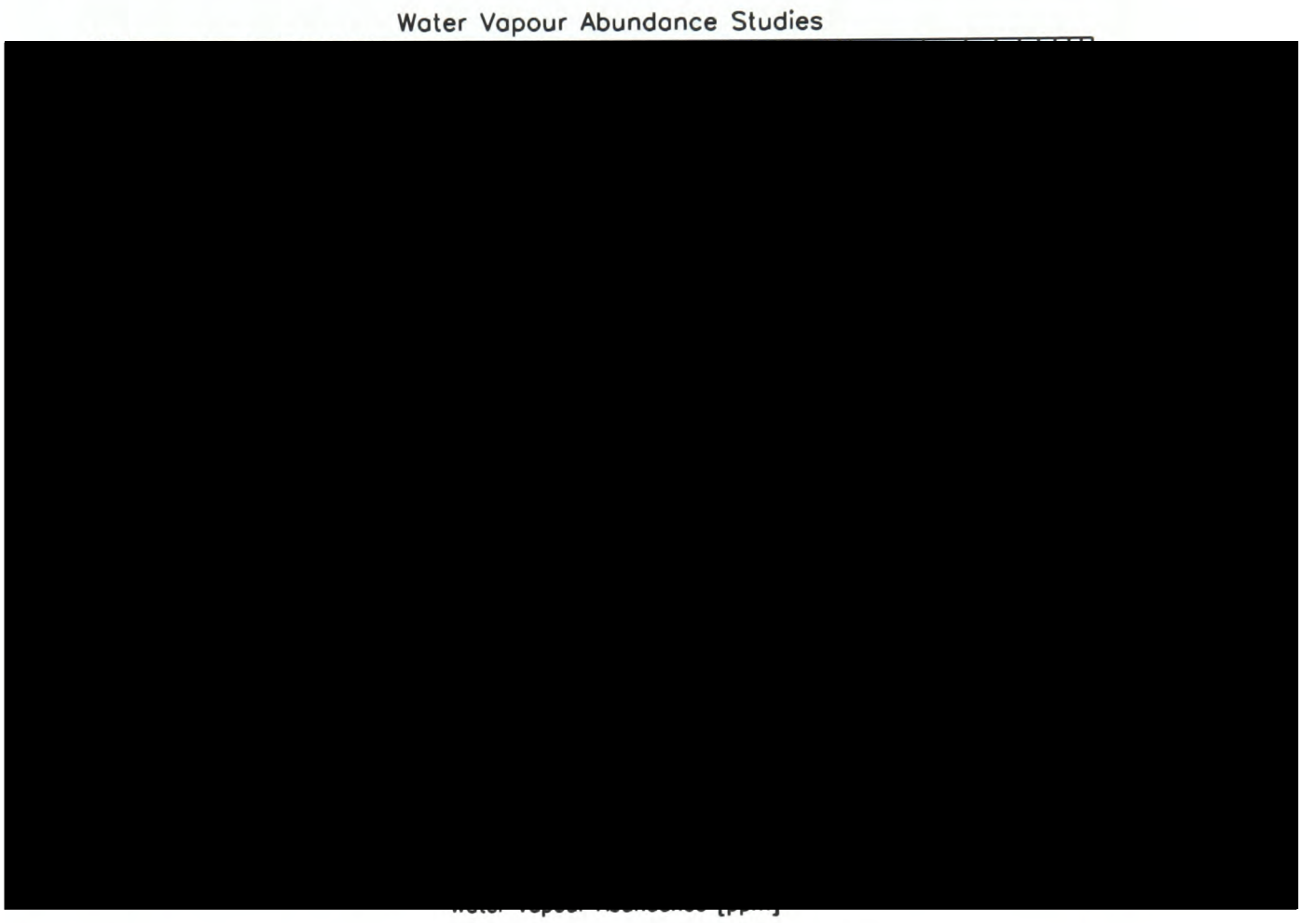

Figure 2.1: Water vapour abundance in Venus' atmosphere vs altitude. The plot is colour-coded as follows: fly-by missions are in green, *in situ* studies are in red, satellite results are in black and Earth-based observations are in blue. In detail: Red-filled dotted squares right-slanted: Moroz et al. (1982), red long-dashes line: Oyama et al. (1980), red solid lines: Moroz et al. (1979a), Young et al. (1984), red dash-triple dotted lines: Donahue and Hodges (1992), Donahue and Hodges (1993), red-filled squares left-slanted: Revercomb et al. (1985), red-filled square right-slanted: Surkov et al. (1982), red solid filled square left-slanted: Mukhin et al. (1982), blue dash-dotted line: Bell III et al. (1991), blue dashed lines: Encrenaz et al. (1995), Encrenaz et al. (1991), blue solid lines: Pollack et al. (1993), Crisp et al. (1991a), Bézard et al. (1990), blue dash-triple dotted line: Meadows and Crisp (1996), blue dotted line: de Bergh et al. (1995), green-filled square right-slanted: Taylor (1975), green-filled square left-slanted: Drossart et al. (1993), black-filled square left-slanted: Moroz et al. (1990), black dotted line: Ignatiev et al. (1997), black-filled square right-slanted: Ignatiev et al. (1999), black dashed line: Schofield et al. (1983)[night-side], black dash-dotted line: Schofield et al. (1983)[day-side].

An attempt to visualise the disagreements between the different post-1975 observational methods is presented in figures 2.1 and 2.2. In figure 2.1, the variation

Water Vapour Abundance [*ppm*]	Altitude [*km*]	Solar Lat/Lon observed	Spacecraft	Reference
80	**60-80**	(20 to 50°N, nightside)	Mariner 10	(Taylor, 1975)
30-50	**48-65**	Figure 2.3	Venera 11, 13 and 14	(Ignatiev et al., 1999)
20±10	**58-62**	Figure 3.4	*Venera 15*	(Moroz et al., 1990)
5-15	**58-62**	Figure 3.4	*Venera 15*	(Ignatiev et al., 1997)
100±50	**45-65**	Figure 3.2	*PV OIR*	(Schofield and Taylor, 1982)
700±300	**49-58**	(7.5°S,303.5°)	Venera 13	(Mukhin et al., 1982)
700±300	**49-58**	(13°S,310°)	Venera 14	(Mukhin et al., 1982)
2000±400	**46-50**		Venera 13, 14	(Surkov et al., 1982)
600	**52**	(4.4°,304°)	P V - Sounder	(Oyama et al., 1980)
200	**40-48**		Venera 13	(Moroz et al., 1982)
5190	**42**	(4.4°,304°)	P V - Sounder	(Oyama et al., 1980)
30±15	**20-40**	(40°S to 50°N)	NIMS-Galileo	(Drossart et al., 1993)
1350	**22**	(4.4°,304°)	P V - Sounder	(Oyama et al., 1980)
25±15	**35**	(40°S to 50°N)	NIMS-Galileo	(Carlson et al., 1991)
50±25	**20**	(40°S to 50°N)	NIMS-Galileo	(Carlson et al., 1991)
Table 2.3	Table 2.3	Figure 2.1	Vega 1, 2	(Surkov et al., 1986)
30±10	**5-48**		Venera 11, 13 and 14	(Ignatiev et al., 1997)
50-70	**0-5**		Venera 11, 13 and 14	(Ignatiev et al., 1997)
20	**0**		Venera 13	(Moroz et al., 1982)
20	**0-60**		Venera 11 and 12	(Moroz et al., 1979a)

Table 2.4: Water in Venus' Atmosphere; *in situ* and fly-by results. The findings are tabulated from higher to lower altitudes.

of water vapour abundance [*ppm*] with altitude [*km*] is shown. This figure is colour-coded as follows: fly-by missions are in green, *in situ* studies are in red, satellite results are in black and Earth-based observations are in blue. The Earth based observations (blue colours) suggest a constant water abundance below the cloud region, with severe depletion in the main cloud deck and a minimal value above that altitude. The Venera 11, 13, 14 and Vega 1, 2 (red colours) observations point to a constant water abundance below the clouds with a distinct source of water vapour in the main cloud deck, followed by depletion over the cloud tops. The experiments on board the Pioneer Venus Satellite and Probes (black and red colours) seem to agree in principal to the rest of the *in situ* studies; a constant profile up to the cloud deck, with strong enhancement within and above the cloud region and steady decline above that altitude. In short, most studies point to a column abundance value between 10 and 200 ppm, with a much bigger spread in the main cloud deck region (40 to 65 km altitude) between 1 and 5000 ppm. It is wise to note here that in both Earth-based and space-born studies the error bars quoted are wide enough not to allow a more precise interpretation of the data.

In figure 2.2, the relationship between spectral region investigated [μm] and water vapour abundance [*ppm*] retrieved is examined. Although it is true that longer wavelengths do not probe as deeply into the atmosphere of Venus as shorter ones and hence a different abundance is expected from such studies, e.g. from Encrenaz et al. (1991), a closer agreement between results was expected for the 0.2 to 1.2 μm region. This figure is colour-coded as follows: *in situ* studies are in red, satellite results are

Figure 2.2: Variation of water vapour abundance with spectral region investigated. This figure is colour-coded as follows: *in situ* studies are in red, satellite results are in black and Earth-based observations are in blue. Blue-filled squares: Meadows and Crisp (1996), Crisp et al. (1991a), Bézard et al. (1990), Drossart et al. (1993), de Bergh et al. (1995), blue solid lines: Encrenaz et al. (1995), Encrenaz et al. (1991), red-filled squares left-slanted: Moroz et al. (1982), red dash-dotted line: Young et al. (1984), black-filled dotted square: Moroz et al. (1982), black-filled left-slanted square: Ignatiev et al. (1999), black-filled right-slanted square: Irwin (1997).

in black and Earth-based observations are in blue. Some of the measurements shown in figures 2.1 and 2.2 are placed on a map of Venus shown in figure 2.3. The most important and relevant to this work measurements have been located on this square map of Venus. The coverage of the *PV OIR* and *Venera 15* instruments is presented separately in chapter 3. As can be noted, the globe has been relatively well covered at low latitudes, with most equatorial regions viewed by more than one type of instrument or technique, and less well covered at polar latitudes.

Figure 2.3: Global coverage of Venus' disk by spacecraft and Earth-based studies. By "solar longitude" we mean that 0°E, 0°N represents the sub-solar point. Black diamonds: Venera 11, 13 and 14, red diamonds: Vega 1 and 2, red square: Bézard et al. (1990) red left-slanted lines: Galileo fly-by, red right-slanted squares: Bell III et al. (1991), little blue squares; de Bergh et al. (1995), blue right-slanted slabs: Crisp et al. (1991a); green diamonds: Pioneer Venus Probes, green left-slanted slabs: Meadows and Crisp (1996), green right-slanted square: Encrenaz et al. (1991) and Encrenaz et al. (1995).

In conclusion, the results from the Earth-based observations, summarised in table 2.2, point to a constant average value of 30 ± 15 *ppm* between 0 and 40 km with steady decrease above that altitude. On the other hand, from the satellite and *in situ* studies shown in table 2.4, one can infer a steady increase in absolute abundance which peaks in the cloud region to 200 ± 100 *ppm* and a constant decrease above 60 km.

2.4 Remote sensing measurements from *PV OIR* and *Venera 15*

Pioneer Venus Orbiter Infrared Radiometer

As the scope of this work is to analyse jointly the *PV OIR* and the *Venera 15* spectra, the results from the primary analyses of both these observations are briefly reproduced in the following two sections.

The first comprehensive analysis of the *PV OIR* data which focused on water vapour retrievals, after the initial report by Taylor et al. (1980), was performed by Schofield et al. (1983). The variation with latitude and longitude[2] of water vapour column amount [pr μm], cloud top pressure [mbars], cloud top temperature [K] and temperature at 70 mb ($\sim$65 km) [K] as derived from far-infrared measurements, for the altitude region 50 to 120 km, is shown in figure 2.4. The figure shown is a composite plot of results reported in Schofield et al. (1983). The *PV OIR* data were averaged in bins of 10° in latitude and 30° in longitude. Water vapour column abundance was shown to increase slowly during the day but remains approximately *10-15 pr μm* except in the region euphemistically known as *wet spot*. This spot was found by the investigators to be centred on mid-afternoon and asymmetric, decreasing more rapidly downwind. In addition, the cloud top pressure was shown to decrease (equivalent to a cloud top height increase) in parallel with the water vapour maximum, reaching its lowest of 80 mbars just before the evening terminator. Even

[2]In this and subsequent chapters, the term "longitude" will always refer to "solar longitude".

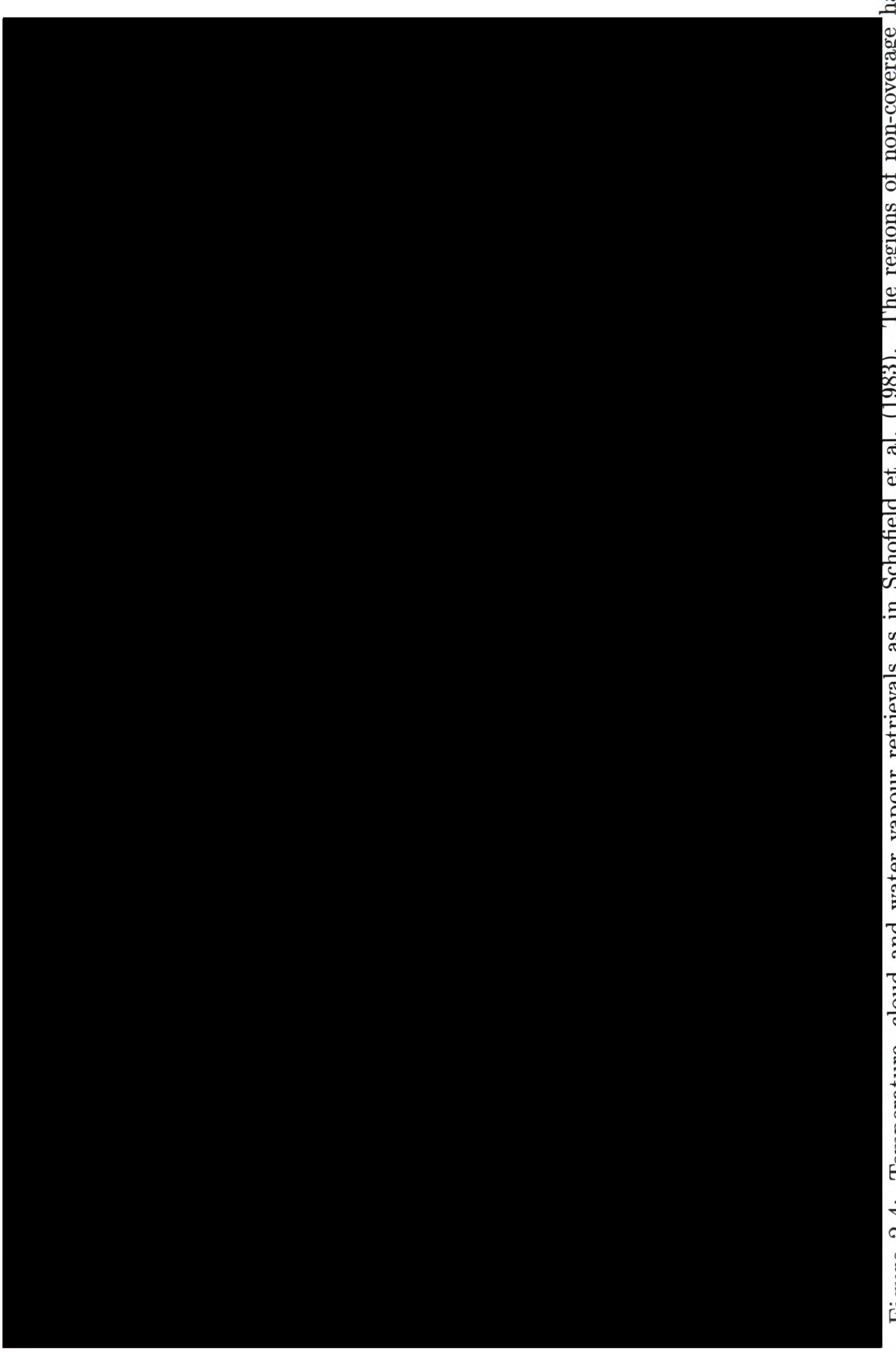

Figure 2.4: Temperature, cloud and water vapour retrievals as in Schofield et al. (1983). The regions of non-coverage have been interpolated by the authors for presentation purposes.

though these results have been considered controversial in the past, it is evident from table 2.4 that they are by no means unreasonable or beyond the range predicted by similar satellite studies. A retrieved water vapour day-night variation from the same study has also been shown in figure 2.1, as the black dash (night-side) and dash-dot (day-side) lines.

Venera 15 Fourier Transform Spectrometer

Moroz et al. (1990) reached some key conclusions with their preliminary analysis of the *Venera 15* on-board[3] data: in the 58 to 62 km range the water vapour abundance was found to have a mean of 20 ± 10 *ppm*, with local point-to-point variability reaching a factor of five but without any day-night variations. In their subsequent analysis, Ignatiev et al. (1999) conclude that the large scale variation in water vapour abundance is not constant and varies from *1 to 20-30 ppm*, with most measurements falling into the limits of *5-15 ppm*. Furthermore, Ignatiev et al. (1999) report day-night variations of one order of magnitude, with the maxima and minima located around 30° and 210°E. They also report, from the on-board data, an increasing mixing ratio with increasing latitude, which is taken as an indication of the negative vertical gradient of the mixing ratio profile (shown in figure $2.5_{(2)}$). They hence conclude in a decrease of water vapour abundance with altitude, but they also note that this feature could equally be due to the change of latitude during

[3]The Venera 15 dataset is presented extensively in section 3.2. Suffice it here to note that there exist two modes of processing the Venera 15 measurements and those are referred to as "on-board" and "on-Earth".

the observations. The results from the on-Earth processed spectra (figure $2.5_{(1)}$) and from a special viewing session of on-board spectra (figure $2.5_{(3)}$) point to an average water vapour abundance in the region of *5-25 ppm.*

2.5 Synopsis

In this section an extensive presentation of all the different instrumental, experimental and computational analysis techniques found in the literature of Venus' water vapour abundance was completed. The main intention behind this presentation was to place the wet spot observed by Schofield et al. (1983) and the Ignatiev et al. (1999) observations in context with other similar studies.

One can safely state that the idea of high spatial and temporal variability in water vapour column abundance is not completely unheard of; Barker (1975b) openly mentions wet spots, Revercomb et al. (1985) observed enhanced amounts of water vapour in the sub-solar point, Moroz et al. (1990) report latitude dependence and quote that "local point to point variability could achieve a factor of 5" and Bell III et al. (1991) actually observed hot and cold spots and radiances that changed by 50-65%. The scientific community throughout the years have agreed to disagree both on the magnitude, source and variability in water vapour. Long term studies, such as the ones presented by Encrenaz et al. (1995) explicitly comment on annual fluctuations while others are apprehensive of the fact that the error estimates themselves do not permit a more precise conclusion to the issue; Drossart et al. (1993) quote no latitude dependence in the Galileo fly-by data larger than 20% but with an

error estimate of 50% the issue is left open to debate. The heavy dependence of the retrievals on background information has been well demonstrated by Donahue and Hodges (1992) and Donahue and Hodges (1993), as well as the dependence on general knowledge about the atmospheric state and radiative properties, as seen by the different analyses of Young et al. (1984) and Moroz et al. (1979a) (c.f. appendix A.1 for more details.).

Above all, the main striking point of disagreement between the *in situ* and Earth-based studies remains dealing with the cloud deck either as a vast source of water vapour or as a region of its severe depletion. Even though it was not discussed in section 1.3 since it will be thoroughly examined in chapter 4, the incomplete knowledge of the detailed chemistry at work at those altitudes, in parallel with the many unknowns concerning the absolute abundances of key species, has tied the hands of many scientists who were trying to photochemically explain the diverse observations. In chapter 6, a tentative attempt will be made to explain the results of the new analysis of the *PV OIR* and *Venera 15* water vapour observations with focus on the physics behind them. It is further understood that the diverse methods of analysing the data, whose resolution and wavelength ranges change appreciably between studies, alongside the differences in assumptions for the *a priori* information and viewing geometry, attribute hugely to the noted disagreement. With the joint analysis of the *PV OIR* and *Venera 15* data for the first time the measurements from two different experimental methods of acquiring remote sensing data will be used to retrieve temperature, cloud and water vapour abundance global maps.

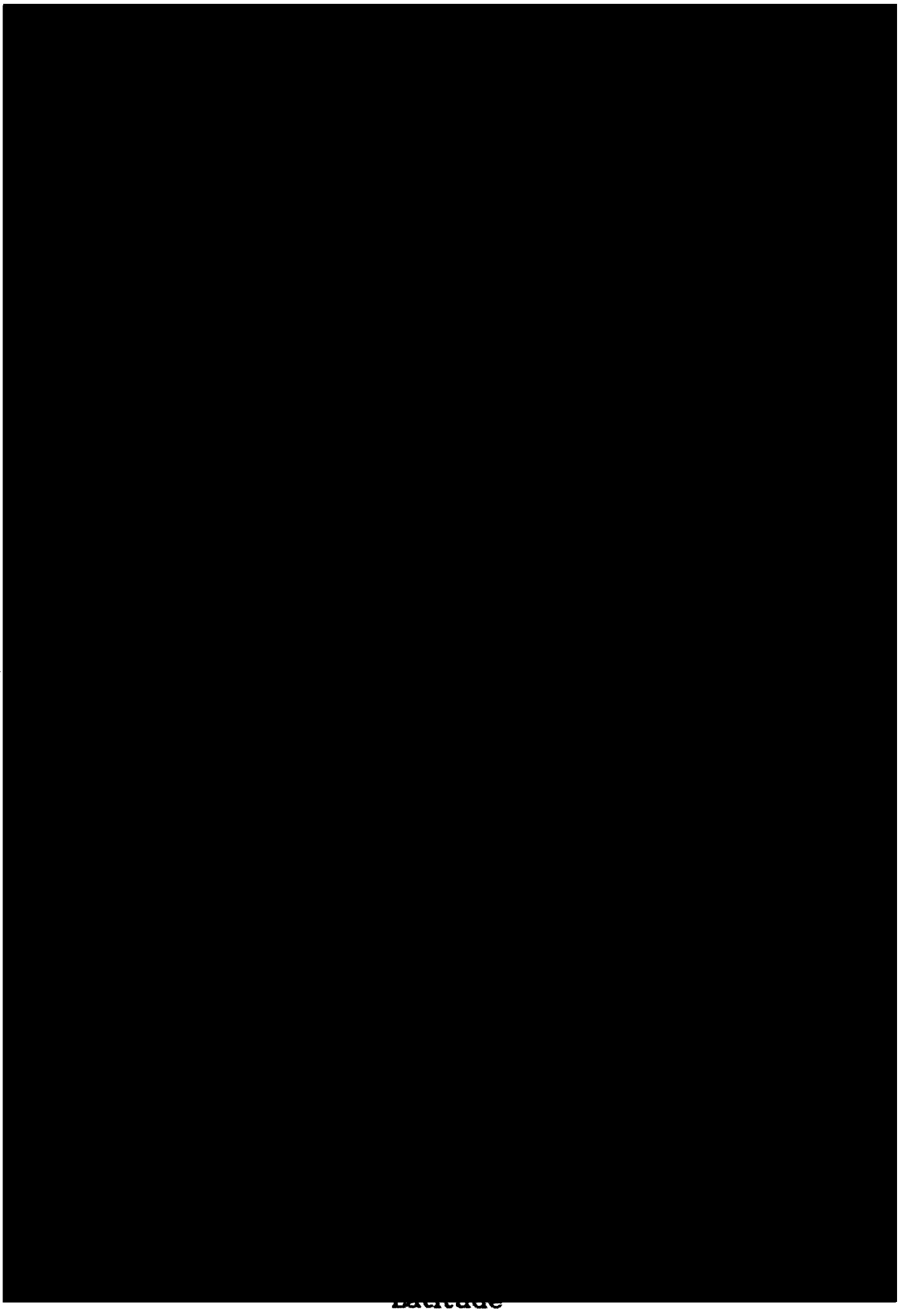

Figure 2.5: Water vapour mixing ratios vs latitude and local solar time, as in Ignatiev et al. (1999). Upper panel, results from the on-Earth *Venera 15* spectra. Middle panel, results from the on-board *Venera 15* spectra. Lower panel, results from the on-board *Venera 15* spectra, special near-nadir viewing session.

Chapter 3

The Pioneer Venus OIR and Venera 15 FTS Instruments

In the previous chapter the amount of studies investigating water vapour abundance in Venus' atmosphere has been revealed. Nevertheless, very seldom has a common analysis of two different data sets been endeavoured with sole examples the works of Pollack et al. (1993) and Ignatiev et al. (1997). In the first work, two sets of ground based spectra of Venus' nightside thermal emission were co-analysed in order to validate spectroscopic data bases. In the second, visible spectra of sunlight obtained by the Venera 11, 13 and 14 probes were used to explore the discrepancy between *in situ*and remote sensing predicted water vapour amounts. However, it is for the first time that measurements acquired from the *Pioneer Venus Orbiter Infrared Radiometer* and *Venera 15 Fourier Transform Spectrometer* instruments will be analysed with the same tools and in this chapter these two different data

sets are presented in order to be able to explain in chapter 4 precisely how they were analysed and produced the results shown in chapter 5.

3.1 *Pioneer Venus Orbiter Infrared Radiometer*

Figure 3.1: The Pioneer Venus Orbiter revolving around Venus (artist's impression.)

The spin-stabilised *Pioneer Venus Orbiter*, seen in figure 3.1, was placed in a highly eccentric, 24-hour orbit in a plane inclined at about 105° to the ecliptic on the December 4, 1978. Its cruise altitude varied from 150-200 km at periapsis to 66,900 km at apoapsis (Colin, 1980). The aims, design and properties of the *Pioneer Venus Orbiter Infrared Radiometer* experiment, *PV OIR* , also known as *VORTEX* after Venus Orbiter Temperature Sounding EXperiment, have been thoroughly described in Houghton and Taylor (1975), Taylor et al. (1979c) and Delderfield et al. (1980).

Channel number	Central waveno. [cm^{-1}]	Range [cm^{-1}]	Field of View [deg]	Noise [α]	Principal Retrieval Function
8	228.0	50.0 - 400.0	1.25	95	Water vapour
2	679.4	672.6-692.6	1.25	48	Temperature
3	727.2	716.8-744.8	1.25	74	Temperature
4	764.4	749.6-777.6	1.25	75	Temperature
5	869.5	852.5-896.5	1.00	50	Cloud Structure

$^{\alpha}$ The units for noise are nW $cm^{-2}sr^{-2}(cm^{-1})^{-1}$.

Table 3.1: Characteristics of the *PV OIR* channels used in this study. For the mean altitude sounded by each channel refer to Fig. $4.5_{(2)}$.

The experiment was highly successful and returned hundreds of thousands of measurements between orbit insertion and 14 February 1979, when its operation was terminated prematurely due to the failure of the instruments' power supply. The first findings of the Pioneer Venus Orbiter and multiprobe missions have been published in a special issue of the *Journal of Geophysical Research*, volume 85, number A13, pp. 7573 to 8337.

The orbiter spin axis was aligned with the celestial south polar axis and was inclined 45° to the field of view of the *PV OIR* experiment, hence constraining its coverage mainly to the Northern Hemisphere. As Venus rotates in a retrograde sense, each orbit occurred 1.48° eastwards (earlier in Venus' day) than its predecessor in a planet-fixed coordinate system. The coverage pattern of the planet is shown in figure 3.2 and it depicts the 72 days for which the *PV OIR* data were acquired. The gap in the local afternoon, shown in the dark green colour, would have been filled

with another 12 days of instrument operation[1]. Because the Pioneer Venus was a spinning spacecraft, the field of view of *PV OIR* crossed the limb of the planet twice for every rotation. And since the spacecraft spin rate was 5 rounds per minute, near simultaneous observations of the same region at different zenith angles were acquired. This proved to be a very valuable asset in simultaneously retrieving cloud structure and temperature profiles as shown both in Taylor (1974) and in section 4.4 of this thesis.

The basic properties of the five *PV OIR* channels used in this study are summarised in table 3.1. Three fixed grating spectrometers (designated "channels 2, 3 and 4") were used to study the 667 cm^{-1}(15 μm) absorption band of CO_2, centred at 679.4, 727.2 and 764.4 cm^{-1}. Even though the infrared emission of the Venus atmosphere is mostly dominated by CO_2, there exist atmospheric windows that allow the study of other species. In order to study the cloud absorption properties, a fourth grating spectrometer ("channel 5") was placed in such an atmospheric window at 869.5 cm^{-1}(11.5 μm). A filter radiometer, referred to as channel 8 or "the water channel", was employed to sense the H_2O rotational band at 228.0 cm^{-1}(45 μm). Channels 2 through to 5 have triangular filter shapes, with central wavenumbers and ranges as shown in table 3.1 whereas the channel 8 radiometer profile has been derived from laboratory calibration measurements. The field of view of the *PV OIR* instrument is a circle and so one angle is enough to define its coverage. For the five *PV OIR* channels mentioned above, the field of view is about 1.25° (about 3 km for

[1]The dark green colour will be used in the remainder of the thesis to signify regions with no coverage.

nadir view and 20 km for limb view, at the periapsis altitude.)

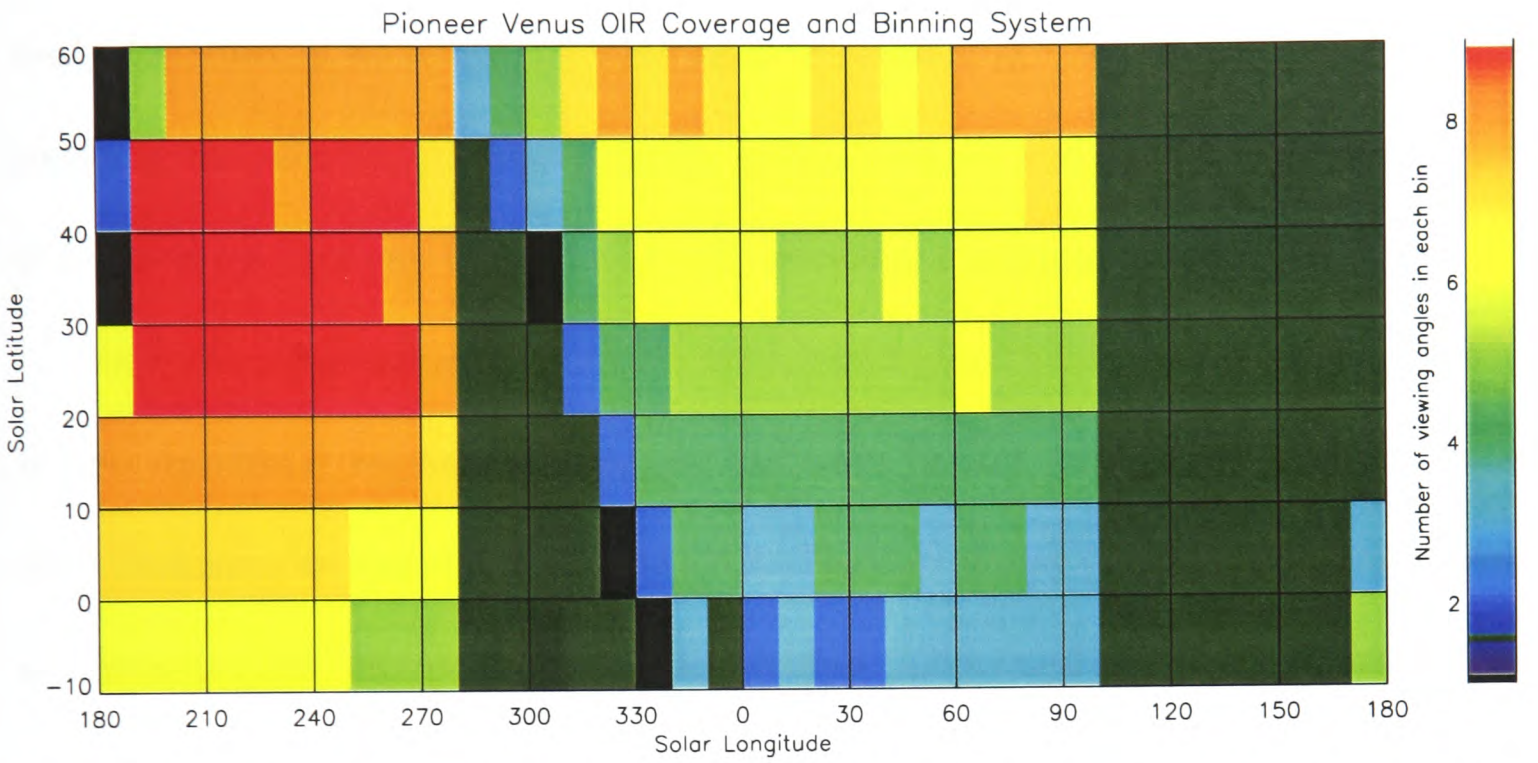

Figure 3.2: *PV OIR* planetary coverage. The *PV OIR* data are averaged in bins of 10° in latitude and longitude. The gap in the local afternoon (depicted by the dark green colour) would have been filled with another 12 days of the instruments' operation.

Following the footsteps of Schofield and Taylor (1982) and the diagnostic tools of Rodgers (2000), we projected the *PV OIR* measurements onto 10° by 10° bins in latitude and longitude. This choice was made in order to enhance the wet spot region and identify more detailed structures, as compared with the previous analysis where the data were projected onto 10° in latitude and 30° in longitude bins. Due to the spinning of the Pioneer Venus orbiter, the *PV OIR* measurements have an associated viewing (zenith) angle. So as to reduce the amount of measurements with very similar viewing angles, the data found within one bin was averaged onto a maximum of nine viewing angles, from 0.1 to 0.9 in cosine viewing angle space[2]. So, in one bin up to nine different viewing angles, i.e. up to nine different sets of

[2] 0° is the nadir view and 90° is the limb view.

measurements may result, as can be seen by the colour bar of figure 3.2. Note that most bins do not contain as many different viewing angles. However, the diagnostic tools described in section 4.4.3 were used to validate mathematically the choice of reducing the amount of measurements in this manner and also confirm the choice of parameters that can be retrieved with reasonable accuracy from them.

Since the main scope of this work is to investigate the water vapour abundance in the equatorial region our analysis has been limited in latitude, from 10°S to 60°N inclusive, as was shown in figure 3.2. The complexity of the Venus atmosphere northwards of 60° further supports this decision. Kliore and Patel (1982) studied the variation of the tropopause altitude, pressure level and temperature with altitude and clearly distinguish three regions: an equatorial/mid-latitude one up to 40°N, a transitional one between 40°N and 55°N and the polar collar one from 55°N to 77°N. These exhibit great variability in the tropopause characteristics. Investigations in both Schofield and Taylor (1982) and Ignatiev et al. (1999) have also clearly identified two latitudinal regions in the two sets of measurements with 60°N being the separating parallel.

3.2 *Venera 15 Fourier Transform Spectrometer*

The *Venera 15* Orbiter, seen in figure 3.3, was placed in a 87.5° inclination elliptic 24-hour orbit. The *Fourier Transform Spectrometer*, FTS, had a fixed instrument orientation and obtained 64 days worth of measurements, from 12 October 1983 until 14 December 1983, nearly the same Venus season as during the Pioneer Venus

Figure 3.3: The Venera 15 orbiter.

visit.

A detailed description of the *Venera 15 FTS* experiment has already been given by Moroz et al. (1986) and Oertel et al. (1990). The instrument was aligned so that the 4° by 4° rectangular field of view moved from ~20°N via the North Pole down to 25°N, while covering the longitude region 60° to 160°E and 230° to 330°E in solar coordinates (approx. 02:00 to 08:00 and 14:00 to 20:00 in local times.) The chosen orientation insured near-nadir observations of the North Polar region and a minimum periapsis altitude of ~1000 km at 63°N allowed each "global" measurement to be completed in about 25 minutes (Moroz et al., 1986). The minimum field-of-view was achieved over the North Polar region at 60x60 km^2.

The instrument had two modes of processing the measurements acquired, either by processing the data on board the spacecraft or by transmitting the full length spectrum back to Earth. The on board processed spectra, hereafter called "on-

Figure 3.4: *Venera 15* FTS planetary coverage. Both on-board and on-Earth spectra are projected in 10° bins in latitude and longitude. The colour bar indicates the number of spectra found in each bin. The vertical white lines show the longitudinal borders of a subset of 42 averaged spectra created by Ignatiev et al. (1999), which will also be used in this work for validation purposes.

board", have a wavenumber range that spans from 274.34 to 1656.46 cm^{-1} with a resolution of 6.94 cm^{-1}. The *Venera 15 FTS* instrument has acquired 1043 such spectra in its nominal orbital inclination, out of which 384 spectra fall within the 10°S to 50°N latitudinal range of interest to this work. The on Earth processed spectra, hereafter called "on-Earth", have a wavenumber range that spans from 250.03 to 1651.22 cm^{-1} with a resolution of 4.5 cm^{-1}. This second processing method was only implemented for six spacecraft orbits' worth of data which covered very few solar longitudes, namely 30° to 60°E and 210° to 240°. 273 spectra were treated in this method, out of which 93 fall within the latitude range of interest.

Ignatiev et al. (1999) have created an averaged set based on the on-board spectra

Figure 3.5: *Venera 15* on-board and on-Earth averaged spectra. The associated noise equivalence radiances are shown in the dotted black lines. The on-board spectrum is displaced by 500nW $cm^{-2}sr^{-2}(cm^{-1})^{-1}$ for clarity reasons. Also shown are the regions of activity of each species. SO_2 is also shown even though it is not being retrieved in this work.

from 20° to 60°N averaged over six longitudinal bins, whose borders are shown as the white markers in figure 3.4. The number of the on-board spectra was reduced to 42 through this averaging process. Even though in this work the original on-board and on-Earth *Venera 15* spectra are being exploited, it has proven useful to perform certain tests using this averaged dataset used in Ignatiev et al. (1999), as will be discussed in chapter 4. In figure 3.5, the entire range covered by the on-board and on-Earth *Venera 15* spectra is shown. The red line depicts the average of the on-board spectra and the blue line is the average of the on-Earth spectra. The on-board

spectrum is displaced by 500nW $cm^{-2}sr^{-2}(cm^{-1})^{-1}$ for clarity reasons. Also shown are the ranges of effectiveness of the species considered in this work. Even though we are not attempting to retrieve SO_2, some of its spectral features are evident in this figure and hence it is also shown. The water vapour will be retrieved from the pure rotational band at <450 $cm^{-1}$and the rotational-vibrational band at >1300 cm^{-1}. The water molecules that are chemically bound to sulphuric acid and compose Venus' clouds do not of course emit in any of the free water absorption bands. The sulphuric acid droplets exhibit absorption features in the region <450 cm^{-1} and between 800 and 900 cm^{-1}, due to complex rotational-vibrational transitions.

Both *Venera 15* spectral data sets have an associated viewing angle, due to the instrument alignment discussed above. Individual spectra were averaged in the same manner as the *PV OIR* radiances, via a projection onto nine different viewing angles. The maximum amount of different spectra resulting in each bin did not exceed six, as seen in the colour bar of figure 3.4. The distribution of the viewing angle of all *Venera 15* spectra with latitude is displayed in figures 3.6 and 3.7. Following instrument design specifications, the nadir view of the planet was attained at 63°N. In an attempt to try and cover the Southern Hemisphere and near-equatorial region the satellite was rotated on its axis to provide near-nadir views above the equator, in one special session. These special-viewing on-board spectra are depicted as the red stars with high cosine viewing angles in figure 3.6. The results from these spectra have also been separately analysed by Ignatiev et al. (1999), reproduced in figure $2.5_{(3)}$.

Figure 3.6: Viewing angle distribution of the *Venera 15* on-board spectra with latitude. The different longitude markers are slightly shifted in latitude by a few degrees in this plot, for clarity reasons.

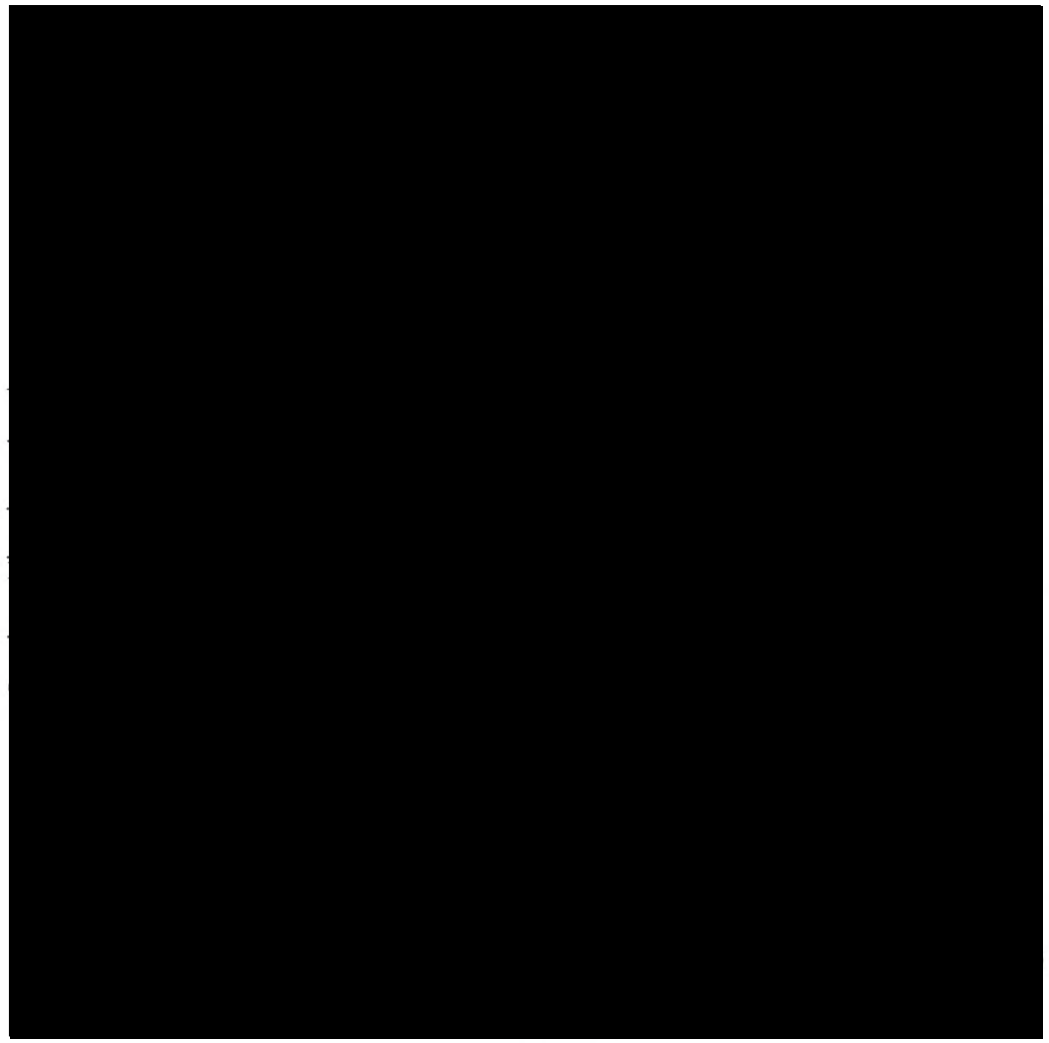

Figure 3.7: Viewing angle distribution of the *Venera 15* on-Earth spectra with latitude. The different longitude markers are slightly shifted in latitude by a few degrees in this plot, for clarity reasons.

3.3 Synopsis

In this section we will recapitulate the important points of the above description of the two instruments; the *Pioneer Venus* orbiter was spin-stabilised and rotated at 5 rotations per minute in a 24-hour polar orbit around the planet. The *Venera 15* orbiter had a fixed instrument orientation but was also placed in a 24-hour polar orbit around the planet. During the 72 days of observation, the *PV OIR* instrument covered most of the Northern Hemisphere, whereas the *Venera 15* FTS mainly covered ~20°N to 90°N for the longitude ranges 60° to 160°E and 230° to 330°E during 64 days of observations. Irrespective of the total coverage of planet by the instruments, this work will focus on the latitude region from ~10°S to 50°N and all covered longitude regions. The *PV OIR* instrument is a radiometer (grating spectrometer) whose five channels measure radiances at 228.0, 679.4, 727.2, 764.4 and 869.5 wavenumbers. In contrast, the *Venera 15* FTS is a Fourier transform spectrometer which measured spectra in two different modes; the on-board processed spectra, which range from 274.34 to 1656.46 cm^{-1} with a resolution of 6.94 cm^{-1} and the on-Earth processed spectra, which range from 250.03 to 1651.22 cm^{-1} with a resolution of 4.5 cm^{-1}.

A timing issue

One of the points of challenge in our analysis has been the fact that the two missions have visited the planet almost four Earth years apart. This point has not deterred this work as it can easily be verified that the two spacecraft arrived at similar Venus

seasons and general atmospheric conditions. Furthermore, the aim of this thesis is not to actually "equalise" the findings of the two instruments but rather to analyse them with the same tools and hence provide confident and unbiased joint results.

During the visit of the Pioneer Venus Orbiter, the sub-solar latitude[3] ranged from -1.3° (Dec 4, 1978) to -2.46° (Southern Solstice, Jan 10, 1979) to -1.47° (Feb 14, 1979). Similarly during the *Venera 15* visit, the sub-solar latitude ranged from 0.46° (Oct 12, 1983) to 0° (Equinox, Oct 18, 1983) to -2.46° (Southern Solstice, Dec 14, 1983). Hence, considering the stability of gross features in the Venus atmosphere described in chapter 1, one would not expect to see *seasonally-induced* differences in the measurements yielded by the two instruments.

The Pioneer Venus measurements were taken under solar maximum conditions whereas the *Venera 15* measurements were recorded during low to medium solar activity. The radio emission from the Sun at a wavelength of 10.7 centimetres, known as the "F10.7 index", quantifies the solar activity. Venus during the Pioneer Venus visit was subjected to an F10.7 flux of about 168-199 whereas during the Venera 15 visit the F10.7 index was at 90-120. Even though changes in the solar cycle occur most strongly in the EUV and UV and both instruments in question are infrared instruments, the Venus cloud absorbs heavily in the UV part of the spectrum. Variations in solar intensity over the solar cycle are ~10% at 190 nm, ~5% at 200 nm and less than 1% at >210 nm (Nicolet, 1989). Unfortunately, quantitative statements cannot be made with regards to the precise effect this, seemingly

[3]The sub-solar latitude is the latitude on the planet directly beneath the Sun, in degrees.

insignificant, intensity change will have on the cloud temperature, composition and structure. In the subsequent analysis, solar conditions are not considered when modelling Venus' atmosphere in order to analyse either set of measurements.

Chapter 4

Joint Retrievals: Theory And Methodology

We do not aim in this chapter to reproduce information that can easily be found in any standard atmospheric physics textbook but rather provide the necessary information for the reader to follow our arguments logically. In each section we discuss not only the theoretical background but also the practical choices made in order to solve the physical equations in question. In section 4.1 the Radiative Transfer Equation is presented in a format applicable to this work. Section 4.2 describes the Atmospheric Model developed in order to solve the aforementioned equation and in section 4.3 the concept of a Forward Model and how that relates to solving the radiative transfer equation is explored. Section 4.4 introduces the mathematical equations required for the retrieval of the atmospheric state observed by the *PV OIR* and *Venera 15 FTS* instruments.

4.1 Radiative Transfer Equation

The Radiative Transfer Equation in the case of calculating the thermal emission from a plane parallel atmosphere in local thermodynamic equilibrium, seen by a nadir viewing instrument, predicts that the upward monochromatic radiation intensity, or radiance, $I(z_r, \mu)$ at any altitude reference level z_r can be expressed by:

$$\boxed{I(z_r, \mu) = \int_{z_r}^{\infty} J^s(z, \mu)\, W(z, \mu)\, dz} \tag{4.1}$$

where μ equals to $\cos\theta$ and θ is the zenith angle[1], $J^s(z, \mu)$ is the source function and $W(z, \mu)$ is the weighting function.

Equation 4.1 describes the radiation observed by the satellite from all atmospheric layers down to z_r. This radiation originates from the fact that, in the infrared range of the spectrum, gas molecules undergo rotational and vibrational transitions. Their spectral lines, which are observed remotely by spectrometers, can then divulge information about the atmospheric temperature and the distribution of the gases themselves. The radiation source function, $J^s(z, \mu)$, in principal, includes contributions to the observed radiance from thermal emission, single and multiple scattering. For the case of the *PV OIR* and *Venera 15* experiments, only the contribution from thermal emission is considered, hence:

$$J^s(z, \mu) = B(T) \tag{4.2}$$

$$\text{and,} \quad W(z, \mu) = \frac{d\tau(z_r, z, \mu)}{dz} \tag{4.3}$$

[1] A number of obvious sub- and superscripts, e.g. the wavenumber, $\widetilde{\nu_0}$, dependence, are omitted in the following equations for clarity reasons.

where $\widetilde{\nu_0}$ is the wavenumber, in cm^{-1}, τ is the transmittance and $W(z_r, \mu)$ will be henceforth called *the weighting function*, a measure of the single-layer contribution to the radiance at the reference level z_r. $B(T)$ is the Planck function given by:

$$B(T) = \frac{2hc^2\widetilde{\nu_0}^3}{\exp(hc\widetilde{\nu_0}/kT) - 1} \tag{4.4}$$

where, h is Plank's constant, 6.626×10^{-34} J s, c is the speed of light, 2.99×10^8 m s^{-1} and k is Boltzmann's constant, 1.38×10^{-23} J/K. The transmittance, τ, is given by:

$$\tau(z_r, z, \mu) = \prod_{i=1}^{M} \exp\left[-\frac{1}{\mu}\chi(z_r, z)\right] \tag{4.5}$$

where, $\tau(z_r, z, \mu)$ is the *transmittance* of the layer (z_r, z), $\chi(z_r, z)$ is the *optical depth* of extinction of the layer and M is the number of species active in the infrared range of the spectrum. The optical depth is given by:

$$\chi^{ext}(z_r) = \int_{z_r}^{\infty} \beta^{ext}(z)\, dz \tag{4.6}$$

$$\text{where, } \beta^{ext}(z) = \sum_{g=1}^{M}(\beta_g^{abs} + \beta_g^{sca}) + \beta_p^{abs} + \beta_p^{sca} \tag{4.7}$$

where, $\beta^{ext}(z)$ is the volume extinction coefficient and comprises of the following terms: β_g^{abs} is the gas absorption contribution and β_g^{sca} is the gas scattering contribution, β_p^{abs} is the aerosol (particle) absorption contribution and β_p^{sca} is the aerosol scattering contribution. We can safely disregard the contribution by Rayleigh (molecular) scattering due to its λ^{-4} dependence as we are interested in the infrared region between 10 and 200 μm. We can also omit the contribution due to scattering by the particles; we have performed calculations that showed that the inclusion of

scattering does not lead to significantly difference radiances than those calculated from thermal emission models alone[2]. This reduces equation 4.6 to equation 4.8.

$$\chi^{ext}(z_r) = \int_{z_r}^{\infty} (\beta_p^{abs} + \sum_{g=1}^{M} \beta_g^{abs})\, dz \tag{4.8}$$

The total transmittance equation which will be used in our solution to the radiative transfer equation is given in equation 4.9.

$$\tau(z_r, \mu) = \exp\left[-\frac{1}{\mu}\int_{z_r}^{\infty} (\beta_p^{abs} + \sum_{g=1}^{M} \beta_g^{abs})\, dz\right] \tag{4.9}$$

4.2 The Atmospheric Model

The atmosphere of Venus has been discussed qualitatively in section 1.2. In order to create a mathematical model of this atmosphere, vertical profiles for temperature, pressure, volume mixing ratios for each radiatively active gaseous species and aerosol mass loading have been constructed from previous measurements and published references.

Temperature and Pressure

The temperature structure of Venus' middle atmosphere was observed by the *Pioneer Venus Large* and *Small* probes, the *P V Orbiter Radio Occultation* and the *PV OIR* experiments. Seiff (1983) and references therein have revised quite extensively the temperature and pressure structure of Venus' middle atmosphere from the cloud tops to 100 kilometres altitude, based on the aforementioned Pioneer Venus and

[2]The general importance of the inclusion of scattering to solving the radiative transfer equation is further demonstrated in appendix A.1.

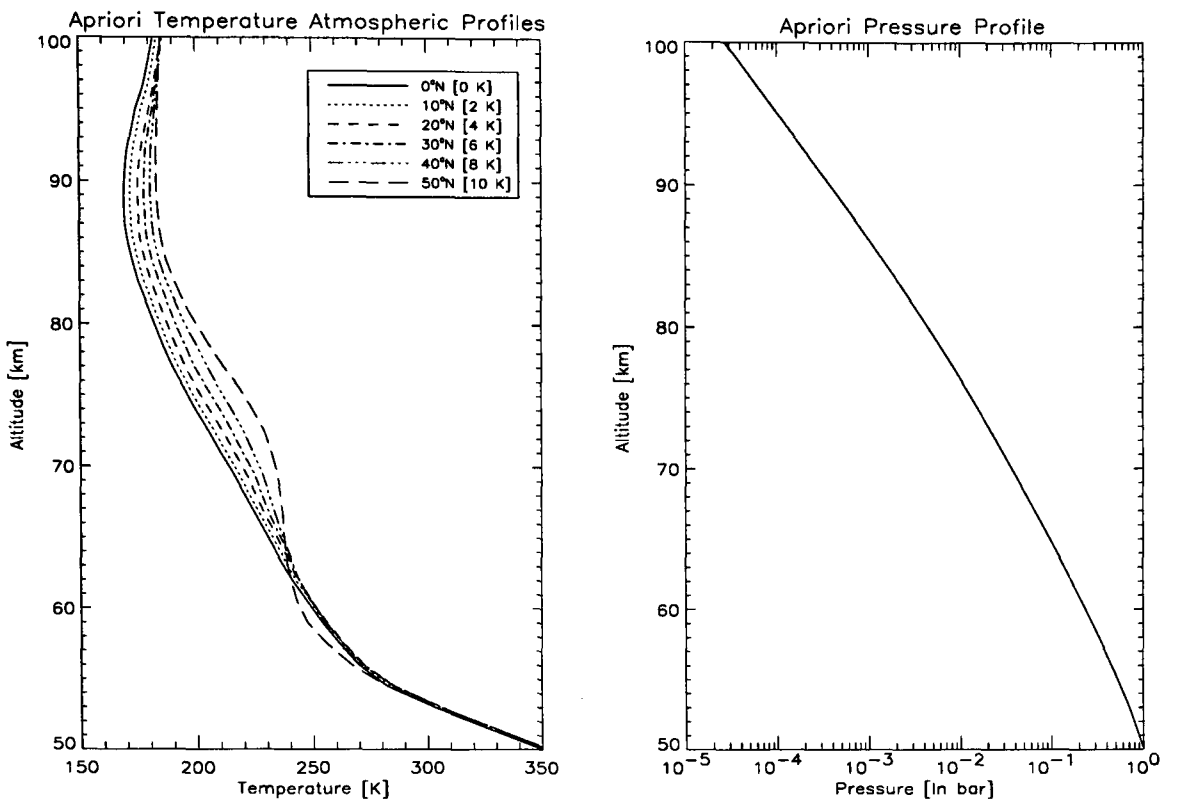

Figure 4.1: Right panel: the pressure profile (logarithmic scale) used in the model corresponding to the 0°N temperature profile. Left panel: the six temperature profiles used as *a priori* temperature profiles vs altitude [km]. The corresponding latitude is shown in the legend, along with the degrees Kelvin each profile has been shifted by for clarity. The beginning of the temperature inversion (polar collar) can be seen in the 50°N profile.

numerous Venera experiments. The latitudinal dependence of the temperature structure was found to be very small up to the 50°N parallel, whereas there exist almost no zonal temperature gradients, as revealed by the Pioneer Venus Probes and occultation experiments (Seiff et al., 1980; Kliore and Patel, 1980). Six temperature profiles derived from these works were used as *a priori* temperature profiles and their corresponding latitudes are shown in the legend in figure $4.1_{(1)}$, along with the degrees Kelvin each profile has been shifted by for clarity. The latitude/longitude structure of the temperature profiles used as *a priori* information in this work is shown in figure A.1. Pressure differences were also reported to be small below the 100 kilometre altitude for the equatorial and mid-latitude regions. For this reason the

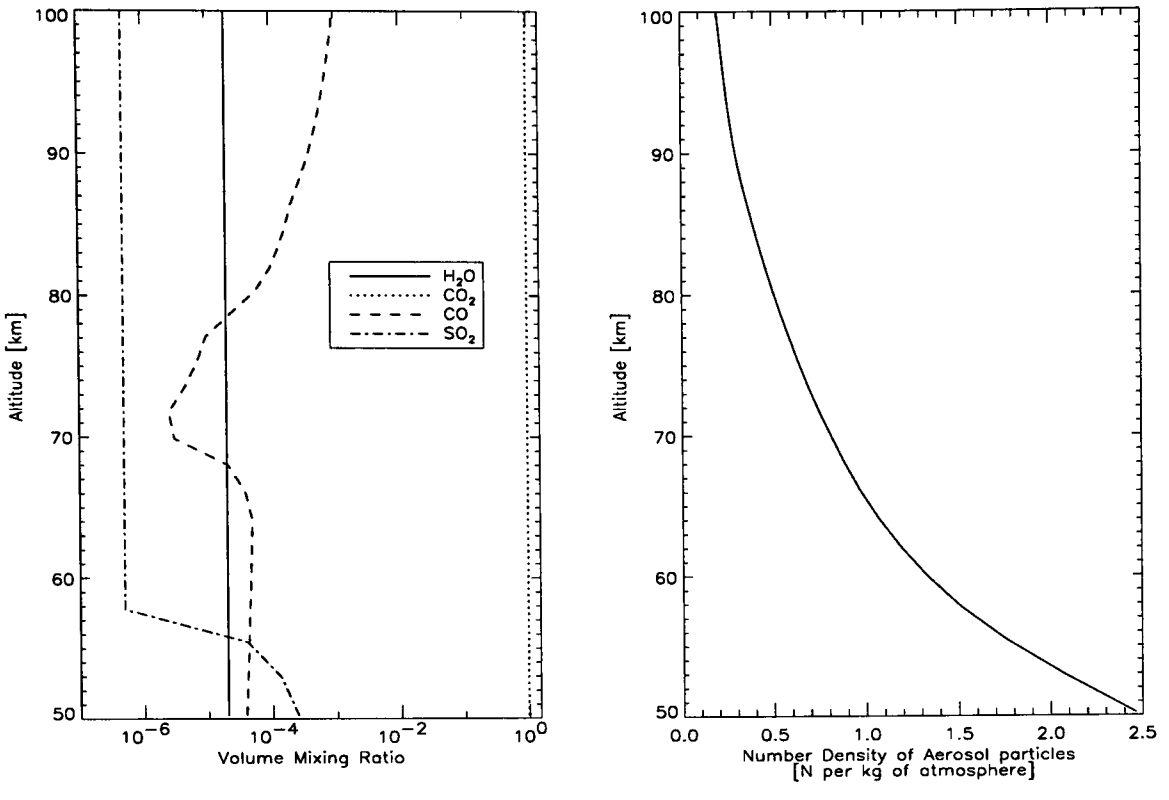

Figure 4.2: Atmospheric gases volume mixing ratio and aerosol number density profiles vs altitude.

pressure profile used in the atmospheric model was kept constant with the reference altitude of 50 km corresponding to the 1 bar level (Kliore and Patel, 1982). The pressure profile above that altitude is given by the hydrostatic integration of the temperature profile and the profile corresponding to the temperature profile of 0°N is shown in figure $4.1_{(2)}$.

Major and Minor Gases

The Venus atmospheric model contains a well-mixed 96.5 $\pm$ 0.8% CO_2 profile, depicted as the dotted line of figure $4.2_{(1)}$, derived from *in situ*Pioneer Venus measurements (Oyama et al., 1980). The remaining 3.5 $\mp$ 0.8% of the atmospheric mass belongs to N_2, but since it is radiatively inactive in the infrared region, N_2 is only included in the calculation of the ideal gas law for conservation of mass purposes.

Three minor but radiatively active gases whose vertical profiles are also shown in the same figure complete the atmospheric model. The water vapour profile is seen here (solid line) as constant with height, but as will be discussed in section 4.4, H_2O abundance is one of the quantities to be retrieved from the measurements. The CO profile (dashed line) depicts a depletion of the species between 70 and 80 km altitude, as derived by Galileo-NIMS data (Collard et al., 1993). COhas a few, albeit weak, lines between 50 and 200 cm^{-1}hence was included in the atmospheric model. No local solar time variability of the COprofile was accounted for, due to its relatively low line strength. The SO_2 profile (dash-dotted line) follows the work of von Zahn et al. (1983). Other minor gases, such as HCl, HF and H_2S, have been known to exist in small and possibly crucial quantities in Venus' middle atmosphere. After von Zahn et al. (1983), table III, page 325, the abundance of HCl is ~0.4 ppm, of HF is ~5 ppb and of H_2S is ~1-3 ppm at the cloud top regions. However, inspecting the *Hitran* 96 spectroscopic data base (Rothman et al., 1998) has verified that these species do not exhibit many lines in the infrared wavenumber range of interest and none of them are strong and significant to this work.

The number density of the aerosol, in number of particles per unit volume $n(r)$, is calculated as follows. The nominal cloud extends from 50 to 100 km, the maximum cloud density is set to 100 N cm^{-3} at the altitude of 50 km (see figure 1.6.) In order to transform the number density (N cm^{-3}) to a number of particles per gramme of atmosphere (N g^{-1}), the ideal gas equation is utilised to calculate the atmospheric density in g cm^{-3}. The level of *unit optical depth* (referred to as "cp0") through this

cloud is one of the parameters to be derived from the measurements and so does not remain constant. In the nominal calculation, this level set to the 120 mbars (~63 km) level (Marov et al., 1980). The second cloud parameter to be derived is the *fractional scale height*, i.e. the fraction of the cloud scale height to the atmospheric scale height (referred to as "hc"). One can also envision this as the rate of change of cloud mass density with atmospheric mass loading. In the nominal retrieval calculation this value is set to 0.85 (Esposito et al., 1983). An *a priori* cloud number density profile can be seen in figure $4.2_{(2)}$.

Hence, from these profiles, the atmospheric density, absorber amounts, partial pressures and effective temperature are calculated from first principles.

4.2.1 Molecular Absorption Coefficient Calculation

The atmospheric absorption spectrum of a molecule is an array of *spectral absorption lines* that correspond to transitions between the discrete energy levels of the molecule. At infrared wavelengths, vibrational and rotational transitions take place. In addition to these discrete absorption characteristics, a *continuum* of absorption might be present between the absorption lines, possibly due to collisionally-induced absorptions, adding to the observed radiation. In this section, the method of calculating the molecular absorption coefficient of the gases present in Venus' atmosphere is discussed.

In order to perform the integral calculation required by equation 4.1 the model atmosphere is split into homogeneous paths (or layers) of constant temperature

and pressure so that the monochromatic absorption coefficient of the gases and aerosol can also be considered constant along that path. Following equation 4.9 the monochromatic transmittance of an atmospheric layer between z_r and z_o due to molecular absorption is calculated as follows:

$$\begin{aligned}\tau(z_r, z_o, \mu) &= \prod_{i=1}^{M} \exp\left[-\frac{1}{\mu}\int_{z_r}^{z_o} \beta_i^{abs}(z)\, dz\right] \\ &= \prod_{i=1}^{M} \exp\left[-\frac{1}{\mu}\int_{z_r}^{z_o} k_i(z) n_i(z) dz\right]\end{aligned} \tag{4.10}$$

where, $k_i(z)$ is the monochromatic absorption cross-section of molecule i, n_i is the corresponding number density calculated from the profiles shown in figure 4.2 and M is the number of different gases active in the infrared range of the spectrum.

As mentioned above, in a real atmosphere each absorption line will have a *strength*, S, given by $S = \int_\nu k_\nu\, d\nu$, where k_ν is the absorption cross-section. For a single line, this absorption cross-section can be expressed in the form (c.f. Andrews et al. (1987), pp. 38-40):

$$k_\nu = S\ f(\widetilde{\nu} - \widetilde{\nu}_0) \tag{4.11}$$

where $f(\widetilde{\nu} - \widetilde{\nu}_0)$ is a shape factor (profile) giving the relative absorption cross-section at a point displaced by $(\widetilde{\nu} - \widetilde{\nu}_0)$ from the line centre $\widetilde{\nu}_0$. In the following, the choices of shape factors for the different gases used in this analysis are described followed by the chosen way of calculating k_ν.

Spectral lines can have their shape altered either by *natural*, *pressure* or *Doppler* broadening processes. The first two processes can be described adequately by the *Lorentz* line shape and the last one by the *Gaussian* line shape (Andrews et al.,

1987). In a region of the atmosphere where both these mechanisms are important, the shape factor $f(\widetilde{\nu} - \widetilde{\nu_0})$ is given by the convolution integral of the Lorentz and Doppler shapes, resulting in the *Voigt* lineshape (Armstrong, 1967). The Voigt profile resembles the Doppler profile near the line centre $\widetilde{\nu_0}$ and the Lorentz profile near the line wings and is a standard line shape to assume for all absorption coefficients required in our atmospheric model. The Humlicek (1982) formalism was used to mathematically calculate this Voigt lineshape. Contributions from individual absorption lines at 35 cm^{-1} distance from the line centre were considered. The water vapour continuum spectra due to collisionally-induced absorption are also included in the calculation using the semi-empirical approach of Clough et al. (1980) and Clough et al. (1989) (CKD version 2.1). For CO_2, the line shape is further complicated in that its absorption lines at 15 μm have been known to exhibit sub-Lorentzian behaviour in the line wings (c.f. Strow and Reuter (1988), Ma et al. (1999)). The absorption cross-section is then expressed in the form:

$$k_\nu \;=\; S\; f(\widetilde{\nu} - \widetilde{\nu_0})\; \chi(|\widetilde{\nu} - \widetilde{\nu_0}|) \tag{4.12}$$

where, $\chi(|\widetilde{\nu} - \widetilde{\nu_0}|)$ is an empirical form factor, experimentally determined. In this work we have opted for the self and foreign induced absorption form factor provided by the works of Cousin et al. (1985) and Le Doucen et al. (1985). The line strengths, S, for the gases considered have been scaled to the desired temperatures using the formalism of Gamache et al. (1990) and are shown in appendix C (Rothman et al., 1998).

In order to calculate the monochromatic absorption coefficient for homogeneous

paths, the most precise, but computationally costly method is the *line-by-line* calculation. In this method, the line shape parameters for each of the radiatively active species are used directly from the line data base for each wavenumber considered. The whole process is thence very time-consuming, albeit highly accurate. In this work, we have opted to make partial use of the line-by-line method, for tabulating the line absorption coefficients which are ranked according to their line strength. A numerical distribution of absorption coefficient strengths has been constructed known as the "k-distribution" or the "correlated-k" distribution (c.f. Goody et al. (1989), Lacis and Oinas (1991)). The shortened version of this calculation is as follows:

Since k_ν is a highly repetitive function of wavelength, the integration over wavelength of equation 4.10 can be replaced with reordering the k_ν in some predefined spectral intervals with similar absorption coefficient strength. The absorption coefficient range is subdivided into a suitable number of intervals of width Δk_i. The frequency distribution of absorption coefficient strengths is obtained directly from the absorption coefficient spectrum by binning and summing wavenumber subintervals $\Delta\nu_j$ which have absorption coefficient strengths within the range k_i and $k_i + \Delta k_i$:

$$f(k_i) = \frac{1}{\nu_2 - \nu_1} \sum_{j}^{M} |\frac{\Delta\nu_j}{\Delta k_i}| W(k_i, k_i + \Delta k_i) \tag{4.13}$$

where, $W(k_i, k_i + \Delta k_i)$ is a Krönecker-δ type function, i is the bin number counter and j is the spectral interval counter. Hence, the cumulative frequency distribution increments, $\Delta g_i = f(k_i)\Delta k_i$, define the fraction of the spectral interval $[\nu_1, \nu_2]$ for

which the absorption coefficient k_ν is between k_i and Δk_i. The cumulative frequency distribution is then:

$$g(k_n) = \sum_{i=1}^{n} f(k_i)\Delta k_i \tag{4.14}$$

The inverse of the cumulative frequency distribution, $k(g)$ is known as the k-distribution, or k-table, and is given by $k_n(g) = g^{-1}(k_n)$.

In this work, k-tables were compiled using the *Hitran* 96 spectroscopic line database (Rothman et al., 1998), with the specified line shapes mentioned above. The absorption coefficients have been tabulated for nine temperatures, between 160 and 340 K, and ten pressures, between 1 and 10^{-10} bar. Two identical k-table sets were created, one for the *PV OIR* and one for the *Venera 15* spectra wavenumber ranges and resolutions. Thus, the transmittance of each species is evaluated for each atmospheric layer (path) into which the atmosphere has been split using equation 4.10.

For completion purposes, we mention here that Schofield and Taylor (1982) used the Yamamoto et al. (1969) line shapes for CO_2. A k-table using this data set was also created for comparison purposes, but tests showed that the transmittances calculated with the Yamamoto et al. (1969) lines were not significantly different to those calculated with the nominal CO_2 k-tables used in this work. We also note that Ignatiev et al. (1999) used the *line-by-line* calculation for evaluating the absorption coefficients using the *Hitran* 92 line data base (Rothman et al., 1992). They chose a sub-Lorentzian form factor for the 15 μm CO_2 band based on data by Moskalenko and Parzhin (1981), and they also adopted the Voigt profile for the water vapour

absorption lines.

Transmission function comparison

In this section, possible sources of discrepancy between this work and the one of Schofield et al. (1983) introduced by the different ways of treating the water vapour absorption coefficients are discussed. Initially we briefly reproduce the work of Schofield et al. (1983) to facilitate this comparative study.

In Schofield et al. (1983) the water vapour transmission functions were derived from empirical expressions fitted to line-by-line calculations using the Air Force Gas Library (AFGL) line parameter compilation of Rothman (1981). Voigt line profiles were adopted for the H_2O molecule. Further to that, they performed laboratory measurements in a 33-meter path White Cell[3] in order to validate that semi-empirical calculation. The results from both these calculations have been reproduced from the paper and are shown in figure 4.3. In their analysis, the authors thence used a compiled table of absorption coefficients that span the entire range of temperatures and pressures found in the Venus atmosphere. Schofield et al. (1983) noted that the difference between the experimental and theoretical transmission functions is 0.03 in logarithmic scale, or 7% in relative terms. As pressure and water vapour amount were varied simultaneously in the White Cell measurements, the corresponding uncertainty in the amount of water vapour above a fixed pressure level was estimated to be 15%.

[3]A White Cell is an experimental apparatus in the form of a multi-path cell that permits the measurement of gaseous absorption over long paths.

Figure 4.3: Theoretical (blue line) and experimental (red crosses) transmission function calculations for H_2O from Schofield et al. (1983) and theoretical transmission function calculations (black lines) from this work. The original experimental cell path was 33 meters and contained 100% water vapour at 300 K temperature. Also shown is the transmission calculated for a 1 kilometre path length (black line with square dots) in order to demonstrate the enormous sensitivity of these calculations.

Graphically, our transmission function calculated using the correlated-k technique with the Rothman et al. (1998) line parameter compilation and the Voigt H_2O line profile, is shown as the black line with star markers in figure 4.3. Our theoretical calculations and the experimental curve of Schofield et al. (1983) (red crosses) seem to agree well at the lower and higher ranges of pressure and not so well in the middle values. The percentage difference between the transmission function of our calculations and the ones of Schofield et al. (1983) is 11.2% and 16.1% for their theoretical and experimental calculations respectively, at the -2.25 point of the logarithmic pressure scale. One might hence note that the absolute retrieved water vapour amounts of the Schofield et al. (1983) work and this one cannot *de*

facto agree, but the general water vapour features (e.g. day-night enhancements, wet spot) are still expected to be retrieved.

4.2.2 Cloud Absorption Coefficient Calculation

Similarly to equation 4.10, the monochromatic transmittance of an atmospheric layer between z_r and z_o due to the cloud absorption is calculated as follows:

$$\begin{aligned}\tau(z_r, z_o, \mu) &= \exp\left[-\frac{1}{\mu}\int_{z_r}^{z_o} \beta_g^{abs}(\nu)\, dz\right] \\ &= \exp\left[-\frac{1}{\mu}\int_{z_r}^{z_o} \sigma^{ext}(r,\nu)\, n(z) dz\right]\end{aligned} \tag{4.15}$$

where, σ^{ext} is the extinction cross-section[4] and $n(r)$ is the number of particles of radius r per unit volume. The calculation of the $n(r)$ profile has already been described in section 4.2.

In order to estimate $\sigma^{ext}(r,\nu)$ we have used the H_2SO_4 refractive index data of Jones (1976) for the wavenumber range 200 to 430 cm^{-1} and Biermann et al. (2000) for the wavenumber range 430 to 1700 cm^{-1}. Mie theory (Mie, 1908) was employed to convert the refractive index data into the cloud extinction cross-section and single scattering albedo. The nominal[5] cloud is composed of 75% H_2SO_4 (and 25% H_2O) spherical droplets of mean radius, r_o, 1.05 μm (Hansen and Honevier, 1974). The particle size distribution, $N(r)$ was assumed to be log-normal, with standard deviation, σ_g, of 0.07 (equation 4.16.)

[4]Traditionally, the combination of atmospheric absorption and scattering is called *extinction* (as in equation 4.7) but since scattering is not considered in this work, absorption and extinction can be thought of as synonymous.

[5]By the term "nominal" we refer to the standard calculation done in this work. The *a priori* parameters chosen for the nominal calculation are all tabulated in table A.1, appendix A.

$$N(r) = \frac{1}{(4\pi)^{1/2}} \frac{1}{r} \frac{1}{\sigma_g} \exp\{-\frac{1}{2}[\frac{\ln(r) - \ln(r_o)}{\sigma_g}]^2\} \tag{4.16}$$

where, r is the particle radius. The absorption due to aerosol particles can be thus calculated for the atmospheric paths defined.

For comparison purposes we note here that Ignatiev et al. (1999) used a log-normal particle size distribution with a radius r = 1.05 μm and variance $\sigma_g = 1.10$. All cloud particles were assumed to be composed of an aqueous solution of the sulphuric acid whose optical properties were defined from Palmer and Williams (1975) and Jones (1976). The authors reach the conclusion that the equilibrium concentration varies with altitude, and most probably latitude as well, and they estimate a value between 67% and 83% in H_2SO_4 acidity.

4.2.3 Synopsis of presented material

In the beginning of this chapter, the radiative transfer equation was discussed for the case of a nadir viewing instrument measuring the thermal emission of a planetary atmosphere in the infrared and far-infrared range of the spectrum (section 4.1.) The atmospheric model developed was then described (section 4.2) followed by the practical ways that the transmittances due to the atmospheric gases (section 4.2.1) and the sulphuric acid cloud (section 4.2.2) were calculated.

In the remainder of this chapter, the methodology with which physical parameters are translated into the mathematical equations of the retrieval scheme is established. The retrieval process itself is fully described and the diagnostic

possibilities of the error analysis are expanded upon.

4.3 The Forward Model

In order to bridge the physics discussion of the previous section with the mathematical formalism of the retrieval process developed in the next section, a short terminology discussion follows. The *Forward Model*, $F(x)$, simulates the radiance a specific instrument would have measured, had the atmospheric state been the input state vector. The radiance is calculated by solving equation 4.1. The measurement vector, y, has m elements, for m observations made. The state vector, x, contains the quantities to be retrieved and has n elements.

Hence, we may state that:

$$y = F(x) + \epsilon \tag{4.17}$$

where, x is the state vector, y is the measurement vector with error ϵ and $F(x)$ is a function that encapsulates our understanding of the physics behind the measurement. This term is substituted further on with the symbol y_n. In this work, "the measurement" is the thermal emission radiance recorded both by the *PV OIR* and the *Venera 15* experiments and "the state vector" contains three different atmospheric quantities: the pressure level of unit optical depth through the Venus cloud, cp0, the fractional scale height of the Venus cloud, hc, the water vapour column abundance and a 30-level temperature profile from 50 to 100 km altitude, hence n=33.

In order to be able to solve equation 4.17, it can be linearised by expanding

it about some reference state x_o as shown below (ignoring the higher terms in the Taylor series):

$$\begin{aligned} y - F(x) &= \left.\frac{\partial F(x)}{\partial x}\right|_{x_o} (x - x_o) + \epsilon \\ &= \mathcal{K}(x - x_o) + \epsilon \end{aligned} \tag{4.18}$$

where the sensitivity kernel, $\mathcal{K}$-matrix, represents the sensitivity of the forward model to the quantities to be retrieved. The $\mathcal{K}$-matrix is often called "weighting function" in other works. However, in order to avoid confusion with the weighting functions defined in equation 4.3, we will solely refer to the $\mathcal{K}$-matrix as the sensitivity kernel and not as the weighting function.

The forward model used in this work has been presented in section 4.2, but we deem it important to summarise here the basic ideas. The model atmosphere is split into layers, whose mean temperature, pressure, absorber (gas) and cloud (aerosol) amounts are calculated from first principles. Depending on the viewing geometry, the path through the atmosphere from where radiation reaches the instrument is defined. The transmittance of each gas species in this path is computed using the absorption coefficients from the pre-tabulated k-tables. The transmittance of the aerosol is similarly computed using the extinction coefficients pre-evaluated from Mie theory. The total optical depth of the path through the atmosphere is thus composed and the total radiance due to thermal emission is evaluated for the specific wavenumber range and resolution.

4.4 The Retrieval Method

The radiative transfer equation 4.1 represents the *Forward Problem*; given the state of the atmosphere, the solution to this equation predicts the radiation incident at the satellite. Having discussed how we solve this equation in section 4.3, we are now faced with the *Inverse Problem*, i.e. given the radiance measurements what is the state of the atmosphere that produces this radiation. In the following section, we are discussing the mathematical background and formulation we have used in order to solve the inverse problem, in order to *retrieve* useful information from the available measurements.

For purposes of illustration, we have chosen a specific latitude/longitude bin of data to be used as a case study throughout this section, namely the 30°N, 240°E bin. For the *PV OIR* data set, this bin contains the maximum possible number of measurements, namely nine different viewing angles, whereas the *Venera 15* experiment registered four spectra projected onto two viewing angles. Where appropriate, the dataset created by Ignatiev et al. (1999) will also be used for demonstration purposes.

4.4.1 Optimal Estimation Retrieval Technique

The optimal estimation retrieval scheme chosen in this work in order to optimise the treatment of measurement errors is the one first presented in Rodgers (1976). In this section we will be using most of the formalism and the format of the equations seen in Rodgers (2000). Appendix A has been created to hold all numerical choices

made while constructing the analysis tools, along with their bibliography references.

The optimal estimation retrieval is based on Bayers theorem of treating probability functions (Bayers, 1763). Consider two states, x and y. The probability that x and y will occur together is denoted by P(x,y). The probability that x will occur when y occurs is denoted by P(x|y). So, the probability that x and y will occur is given by the probability that x will occur when y will occur multiplied by the probability that y will occur, i.e. P(x,y)=P(x|y) P(y). The vice versa also holds, i.e. P(x,y)=P(y|x) P(x). Hence, Bayer's theorem states that:

$$P(x|y) = \frac{P(y|x)P(x)}{P(y)}$$

$$P(x|y) \propto P(y|x)\ P(x) \tag{4.19}$$

In our problem, P(y|x) is the probability that a measurement y will be made when the atmospheric state is x. The measurements y contain errors given by S_ϵ. P(x) contains the information on x prior to making any measurements. This information depicts previous knowledge/measurements on the general state of the atmosphere and is known as the *a priori* information, x_a. The *a priori* information has an associated *a priori* error covariance matrix to quantify our confidence on the previous knowledge of the atmosphere, given by S_a. The selected *a priori* and covariance matrix should cover, and in a sense predict, all possible observable atmospheric conditions so as to encompass the atmospheric variability observed by the measurements.

Assuming Gaussian distributions for both the *a priori* and measurement covari-

ance errors, these two probabilities are given by:

$$P(y|x) \propto \exp[-\frac{1}{2}(y - y_x)^T \; S_\epsilon^{-1} \; (y - y_x)] \tag{4.20}$$

$$P(x) \propto \exp[-\frac{1}{2}(x - x_a)^T \; S_a^{-1} \; (x - x_a)] \tag{4.21}$$

where, y_x denotes the forward problem. Substituting equations 4.20 and 4.21 into equation 4.19 and taking the natural logarithm, we obtain the equation of the *cost function*:

$$\ln P(x|y) \propto \phi_x \; = \; (y - y_x)^T \; S_\epsilon^{-1} \; (y - y_x) + (x - x_a)^T \; S_a^{-1} \; (x - x_a) \tag{4.22}$$

By minimising the cost function equation the most probable value of x, given the measurements y, may be found. The first part of the right hand side of equation 4.22 is traditionally known in literature as *chi-squared* and so in order to avoid confusion, the cost function minimised in the optimal estimation formalism will be denoted by ϕ_x. The zero of the gradient of this cost function will be found using Newton's iterative method, given by equation 4.23.

$$x_{i+1} \; = \; x_i - [\nabla_x(\phi_x)]^{-1} \; \phi_x \tag{4.23}$$

$$\text{and,} \;\; \nabla_x(\phi_x)^{-1} \; = \; [\mathcal{K}^T \; S_\epsilon^{-1} \; \mathcal{K} + S_a^{-1}]^{-1} \tag{4.24}$$

where, $\mathcal{K}$ has replaced by $\nabla_x(y_x)$. Substituting equations 4.22 and 4.24 into equation 4.23, we obtain the *Newton-Gauss method* for iteratively solving the retrieval problem:

$$x_{i+1} = x_i - (S_a^{-1} + \mathcal{K}_i^T\ S_\epsilon^{-1}\ \mathcal{K}_i)^{-1}(-\mathcal{K}_i^T\ S_\epsilon^{-1}\ (y - y_i) + S_a^{-1}\ (x - x_a)) \qquad (4.25)$$

where, $\mathcal{K}_i = \mathcal{K}(x_i)$. By expressing x_{i+1} as a departure from x_a rather than x_i, equation 4.25 is rearranged to give the iterative solution used here, equation 4.26.

$$\boxed{x_{i+1} = x_a + (S_a^{-1} + \mathcal{K}_i^T\ S_\epsilon^{-1}\ \mathcal{K}_i)^{-1}\mathcal{K}_i^T\ S_\epsilon^{-1}\{(y - y_i) + \mathcal{K}_i(x_i - x_a)\}} \qquad (4.26)$$

$$\text{with total covariance, } \hat{S}\ =\ (\mathcal{K}_i^T\ S_\epsilon^{-1}\ \mathcal{K}_i + S_a^{-1})^{-1} \qquad (4.27)$$

where, x_{i+1} is the new solution of the state vector, x_a is the *a priori* value for the state vector and x_i is the current solution. The initial value for the state vector, x_o, can, but need not be, x_a.

A Levenberg-Marquardt-type constraint (Levenberg, 1944; Marquardt, 1963) was also employed in order to complement the Newton-Gauss iteration. In slightly non-linear problems, the true solution might be far from the current starting point and the iterative step taken might increase rather than decrease the residual. So as to avoid meaningless steps, the following restraint was used (c.f. appendix B.1 for more details):

$$x'_{n+1} = x_n + \frac{(x_{n+1} - x_n)}{1 + \lambda} \qquad (4.28)$$

where, λ is the Marquardt-Levenberg-type "braking parameter".

For completion purposes, the retrieval techniques employed in Schofield et al.

(1983) and Ignatiev et al. (1999) have been reproduced in appendix B.2.

Schematic explanation of the retrieval process

The schematic explanation of the retrieval process employed in this work is shown in figure 4.4. The retrieval process is initialised with the following information: the *a priori* state of the atmosphere, i.e. temperature, pressure, presence of absorber and concentrations (section 4.2), the λ-parameter (equation 4.28), the correlation length H (equation 4.29), the correlated-k tables and a user-defined ϕ limit to signal the attainment of convergence. All of the above is entered as input to the forward model (equation 4.1), which returns the predicted radiances, y_n. The initial cost function, ϕ_i, (equation 4.22), is calculated at this stage.

The iterative process thus begins with the first iteration of the retrieval equation 4.26, with further inputs: the measurement error, S_ϵ, the *a priori* covariance error, S_a and of course the measured radiances, y. The retrieval equation provides the first estimate of the solution, x_{test}. Equation 4.28 is applied to avoid nonphysical deviations from a realistic atmospheric state vector. The x_{test} solution is used to solve the radiative transfer equation a second time and y_n is obtained. The current cost function ϕ_n is then calculated and the retrieval proceeds as follows:

- If $\phi_{new} > \phi_{old}$, the state and forward model vectors are not updated to x_{test} and y_n respectively and the λ-parameter is increased to $\lambda_{new} = 10\lambda_{old}$.
- If $\phi_{new} < \phi_{old}$, a double check is performed:
  - If $\frac{\phi_{old} - \phi_{new}}{\phi_{new}} > \phi_{\text{lim}} \rightarrow$, the λ-parameter is decreased to $\lambda_{new} = 0.3\lambda_{old}$, the state and forward model vectors are updated and iteration proceeds

to the next step.

– If $\frac{\phi_{old} - \phi_{new}}{\phi_{new}} < \phi_{\text{lim}} \rightarrow$ convergence has been achieved and the retrieval process can stop.

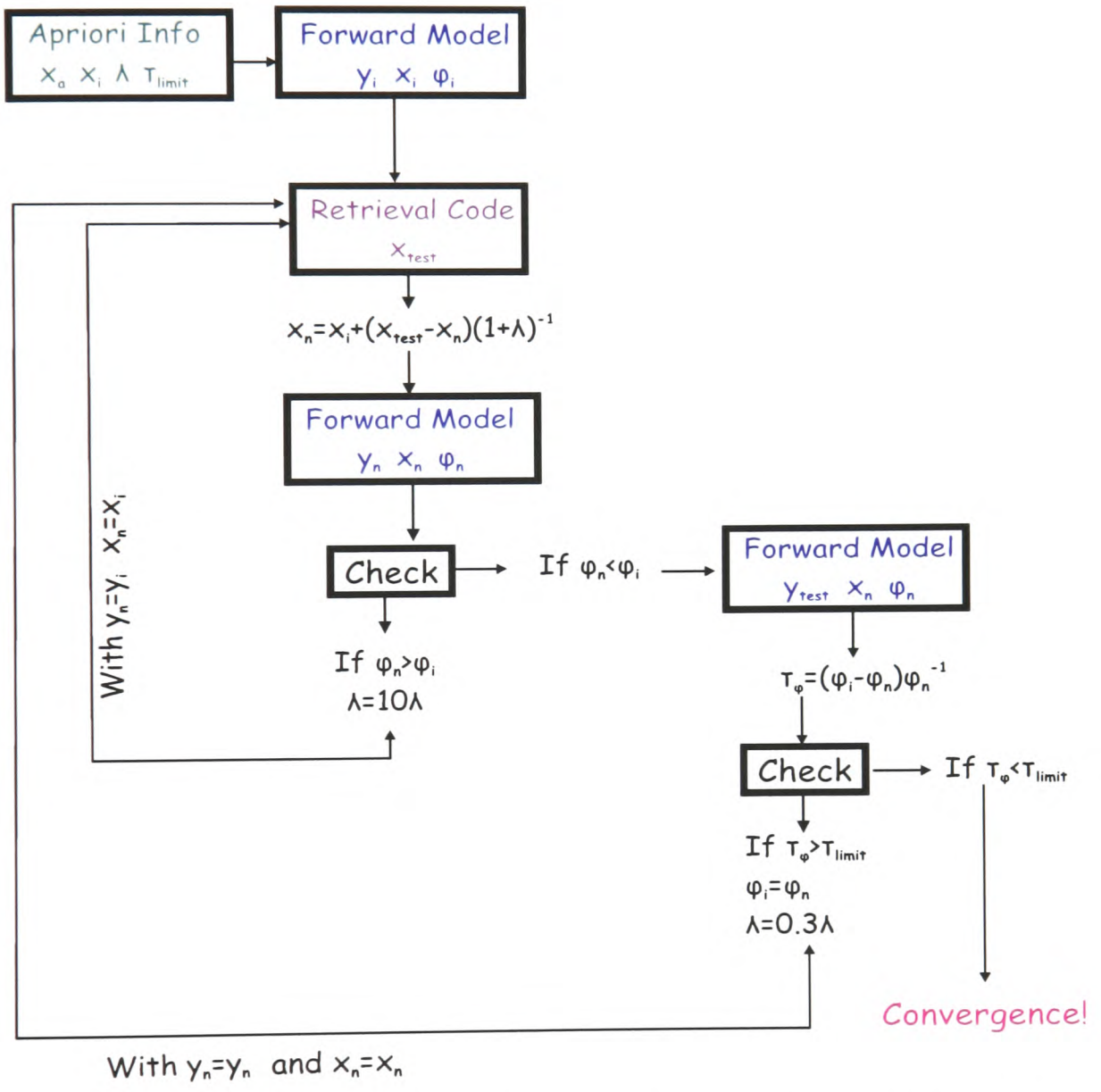

Figure 4.4: Schematic representation of the iterative retrieval process employed.

4.4.2 Error Analysis and Formalisms

This retrieval formalism provides us with three very useful validation analysis tools, the *sensitivity kernels*, $\mathcal{K}$-matrix, the *contribution functions*, $\mathcal{G}_y$-matrix and the *averaging kernels*, $\mathcal{A}$. The sensitivity kernels, or the columns of the $\mathcal{K}$-matrix, can

be seen in figure $4.5_{(2)}$ for the *PV OIR* measurements[6]. The sensitivity kernels peak slightly lower in altitude than the weighting functions, shown in figure $4.5_{(2)}$ since they normalised by the Planck function, $B(T)$.The gain matrix, $\mathcal{G}$-matrix, is defined as $\mathcal{G}_y = (S_a^{-1} + \mathcal{K}^T S_\epsilon^{-1} \mathcal{K})^{-1} \mathcal{K}^T S_\epsilon^{-1}$. The columns of the $\mathcal{G}$-matrix are known as the contribution functions and they represent the contribution made by each radiance measurement to the final retrieved profile or parameter. The averaging kernel, $\mathcal{A} = \mathcal{G}_y \mathcal{K}$, gives the sensitivity of the retrieval to the true atmospheric state. The rows of the $\mathcal{A}$-matrix, shown in figure $4.5_{(3)}$, can be regarded as smoothing functions. The rows of $\mathcal{A}$ are peaked functions with a half-width that is an indication of the spatial resolution of the measurements.

The retrieved temperature profile for the case study is shown in figure $4.5_{(4)}$. The dashed line, with associated constant error dotted line, is the *a priori* profile. The solid line is the retrieved profile, with associated error dotted profiles. Rodgers (2000) shows that the *total* error covariance of the final retrieval is given by $\hat{S}$, equation 4.27, and that it is composed by two main sources, the *measurement* error, S_m, which represents the uncertainty in the retrieval introduced by the noise, and the *smoothing* error, S_s, which represents the uncertainty introduced by possible components of the state vector that the measurements cannot detect. The relative contribution of these errors for the case study we are considering is displayed in figure $4.5_{(5)}$. The *a priori* error variance, S_a is 5 K, the smoothing error, S_s, is the dotted line, the measurement error, S_m, is the dash-dot line and the total final

[6]The equivalent matrices for the *Venera 15* case study are shown in figure 4.6. We do not explicitly mention them to avoid being repeatedly pedantic.

error covariance, $\hat{S}$, is the solid line. For loosely constrained retrievals, the diagonal elements of the *a priori* covariance are set to the estimated error at each level (in this case study, 5 K) and the off-diagonal elements are set to zero. No correlation is thence assumed between atmospheric levels and the temperature solution at each level tends to be independent of all others. In a real atmosphere however, there is a correlation between different levels which can be modelled mathematically using equation 4.29, where H is known as the *correlation length*. The correlation length in this study is set to 10 km since the atmospheric temperature is not expected to exhibit great variability. Hence, the *a priori* error covariance for the temperature profile is calculated using equation 4.29.

$$S_{ij} = S_{ji} = \sqrt{S_{ii}S_{jj}}\ \exp(-\frac{|(z_i - z_j)|}{H}) \tag{4.29}$$

One should note here that for both the *PV OIR* and the *Venera 15* measurements the measurement covariance matrix, S_ϵ, is diagonal, with no correlation between adjoining spectral points.

A third possible error component, not shown in the above equations, is the *bias error* of the retrieval method. This is the error that might result if the retrieval method chosen was not well-behaved and hence did not meet the criteria required by the particular problem. In short, if the only knowledge of the atmospheric state is the *a priori* state then virtual measurements can be calculated with the forward model using the *a priori* state as input. Thence, a good inverse method should return the *a priori* as retrieved state, if the measurement covariance matrix is the unit matrix signifying total confidence in the measurements. This test was performed for both

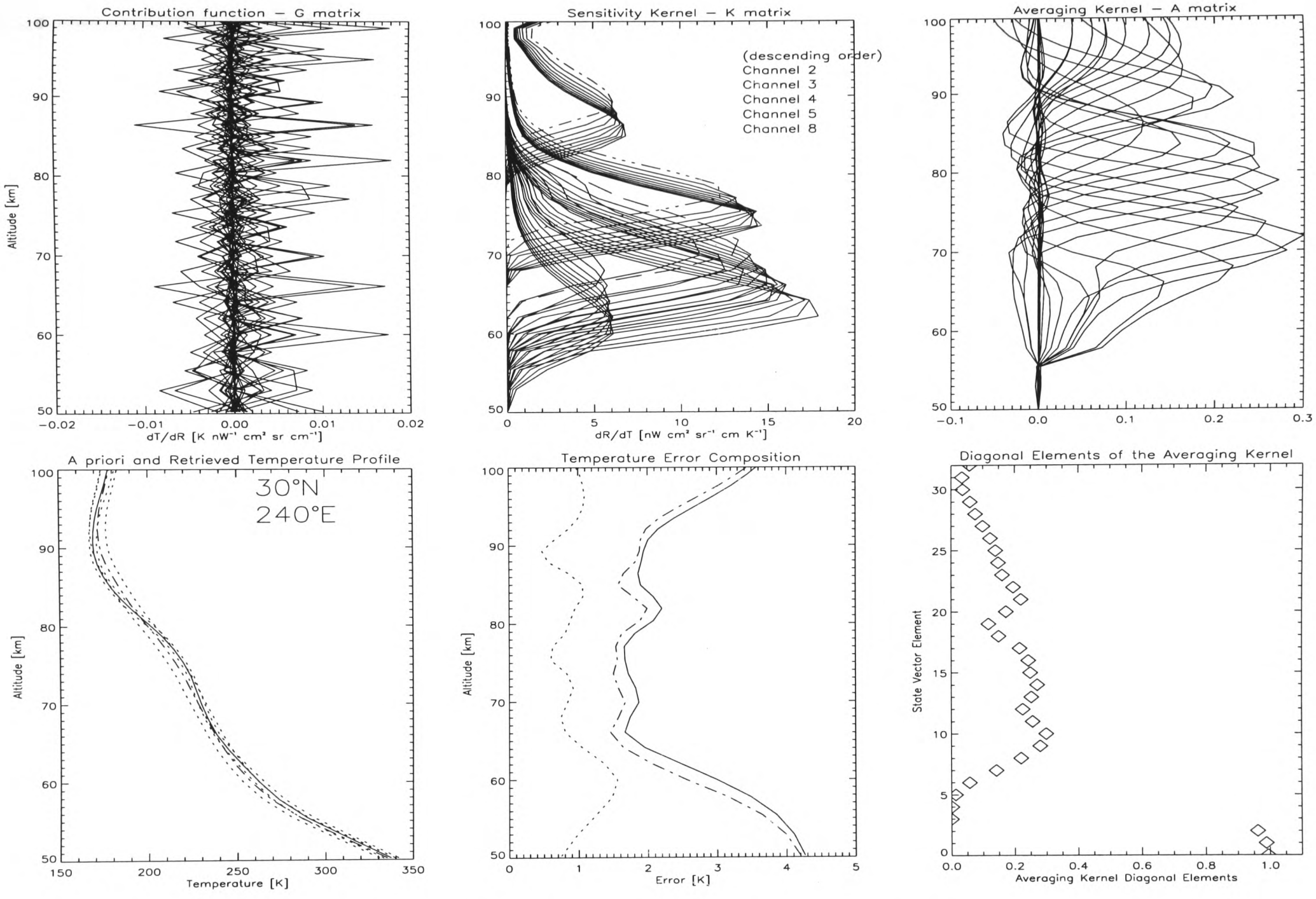

Figure 4.5: Retrieval diagnostics and example for the *PV OIR* case study measurement. The top row, left to right: contribution functions, sensitivity functions and averaging kernels for the temperature elements of the state vector versus altitude [km]. The bottom row, left to right: temperature *a priori* and retrieved profile with associated error, temperature error composition and diagonal elements of the $\mathcal{A}$-matrix for the whole state vector being retrieved.

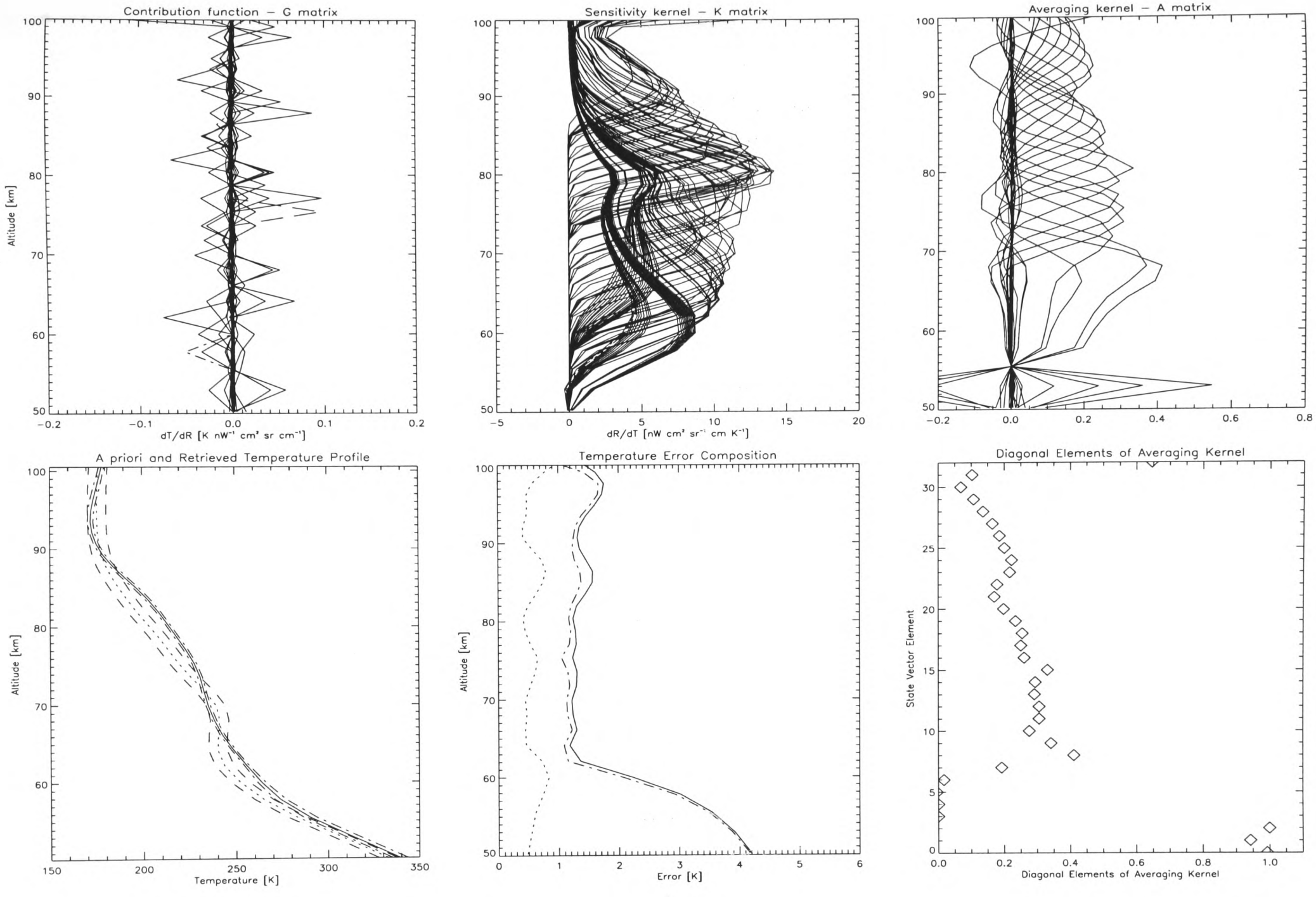

Figure 4.6: Retrieval diagnostics and example for the on-board *Venera 15* case study. The top row, left to right: contribution functions, sensitivity functions and averaging kernels for the temperature elements of the state vector versus altitude [km]. The bottom row, left to right: temperature *a priori* and retrieved profile with associated error, temperature error composition and diagonal elements of the $\mathcal{A}$-matrix for the whole state vector being retrieved.

sets of observations and the bias error was verified to be zero. This investigation also verifies the retrieval method, since a synthetic spectrum was created using known atmospheric parameters as input and the retrieval returned those same atmospheric parameters.

A fourth possible source of error arises from the incomplete knowledge of the physical system the forward model is trying to describe. Known as *forward modelling errors*, they represent neglected physics that should have been included in the forward model or incorrect input atmospheric parameters to the forward model who are *not* in the state vector, hence are not being retrieved and do not have an associated error. These errors may introduce an easily identified biased difference between the forward modelled spectra and the measured spectra. Hence, a known forward model bias could be treated as a simple vector added to the measurement vector y. There are a few possible sources of forward model error in this work, namely the spectroscopy and the atmospheric input parameters. For the case of spectroscopy, in view of the low resolution of both instruments, problems commonly found in other spectrometer studies, for example differences between line databases or high temperature corrections to the absorption coefficients, do not affect this analysis. One issue that was all the same investigated was the choice of line-wing cut-off in the calculation of the k-tables. Pollack et al. (1993) used a cut-off distance of 120 cm^{-1} for CO_2 and 25 cm^{-1} for all other molecules. Meadows and Crisp (1996) found that these choices seriously underestimated the far-wing absorption at high pressures. Even though we are not sensitive to regions of high pressure in this work,

k-tables were also created with an extreme cut-off at 1000 cm^{-1}. The predicted radiation was almost indistinguishable from the one calculated using the nominal k-tables with 35 cm^{-1} line wing cut-off and well within measurement error. For the case of the atmospheric input parameters, possible forward model error sources are the pressure, CO_2, CO, and SO_2 profiles. These were perturbed in both directions by 10% of their nominal value, except the CO_2 profile which was perturbed by 0.8% and the results are shown in figure 4.7. In this figure, the covariance of the forward modelling error matrix is compared to the total retrieved error covariance for the temperature elements of the state vector. As expected, the qualitative effects of perturbing the pressure and CO_2 profiles are the same, since the Venus atmosphere is well-mixed in CO_2. The highest effect, that of perturbing the pressure, is of the order of 0.7 K, below the total retrieved error in temperature at that level of ~1.8 K. The, however minimal, possible effects of CO and SO_2 are also constrained only in the lower part of the atmosphere.

4.4.3 Diagnostic Tools

The importance of the $\mathcal{K}$-matrix, $\mathcal{G}$-matrix and the $\mathcal{A}$-matrix has been discussed previously. In order to be able to quantitatively judge the accuracy and ability of the measurements to divulge the information on demand, two further diagnostic tools have been utilised, the *degrees of freedom* and the *information content.*

The degrees of freedom, after Rodgers (2000), depict the amount of quantities that can independently be retrieved from the specific measurements, *a priori* in-

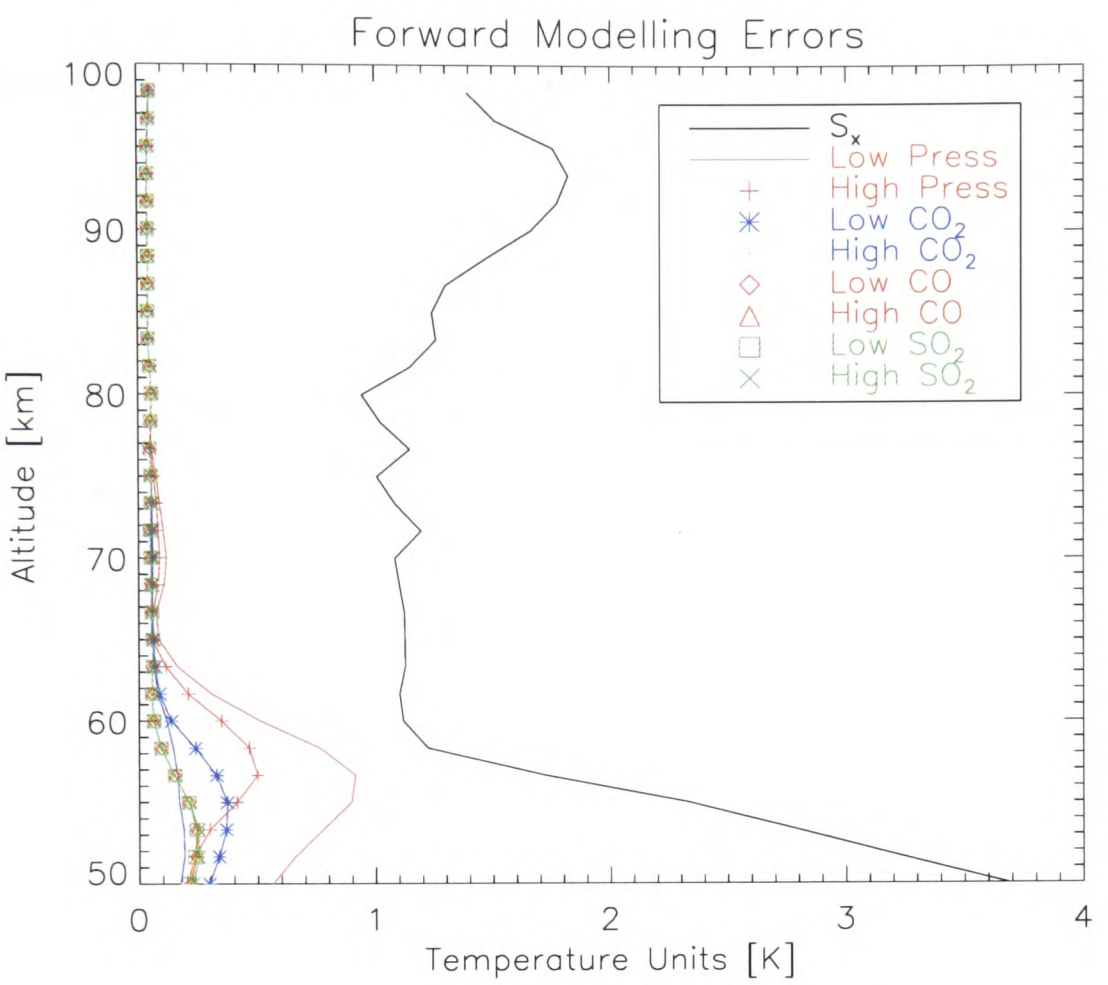

Figure 4.7: Investigation into possible forward modelling errors in the *Venera 15* measurements. The x-axis is in temperature units [K] and the y-axis represents the altitude range from 50 to 100 km. The total final retrieved temperature error is compared to the postulated error created by the various perturbances. The effect of the perturbations is confined to the lowest 20 km of the atmosphere considered and is lower than the total final temperature error. Above 90 km there exists very little information in the *Venera 15* measurements hence the increase in the total final retrieved error.

formation and forward model, and are given by:

$$d_s = \mathrm{tr}(\mathrm{I_n} - \hat{\mathrm{S}}\,\mathrm{S_a^{-1}}) = \mathrm{tr}(\mathrm{A}) \tag{4.30}$$

The largest number of degrees of freedom depends on the number of elements of the *state vector*, the *a priori* error covariance, the measurement error and the $\mathcal{K}$-matrix. Formally, this number was calculated as the rank of the $\mathcal{K}$-matrix, but due to the presence of random noise and the possibility of dependence between the rows of the $\mathcal{K}$-matrix, the actual number of independent variables will be less than

that.

Since the degrees of freedom can be calculated from the trace of the $\mathcal{A}$-matrix, the behaviour of the averaging kernel is a great indicator on the total number and distribution of degrees of freedom. If $\mathcal{A}$ were a perfect unit matrix all parameters of the state vector would have been independently retrieved. From figure $4.5_{(6)}$ we can see that for the first three retrieved parameters, namely, cloud-top height, fractional scale height and water vapour abundance, the diagonal elements of the averaging kernel are very close to unity (similarly in figure $4.6_{(6)}$.) For the temperature elements, it may seem that there is not enough information to retrieve a full-length 30-element temperature profile. However, the profile is constrained by physics to be continuous and so we would not require 30 degrees of freedom in order to accurately retrieve it.

The information content, expressed in "bits", represents the improvement on the *a priori* error after the retrieval and is given by:

$$\mathcal{H} = -\frac{1}{2}\log_2 |\hat{S}\, S_a^{-1}| = -\frac{1}{2}\log_2 |I_n - A| \tag{4.31}$$

It can also be seen as predicting the pieces of information gained by performing the retrieval as compared to the *a priori* information and is calculated from the determinant of the total retrieved error covariance matrix over the determinant of the *a priori* covariance matrix.

These two diagnostic tools complement each other in helping our understanding of the quality and potential of the measurements. The degrees of freedom should be viewed as the pieces of information that can be independetly retrieved from the entire

measurement spectrum, and this calculation does not depend on the precise nature of the retrievable quantities. The information content applies to each spectral point and depends on the choice of retrieved quantities. Using the two cloud parameters as an example, the algorithm will attempt to secure two degrees of freedom in order to perform the retrieval with the minimum amount of spectral points and hence reduce computational time and unnecessary retrieval noise. Once the spectral regions that contain this information are identified, the rest of the spectrum is discarded. This does not mean that there is no information in the rest of the spectrum, only that the best necessary spectral points were found in order to perform the retrieval.

Applying these diagnostic tools to both sets of measurements has hence proven an invaluable tool in asserting a number of choices made in this analysis of the *PV OIR* and *Venera 15* data sets. It is necessary to remind the reader here of some numerical facts about the two sets of measurements, presented in previous chapters; the *PV OIR* instrument is a radiometer and provides us with single radiance measurements, in groups of five values for the five radiometer channels. Depending on how many measurements with different viewing angles result in a single latitude/longitude bin, the *PV OIR* data will have $m = 5$ up to $m = 45$ number of measurements in steps of five. In the bin used as case study, the measurements cover nine different viewing angles resulting in $m = 45$, i.e. 45 semi-independent measurements. The *Venera 15* instrument is a spectrometer and provides us with full-length spectra, approximately from 250 to 1650 cm^{-1}. As a result of this difference between the two instruments, a different diagnostic discussion is required for each one. This diagnostic analysis is

$y(m)$	d_s [49 levels]	$\mathcal{H}$ [49 levels]	Lat/Lon
5	3.74 [3.85]	9.92 [10.00]	10°S, 330°E
10	4.30 [4.38]	12.22 [12.34]	0°S, 330°E
15	4.65 [4.70]	13.70 [13.80]	10°S, 350°E
20	5.05 [5.02]	15.29 [15.38]	10°N, 350°E
25	5.31 [5.26]	16.42 [16.50]	20°N, 350°E
30	5.54 [5.50]	17.21 [17.30]	30°N, 350°E
35	5.76 [5.84]	17.33 [17.75]	50°N, 350°E
40	5.87 [5.96]	17.85 [18.29]	50°N, 340°E
45	6.41 [6.52]	20.08 [20.19]	20°N, 260°E

Table 4.1: Information content and degrees of freedom for different amount of measurements in the *PV OIR* data set. The equivalent values for a state vector with 49 temperature elements is shown in the parentheses in order to relate to the work of Schofield and Taylor (1982).

discussed threefold in the following section; for the *PV OIR* radiance data set, the on-board *Venera 15* spectra and the on-Earth *Venera 15* spectra.

For the case of the *PV OIR* data; as has been shown in figure 3.2 not all latitude/longitude bins contain the same amount of measurements. The question thence arises whether it is possible to retrieve $n = 33$ state vector elements from the less populated bins. In table 4.1, the different number of measurements and their corresponding degrees of freedom and information content are presented. The semi-independent nature of the *PV OIR* data, firstly postulated in Schofield and Taylor (1982), is clearly demonstrated, as d_s does not rise further than $d_s \cong 6.41$ even for the case of nine difference viewing angles. Also shown are calculations made for a 49-element temperature profile used in the work of Schofield and Taylor (1982). It is evident that reducing the number of points of the temperature profile has not reduced the amount of available information to be extracted from the measurements.

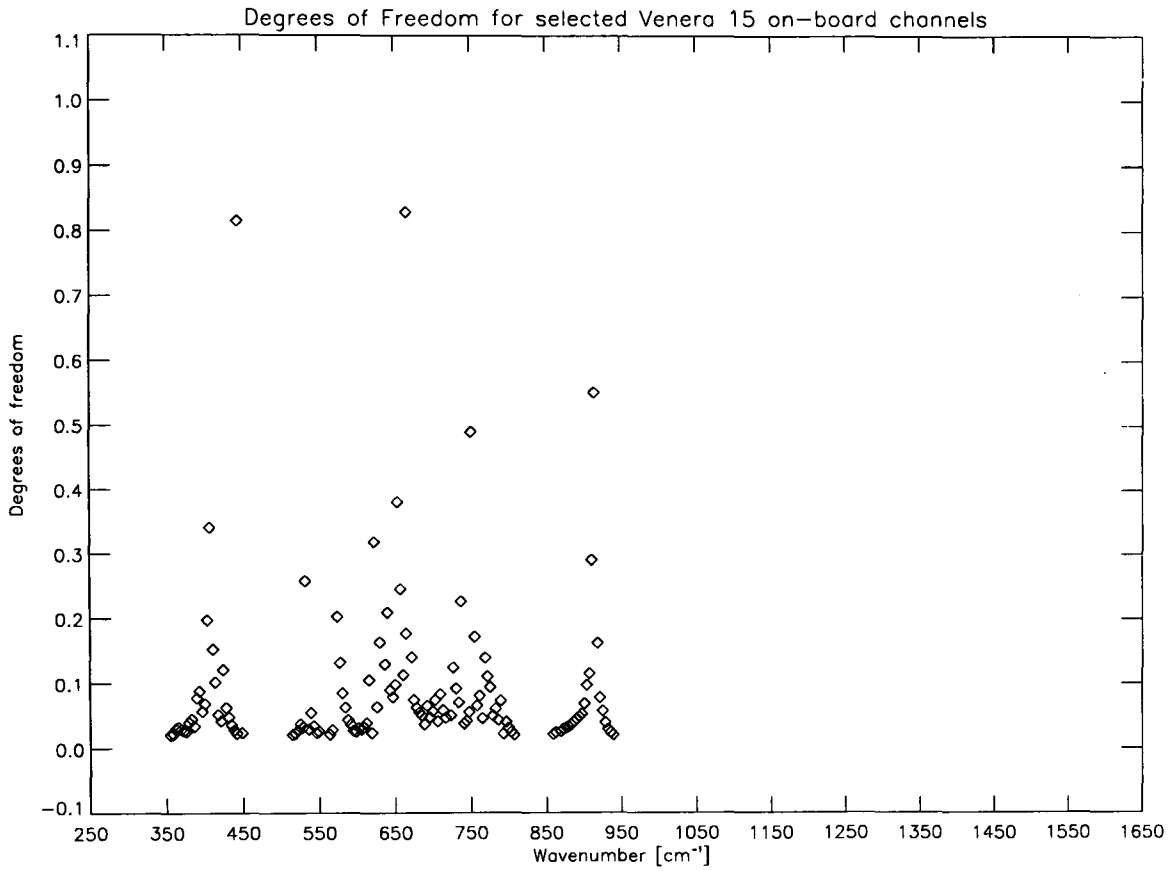

Figure 4.8: Degrees of freedom for the chosen 132 spectral points of a random on-board *Venera 15* spectrum vs wavenumber [cm^{-1}]. Most of the available information is contained in the first half of the spectrum.

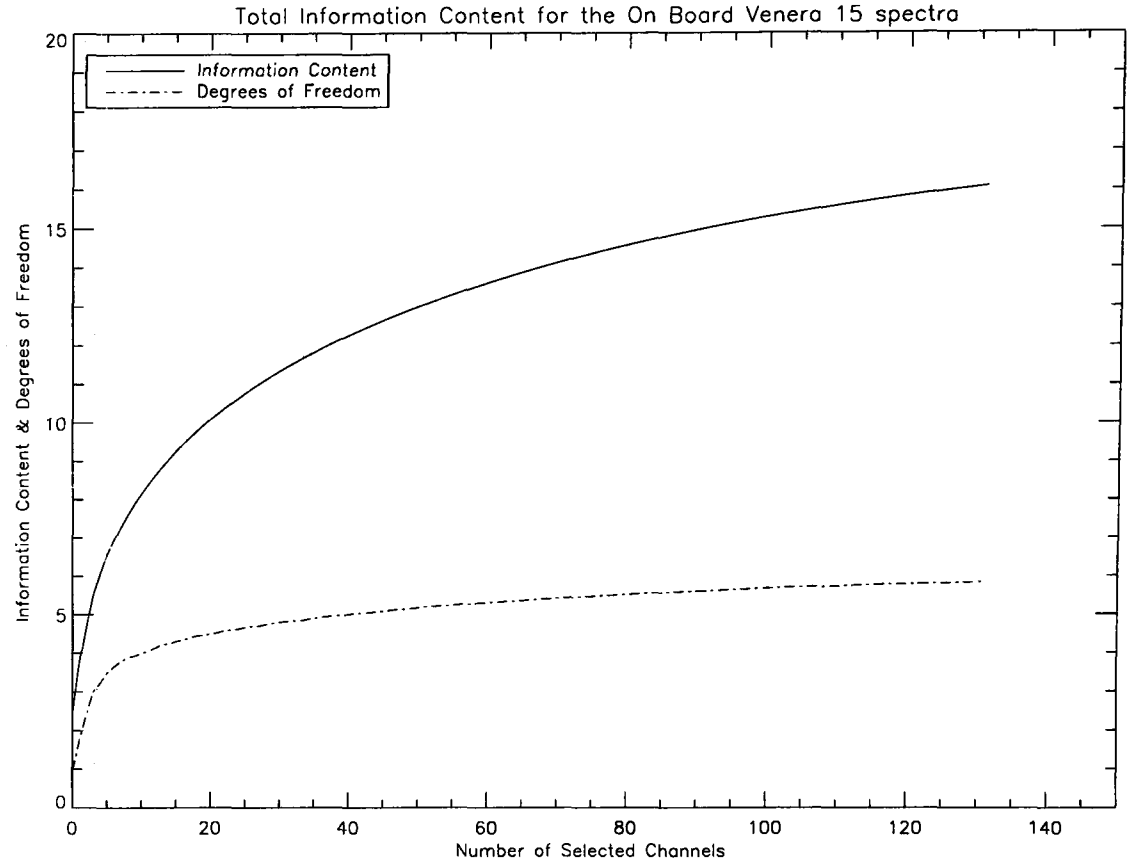

Figure 4.9: Information content and degrees of freedom of a random on-board *Venera 15* spectrum. The x-axis depicts the number of spectral channels chosen.

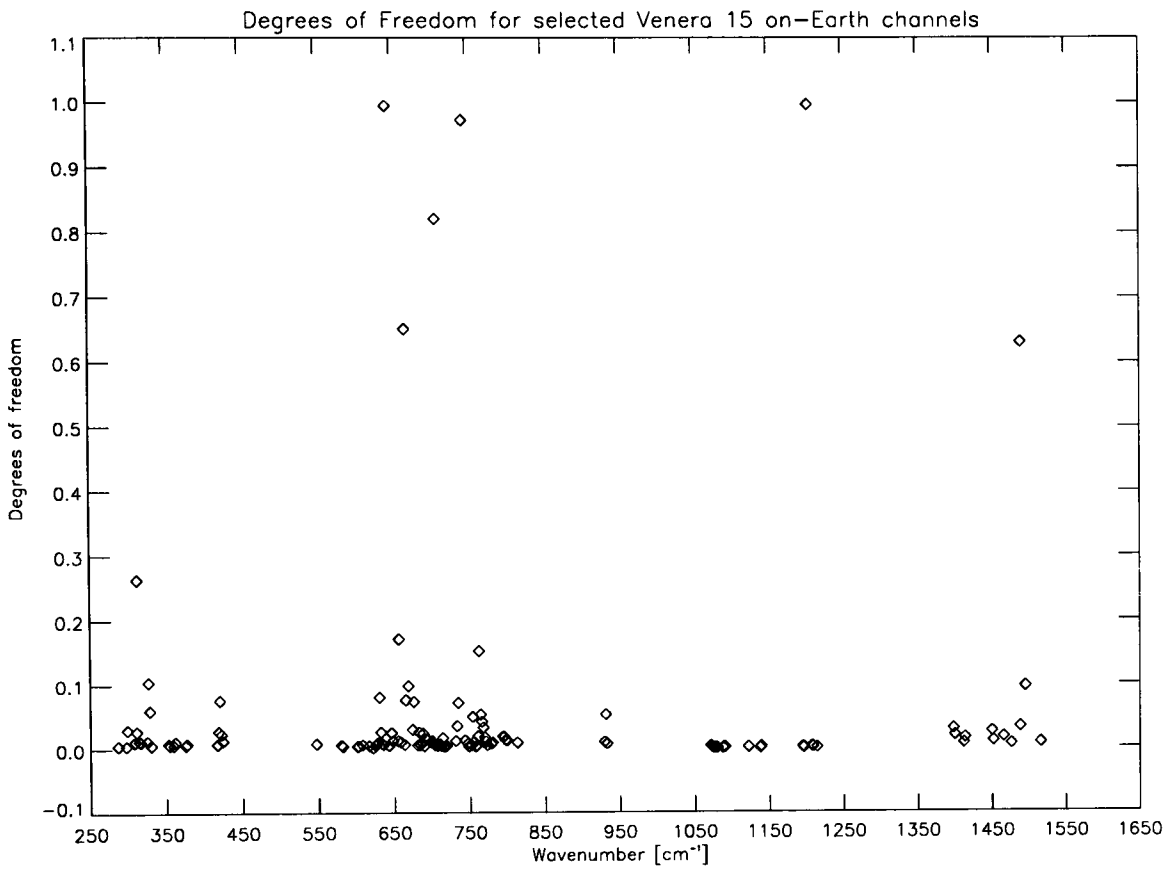

Figure 4.10: Degrees of freedom for the chosen 132 spectral points of a random on-Earth *Venera 15* spectrum vs wavenumber [cm^{-1}].

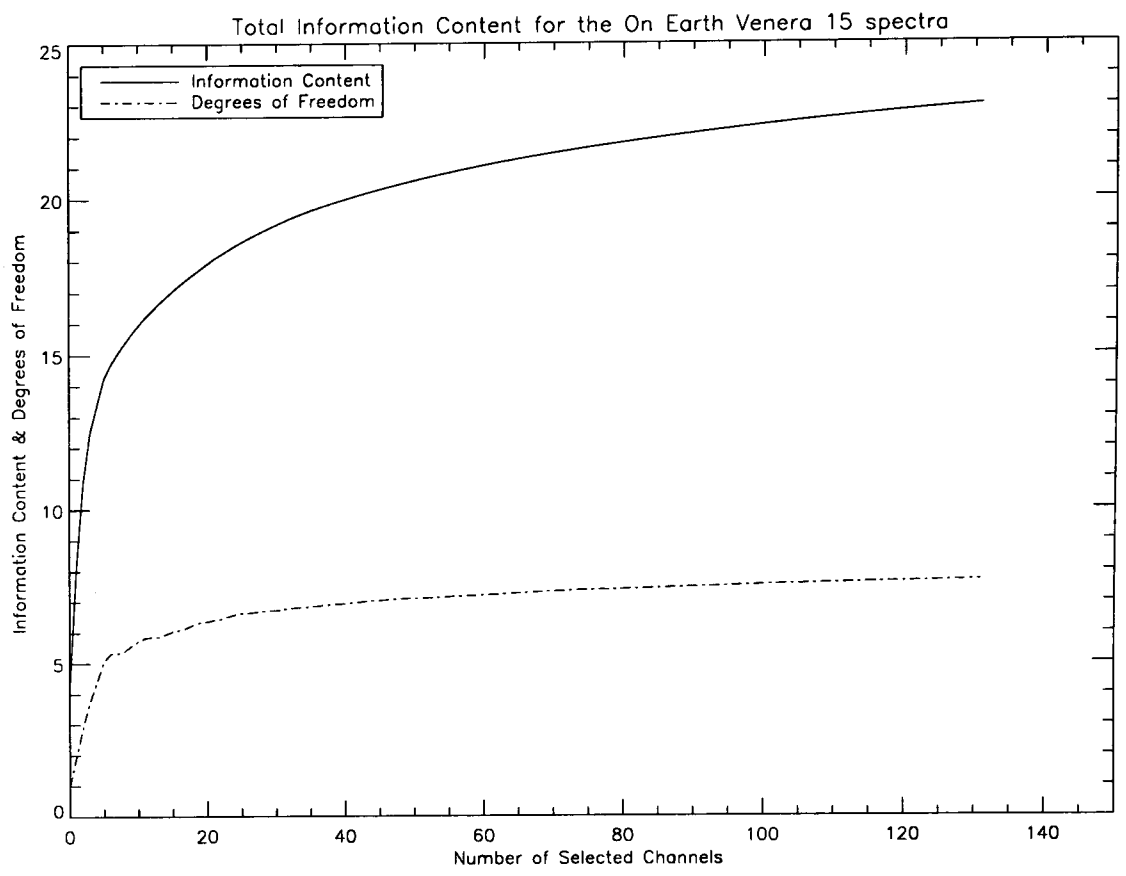

Figure 4.11: Information content and degrees of freedom of a random on-board *Venera 15* spectrum. The x-axis holds the number of spectral channels chosen.

For the case of the on-board *Venera 15* spectra; they extend from 275 to 1650 cm^{-1} and since the highest wavenumber that the *PV OIR* instrument measured is 896.5 cm^{-1}, one might safely assume that it is reasonable to only use the overlapping range of the *Venera 15* data set. In this case, the amount of spectral data points to be fitted would be reduced from $m = 399$ to $m = 181$, making the calculation computationally more affordable. However, in order to scientifically support this choice, the diagnostic tests were implemented. These show that most of the information about the state vector can indeed be found in the 275 to 950 cm^{-1} region, as shown in figure 4.8 which depicts the degrees of freedom of the chosen spectral points. Basically, each spectral point may, or may not, contain information about the retrievable species. The diagnostic tools checks each spectral point individually and estimates the information content and degrees of freedom that it contains. In the ideal case, since we are trying to retrieve $n = 33$ quantities we would like to pick spectral points whose total degrees of freedom add up to, or are close to 33. However, the inverse problem in radiative transfer theory is not ideal and the degrees of freedom in this randomly chosen on-board *Venera 15* spectrum does not exceed $d_s \cong 6$, whereas the information content is $\mathcal{H} \cong 18$ (figure 4.9). The number of final chosen spectral points was $m = 132$ for the on-board *Venera 15* measurements.

For the case of the on-Earth *Venera 15* spectra; they extend from 250 to 1650 cm^{-1} but with a higher resolution than the on-board spectra and better signal-to-noise ratio in the region of the rotational-vibrational water vapour band centred around 1500 cm^{-1}. Hence the total number of freedom in this case is slightly

increased to $d_s \cong 9$ and the information content to $\mathcal{H} \cong 28$ (figure 4.11.) As can be seen from figure 4.10, information about the cloud and water vapour is also contained in the second half of the original spectrum, around 1150 and 1450 cm^{-1} respectively. For continuity reasons, the number of spectral points of the on-Earth *Venera 15* measurements was also reduced to $m = 132$.

In conclusion, this initial diagnostic examination was performed on the average on-board and on-Earth *Venera 15* spectra. The final selection of the $m = 132$ channels was performed individually for each one of the on-board and on-Earth spectra. The post-processed reduced *Venera 15* spectra were then analysed using the retrieval process described previously.

Example Temperature Retrieval

In order to put the last few pages into context with the aim of this thesis, an example temperature retrieval from both sets of measurements is shown in figures 4.12 and 4.13. The leftmost panels show the *a priori* profile and associated error, set to 5 K. The middle panels shown the retrieved profile and error, and the rightmost panels the difference between *a priori* and retrieved. In the case of the *PV OIR* profile, the best retrieved profile from the work of Schofield and Taylor (1982) is also shown as the red line for comparison purposes. The retrieved profile and error profiles revert to the *a priori* for the altitudes where there is no information in the measurements. This is the kind of diagnostic inspection on the results of a retrieval that can be made via the error analysis kernels, discussed in the previous section.

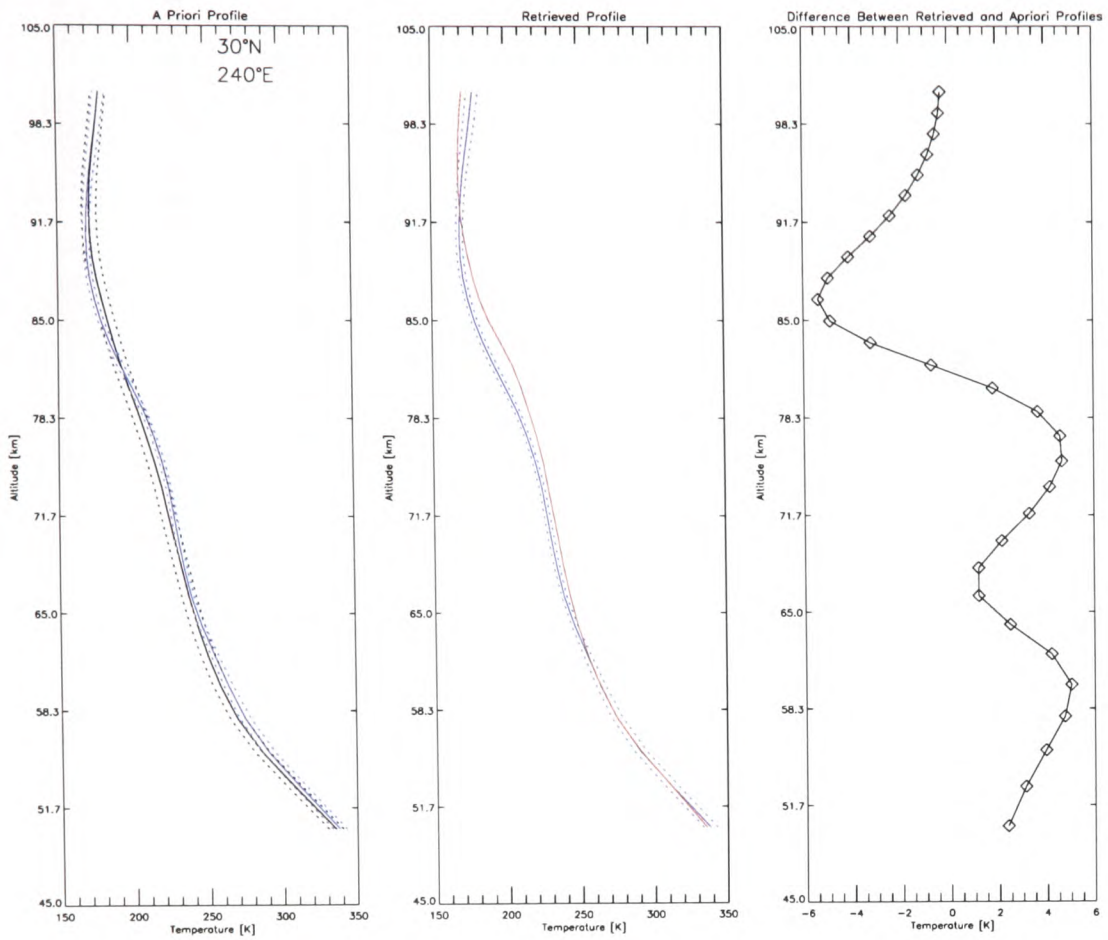

Figure 4.12: Example temperature retrieval from the *PV OIR* data. Left panel: the black line is the *a priori* temperature profile and the blue line is the retrieved profile. The dotted lines are the associated errors. Middle panel: the blue line is the retrieved profile and associated error. The red line is the retrieved profile from the work of Schofield and Taylor (1982). Right panel: the temperature difference between the *a priori* and the retrieved profile.

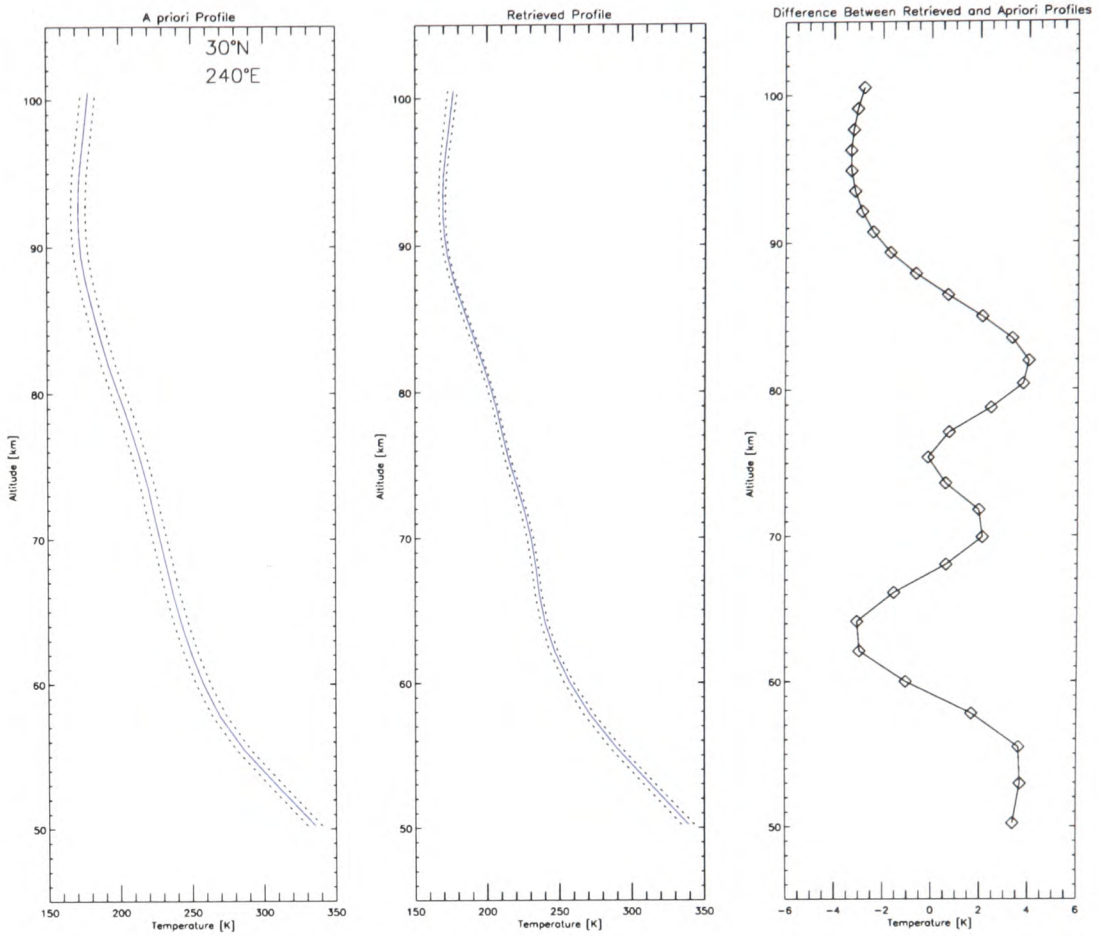

Figure 4.13: Example temperature retrieval from the *Venera 15* data. Left panel: the *a priori* temperature profile and associated error (dotted line). Middle panel: the blue line is the retrieved profile and associated error. Right panel: the temperature difference between the *a priori* and the retrieved profile.

4.4.4 Aerosol Correction Coefficient Retrieval

As demonstrated previously in section 4.2, the principal source of uncertainty in this analysis but also in Schofield et al. (1983) and Ignatiev et al. (1999) is the correct representation of the sulphuric acid cloud contribution to the observed radiation. The lack of adequately precise data for the optical properties of the H_2SO_4 cloud in the range 50 to 400 cm^{-1} led both aforementioned authors to resort to approximate methods to quantify the cloud absorption contribution. In this section, we first discuss the methods that Schofield et al. (1983) and Ignatiev et al. (1999) resorted to in order to compensate for the lack of optical data. Then we present the differences between the refractive index data sets that supply the optical depth properties of the cloud. We then discuss how we used the *Venera 15* spectra in order to extract the cloud correction coefficients used in this analysis. This extraction was not possible from the *PV OIR* measurements alone as they are single radiance points.

In Schofield and Taylor (1982) and Schofield et al. (1983), the spectral variation of the cloud extinction coefficient is represented by a single factor, $r54$, the ratio of extinction coefficients at the wavelengths defined by the central wavenumbers of channels 5 and 4. Similarly, $r58$, the ratio of channels 5 and 8, provides the cloud extinction coefficient applicable to the water channel. The $r54$ ratio was set to 1.7, from Mie theory calculations for 1.05 μm radius H_2SO_4 droplets and the $r58$ ratio was set to 2.78, based on the calculations of Aumann and Orton (1979). The refractive index data they used was that of Palmer and Williams (1975) and Jones (1976), shown in figure 4.14. To test the sensitivity of the retrieved water vapour

abundance to these two ratios, Schofield et al. (1983) retrieved the *PV OIR* data using two extreme cloud models, with a 20% difference in the opacity ratio $r54$. Changes in absolute water vapour abundance of the order of $\pm 30\%$ were observed even though the relative features (day-night variation, wet spot) remained unaltered.

In Ignatiev et al. (1999), the authors resorted to introducing a small *ad hoc* correction factor to the cloud absorption coefficient, as a smooth function of wavenumber in the range of 0.75 to 1.8 (-25% to +80%) over the spectral interval of $250 < \nu < 400\,\mathrm{cm}^{-1}$. Although the authors have kindly provided us with these correction coefficients, we have opted to retrieve them anew in this work for continuity reasons.

In the forward model used in this study, we did not need to resort to optical depth ratios as Schofield and Taylor (1982) did, but rather use the existing knowledge of the cloud absorption coefficient over the entire wavenumber range covered. However, the use of the Jones (1976) data prevent the accurate representation of the cloud β_p^{abs} in the 228.0 cm^{-1} water band since the author quotes a 10% error on the experimentally acquired imaginary refractive index, m_i. The imaginary part of the refractive index is directly proportional to the absorption coefficient, β^{abs} through:

$$m_i = \beta^{abs} \frac{\lambda}{4\pi} \tag{4.32}$$

where, λ here is the wavelength (Salby, 1996). The disagreement between refractive index data sets is evident in figure 4.14, where the overlap between the Jones (1976) and the Biermann et al. (2000) imaginary parts is far from satisfactory. Unfortunately, even though a number of new experimentally acquired refractive index data sets exist for H_2SO_4 aerosol solutions (Tisdale et al., 1998; Heathfield

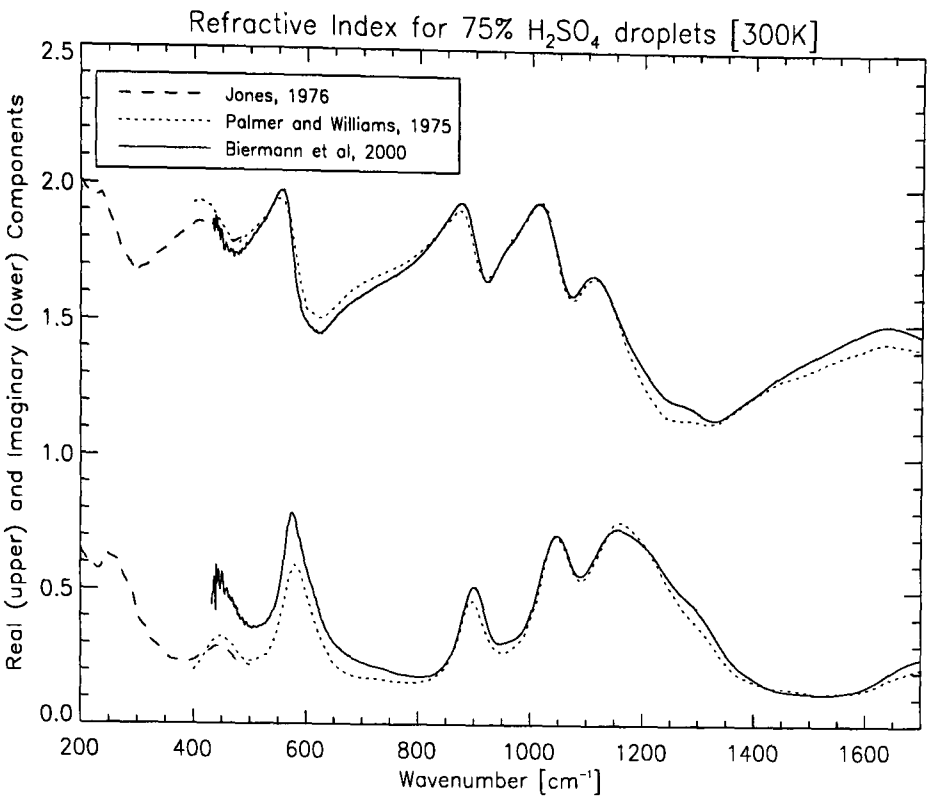

Figure 4.14: Biermann et al. (2000): solid lines, Jones (1976): dashed lines, Palmer and Williams (1975): dotted lines. The upper curves are the real part and the lower curves the imaginary part of the refractive index.

et al., 1999; Niedziela et al., 1999), none of them extends further than 400 cm^{-1}. The Mie calculation was performed for the cloud specifications discussed in section 4.2.2 for the refractive index data of Jones (1976), Palmer and Williams (1975) and Biermann et al. (2000). The normalised resulting cross-section is shown in figure 4.15.

Without entering further into the details of the Mie scattering theory, one should note that in order for the calculations shown in figure 4.15 to be performed a number of parameters had to be specified; the mean size, variance and distribution of the aerosol particles, the sulphuric acid percentage concentration of the droplets and their expected effective temperature. The cloud used in this analysis, and discussed extensively above, is uni-modal; however Pollack et al. (1980), who describe the

Venus cloud properties from the P V Sounder probe location, have presented a multi-modal cloud aerosol model. Four different mean sizes, variances and aerosol number densities describe this multi-modal cloud and as demonstrated in Figure 1 of Zasova et al. (1999), different cloud extinction curves result from the Mie scattering calculation on the characteristics of the four different modes. Unfortunately, as shown in section 4.4.3, not enough information is contained in either the *PV OIR* or the *Venera 15* datasets to warrant trying to retrieve cloud parameters for different aerosol modes. In order to achieve such a task, one would require dedicated radiative channels for each of the different cloud modes. Hence, our efforts were focused on retrieving the optical depth of a uni-modal cloud through the two physical parameters that define its number density; the unit optical depth (cloud-top pressure) and the fractional scale height. In the following, we are discussing the retrieval of the correction factor on the cloud extinction coefficent using the *Venera 15* spectra. This correction was then applied to the cloud extinction coefficient curves used in solving equation 4.15 for both the *PV OIR* and *Venera 15* retrievals.

The correction factor retrieval was performed as a separate step, before attempting to retrieve temperature, cloud and water vapour abundance. Both the on-board and on-Earth *Venera 15* data were averaged within the 10° latitude/longitude bins in order to smooth out the data variability and measurement noise. Hence, a correction factor curve was extracted for each of the *Venera 15* latitude/longitude bin. The wavenumber range targeted spanned between 270 and 430 cm^{-1}. An iterative retrieval algorithm was set up in order to retrieve the correction factor

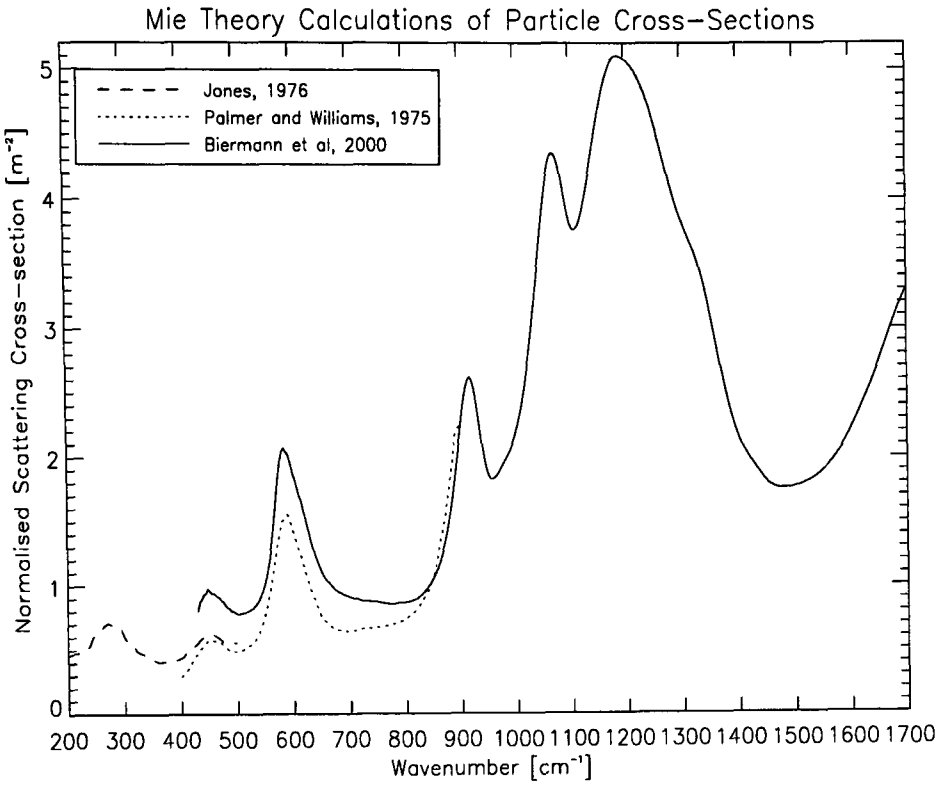

Figure 4.15: Mie theory calculations of single scattering cross-sections using the three different refractive index data bases shown in figure 4.14. The cross-section has been normalised by a factor of 10^8.

at each wavenumber separately. The forward model used is the same as the one described in section 4.3, with the exception that the state vector now only contains one element (the correction factor) and the function minimised is given by $\phi = (y - y_n)^T \, S_\epsilon^{-1} \, (y - y_n)$. The same cost function type checks were performed as the ones visualised in figure 4.4. An example of the retrieved correction factors is shown in figure 4.16. The corrected cloud extinction cross-sections were then implemented for both the *Venera 15* and *PV OIR* retrieval analyses.

In conclusion, we have created a new set of correction coefficients to the cloud absorption cross-sections calculated using Mie theory from Jones (1976) refractive index data in order to properly analyse the *PV OIR* and *Venera 15* observations. These correction coefficients have been created via a one-dimensional retrieval of the

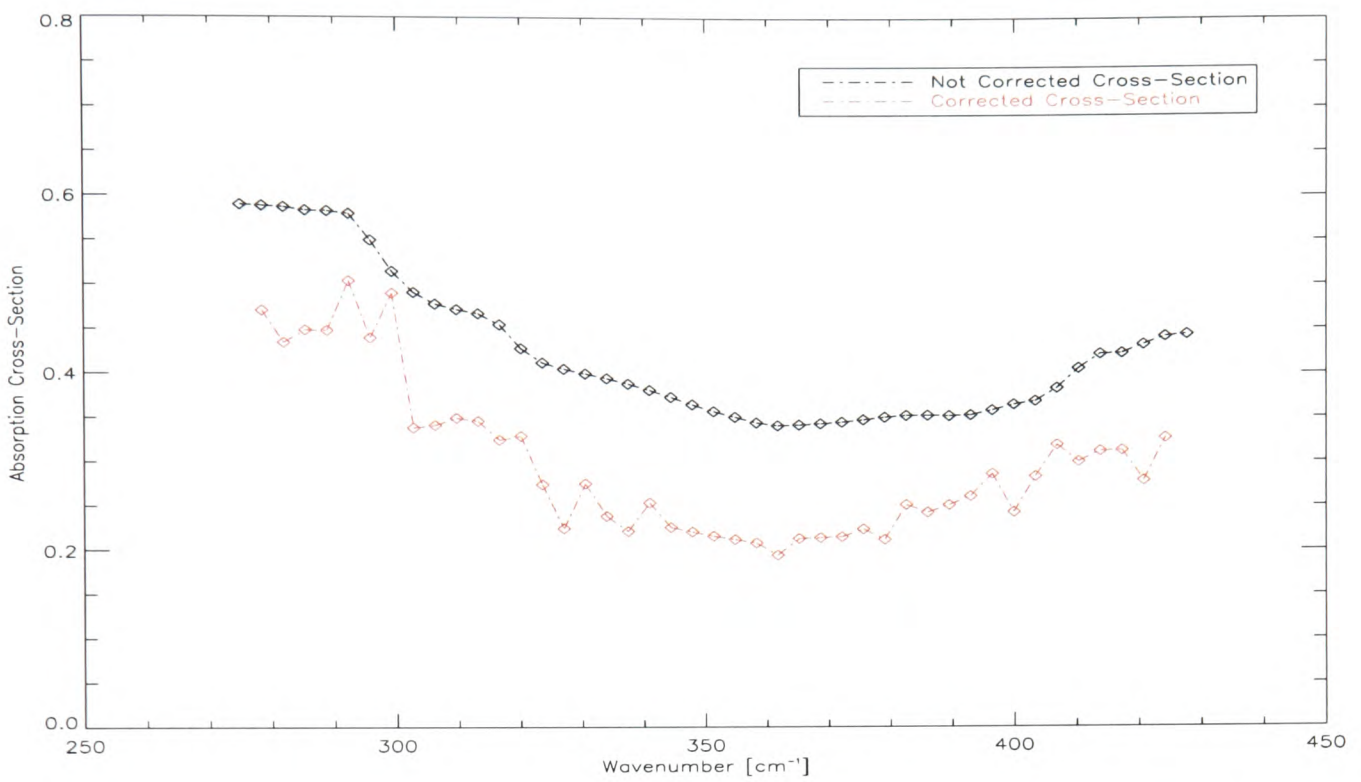

Figure 4.16: Original and corrected cloud extinction cross-sections. The original was calculated with the Jones (1976) refractive index data, for a solution of 75% H_2SO_4 at 300 K temperature. The cross-section has been normalised with a factor of 10^8.

Venera 15 spectra, and were created for all areas of latitude/longitude coverage of the *Venera 15* dataset. Nearest neighbour retrieved coefficients were used in order to service the *PV OIR* regions of coverage. These coefficients cannot however be considered as a "standard" corrective measure to be used by anyone needing to use the Jones (1976) refractive index database. They are by definition model-dependent since our forward model was used in order to attain them from the retrieval of the *Venera 15* spectra. On the other hand, it was impossible to retrieve these correction coefficients as part of the main cloud-top pressure, fractional scale height, water vapour and temperature retrieval procedure as they are 100% correlated with the two cloud parameters. Hence, this pre-retrieval analysis was paramount so as to correctly implement the joint retrieval on the *PV OIR* and *Venera 15* observations.

Systematic error on the *PV OIR* results

One of the main concerns in the work of Schofield et al. (1983) was the dependence of the retrieved water vapour abundance on the cloud extinction coefficients that describe the contribution of the cloud absorption to the radiance sensed by the *PV OIR* water channel. This concern is based on the quality of the refractive index data that describe the optical properties of the sulphuric acid droplets in the 50 to 400 cm^{-1} region and the authors performed tests to quantify this dependence. As discussed previously, they give an estimate of 30% change on the absolute water vapour abundance retrieved due to a 20% difference in the opacity ratios their radiative transfer model is based on. This same concern led us to perform the elaborate cloud extinction coefficient correction factor retrieval benefiting from the quality of the *Venera 15* spectra, as described above. However, it would be unreasonable to assume that this corrective measure has eradicated all systematic errors on the retrieved water vapour from the *PV OIR* dataset.

As such, an investigation on the systematic error on the water vapour abundance retrieved introduced by altering the cloud extinction coefficient curve was performed. Based on the error assessment of Jones (1976) on the imaginary part of the refractive index of the aerosol droplets being about 10%, the cloud extinction curve (figure 4.15) was perturbed upwards and downwards by 10% between 50 and 400 cm^{-1}. The absolute difference in water vapour abundance between the two perturbed retrievals and the nominal one was uniform throughout the *PV OIR* global coverage and of the order of *4 to 8 ppm*. Further to this, no significant

change in the retrieved cloud parameters was observed, further testifying that the cloud information is mostly obtained by the dedicated *PV OIR* cloud channel. A extensive discussion on the possible correlation between cloud-top pressure and water vapour abundance retrieved is given in section 5.4.

4.5 Synopsis

The main aim of this chapter was to describe the basis of remote sensing theory and how the inverse methods of retrieving atmospheric temperature and constituent abundances are used in practise. Specifically, in section 4.1, the equation of radiative transfer for a nadir-viewing instrument that observes a planetary atmosphere is illustrated. This thermal emission, as observed in the spectral ranges covered by both instruments, arises mostly from carbon dioxide and water vapour spectral lines and from a continuum absorption from the sulphuric acid droplets that compose the Venus cloud. The atmospheric model developed for solving the radiative transfer equation is described in section 4.2, where the calculation of the transmittances due to gases (section 4.2.1) and due to the cloud (section 4.2.2) is explained. The possible sources of discrepancy between this work and the ones of Schofield et al. (1983) and Ignatiev et al. (1999) were also recounted at this stage. The forward model developed for this analysis is discussed in section 4.3. The retrieval scheme used to invert the radiative transfer equation is detailed in section 4.4.1 followed by the error analysis and characterisation for the results from both instruments (section 4.4.2)and a example temperature retrieval (section 4.4.3.) This section

ends with demonstrating the need for aerosol correction coefficients and the retrieval process developed and executed in order to create them for this work (section 4.4.4.)

In the following chapter the results of this analysis are presented and described and in chapter 6 a discussion on the possible physical explanations behind the retrieved results completes this thesis.

Chapter 5

Joint Retrievals: Results

In this chapter the results of the new analysis of the *PV OIR* and *Venera 15* observations are presented and discussed. The products of the two instruments are initially displayed separately in sections 5.1 and 5.2. In section 5.3 the results from the common areas of coverage of the planet are compared and contrasted. A discussion on the scientific validation of the results is presented in section 5.4. A summary of the key observed features is given in section 5.5. A comprehensive discussion on the physics behind these observations will be elaborated further in chapter 6.

5.1 *PV OIR* Results

The global temperature field for two altitudes at the cloud-top region is shown in figure 5.1 and the associated retrieval error in figure 5.2. The temperature structure was found to be more or less isothermal below the 50° parallel, with zonal

fluctuations between 5 and 10 K. The beginning of the temperature inversion known as the "polar collar", discussed in chapter 1, can be seen between 50° and 60°N. Temperature maxima were found just before local noon and midnight, giving the impression of a small scale semi-diurnal variation. These temperature signatures are present in the raw radiance data of the *PV OIR* temperature sounding channels. The *a priori* temperature field is shown in figure A.1 and has an associated *a priori* error of 5 K.

The retrieved cloud-top pressure (cp0) and fractional scale height for the cloud (hc) are shown in figure 5.3. In the upper panel, the cloud-top pressure was found to exhibit a minimum in the late evening equatorial region and a maximum in morning mid-latitudes. In altitude units, the difference between the minimum and maximum cloud-top pressure is of the order of 3-4 km, almost an atmospheric scale height. The maximum cloud-top pressure is highly correlated with the highest fractional scale heights retrieved which are shown in the lower panel. The fractional scale height is given by the cloud scale height over the atmospheric scale height. At these altitudes, the Venus atmosphere is well-mixed in CO_2 and the retrieved temperature field shows almost no variation. Hence, the observed change of up to 30% in fractional scale height may signify that the cloud composition itself changed, possibly due to dynamics. A similar provisional explanation is also given in Ignatiev et al. (1999), where the equilibrium concentration of the sulphuric acid aerosol particles is deduced to be 76-83% in the region of unit optical depth pressure of 62.5±2.5 km, and 67-82% in the region of cp0 of 56±2.0 km.

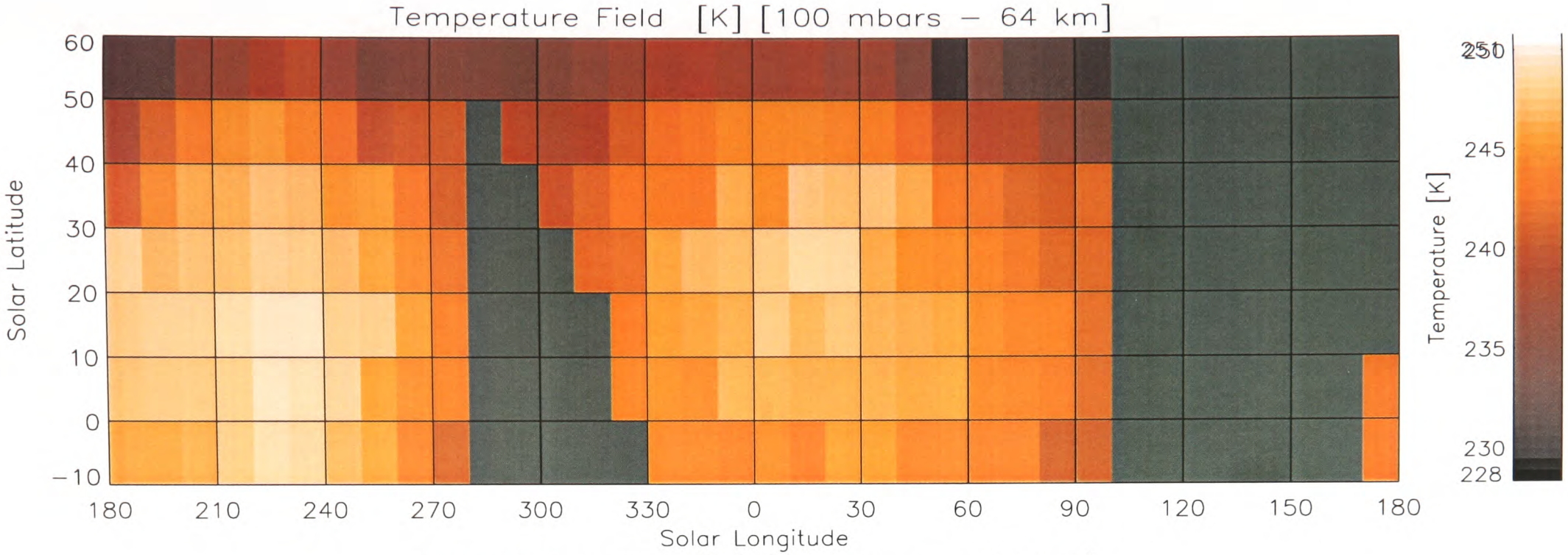

Figure 5.1: *PV OIR* temperature retrievals. Two global temperature fields at the cloud top region, at 100 and 75 mbars, are shown. The scale height at these altitudes is $\sim$ 5 km.

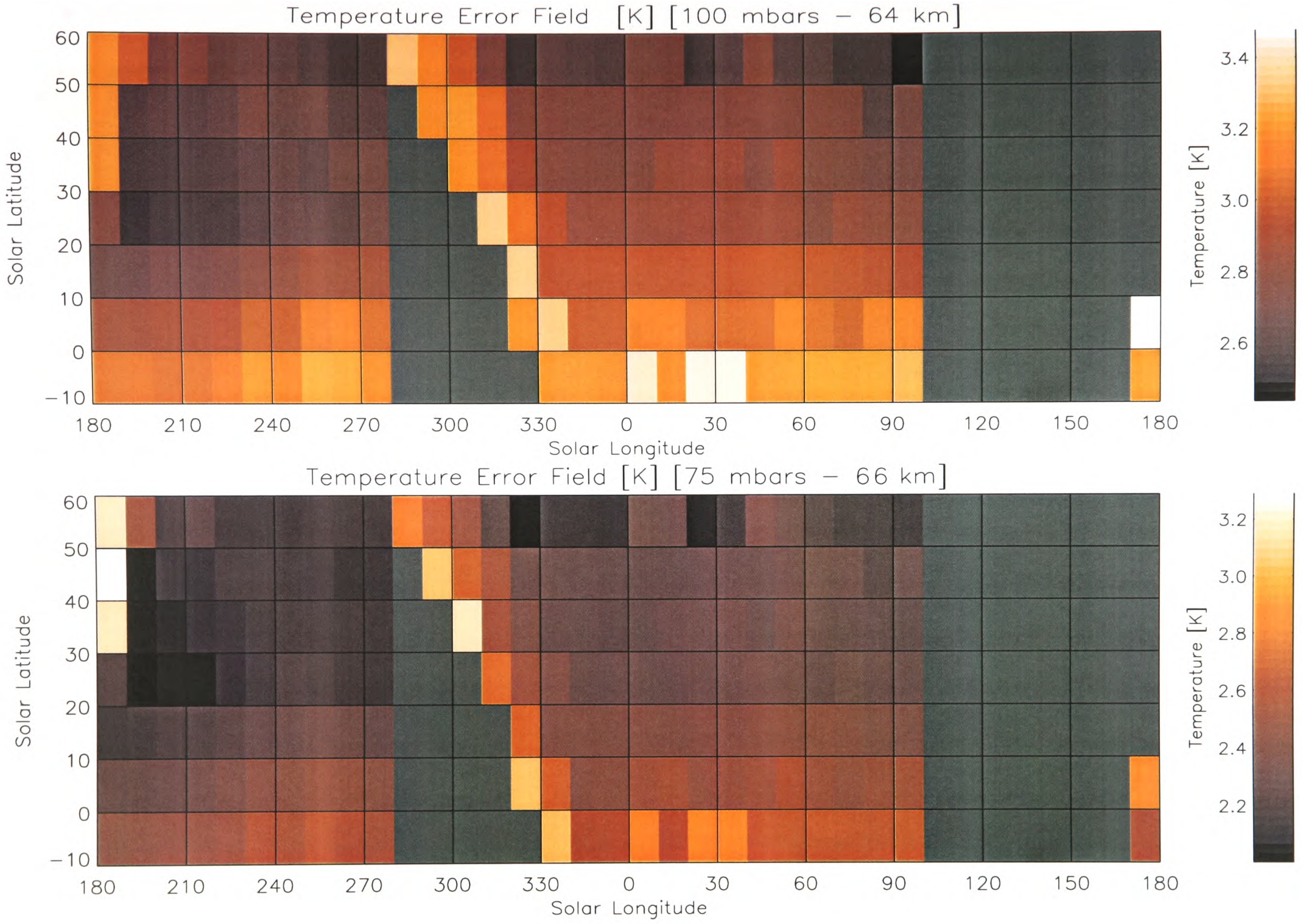

Figure 5.2: *PV OIR* temperature retrieval error for the global fields.

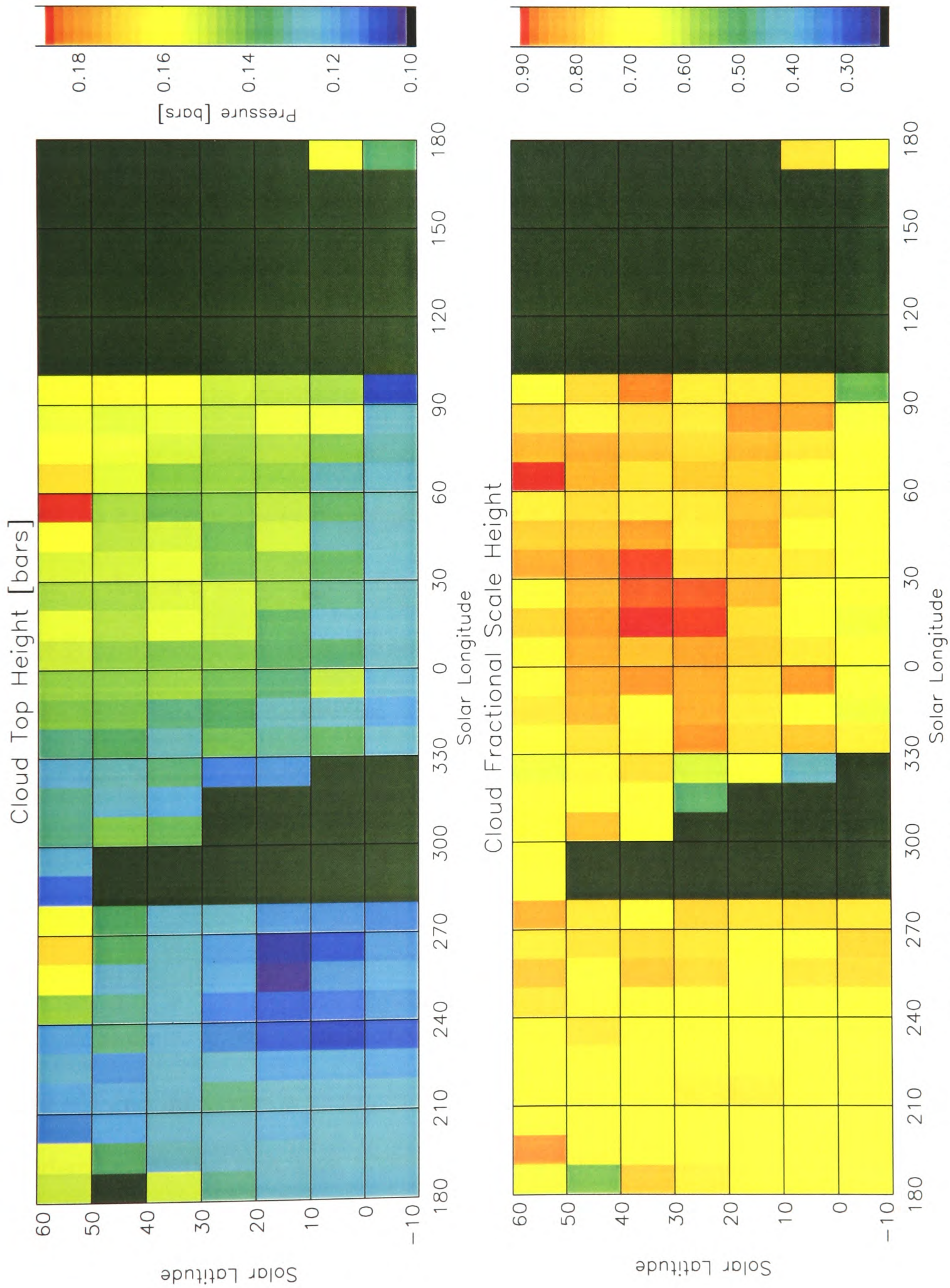

Figure 5.3: *PV OIR* cloud-top pressure and cloud fractional scale height retrievals.

The precise variation of unit optical depth (cloud-top) pressure with solar longitude and latitude is clearly demonstrated in figures 5.4 and 5.5 respectively. The error bars are not shown in figure 5.5 for clarity reasons. The morning and evening terminators (90° and 270°E) were used to divide the markers into day- and night-time observations. From figure 5.4 we can see that the cloud-top pressure at nighttime is ~110 mbars and the highest at daytime is ~140-150 mbars. In figure 5.5, at equatorial latitudes the mean cloud optical depth is unity at 125 mbars (~63 km) with a longitudinal dependence of ±25 mbars and the cloud scale height is about 0.75±0.15 times the atmospheric scale height.

The water vapour abundance map derived from the new analysis of the *PV OIR* radiance data is shown in the upper panel of figure 5.6 and the associated retrieval error in the lower panel. A number of features observed already by Schofield et al. (1983) have been enhanced in the new results due to the smaller binning system. The main water vapour enhancement, the "wet spot", has been recovered shortly after local noon in the equatorial region with a maximum of ~100 ppm (~50 pr micron), with the secondary maximum of ~40 ppm centred around 30°N, 0°E. From the lower panel of figure 5.6 we note that greater confidence is placed in this secondary maximum and in the nightside observations of the planet, i.e. in the regions of water vapour abundance less than 20 ppm. The water vapour abundance variation with latitude and longitude is shown in figures 5.7 and 5.8. The day-night variation is evident, as the fact that most nighttime measurements do fall within the 20-30 ppm region. In figure 5.8, the distinction between day and night retrieved abundances is

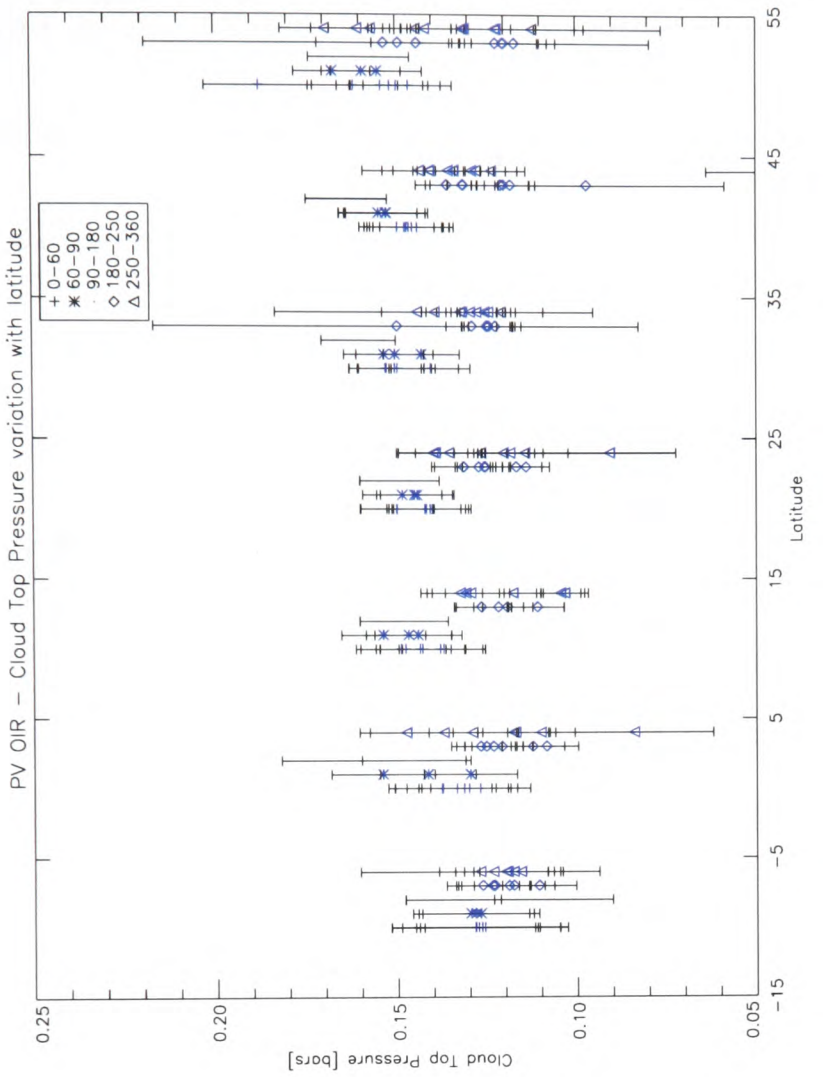

Figure 5.5: *PV OIR* cloud-top pressure variation with latitude. The data have been shifted in latitude for clarity purposes.

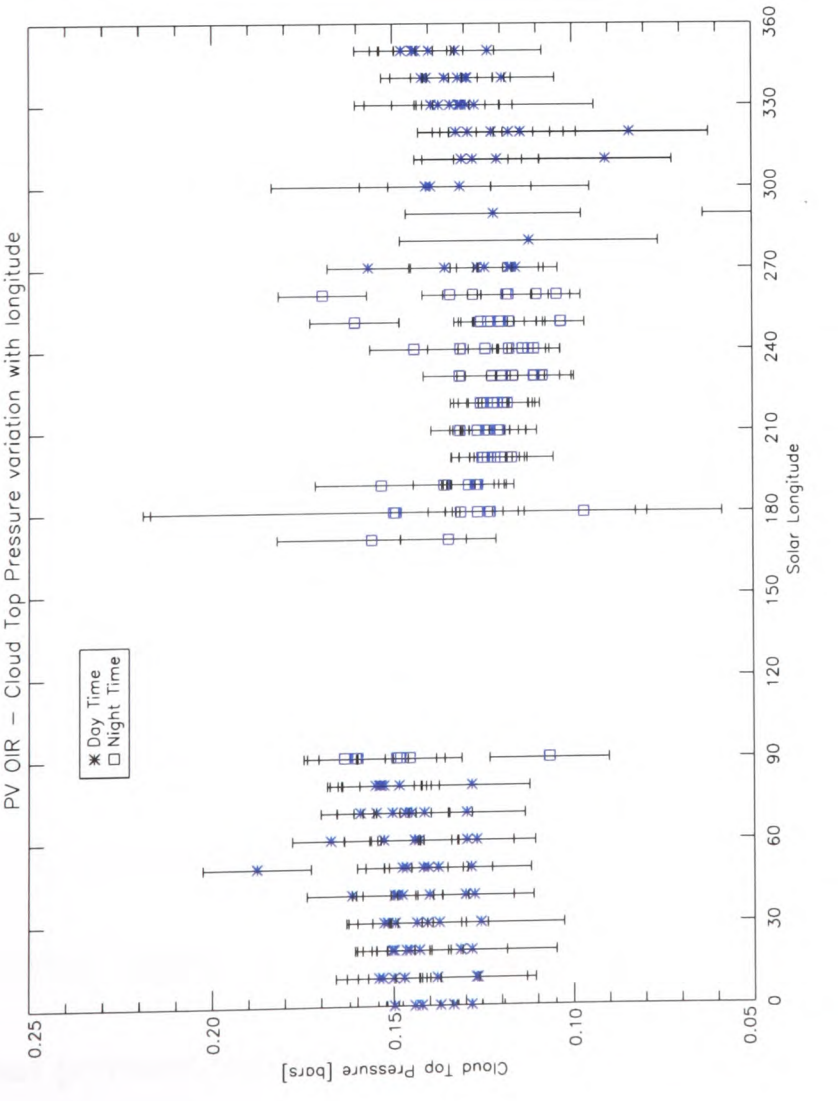

Figure 5.4: *PV OIR* cloud-top pressure variation with longitude and associated error bars. The retrieved values shown are the same as those of figure 5.3.

apparent in more or less all latitudes. With respect to the shape of the wet spot, on first inspection, it might not look unreasonable that the zonal wind is involved in creating its elliptical shape. In chapter 6 a detailed investigation into this issue is given.

5.2 *Venera 15* Results

As has already been discussed in section 3.2, figure 3.4, in each latitude/longitude bin more than one *Venera 15* spectra were found, from both on-board and on-Earth data sets. Each of these was analysed separately by the retrieval process and the individual results were then statistically averaged to produce the figures shown in this section.

The global temperature field for two altitudes near the cloud-tops is shown in figure 5.9 and the associated retrieval error in figure 5.10. Since the spatial coverage of the *Venera 15* spacecraft was not as complete as the coverage of the *PV OIR* measurements, it is harder to make comprehensive comments about the general state of the atmosphere. We can note that the atmosphere remained in its near-isothermal state, with the temperature inversion region poleward of the 50°N parallel becoming noticeable. The 280°E latitudinal strip, up to 20°N, contains the results from the special on-board spectra session where the Venera 15 satellite was rotated so that the *Venera 15* FTS instrument points in the near-nadir at equatorial latitudes. The associated viewing angle of these spectra is indeed close to nadir, testifying that the instrument was probing further down into the atmosphere. This is the reason why

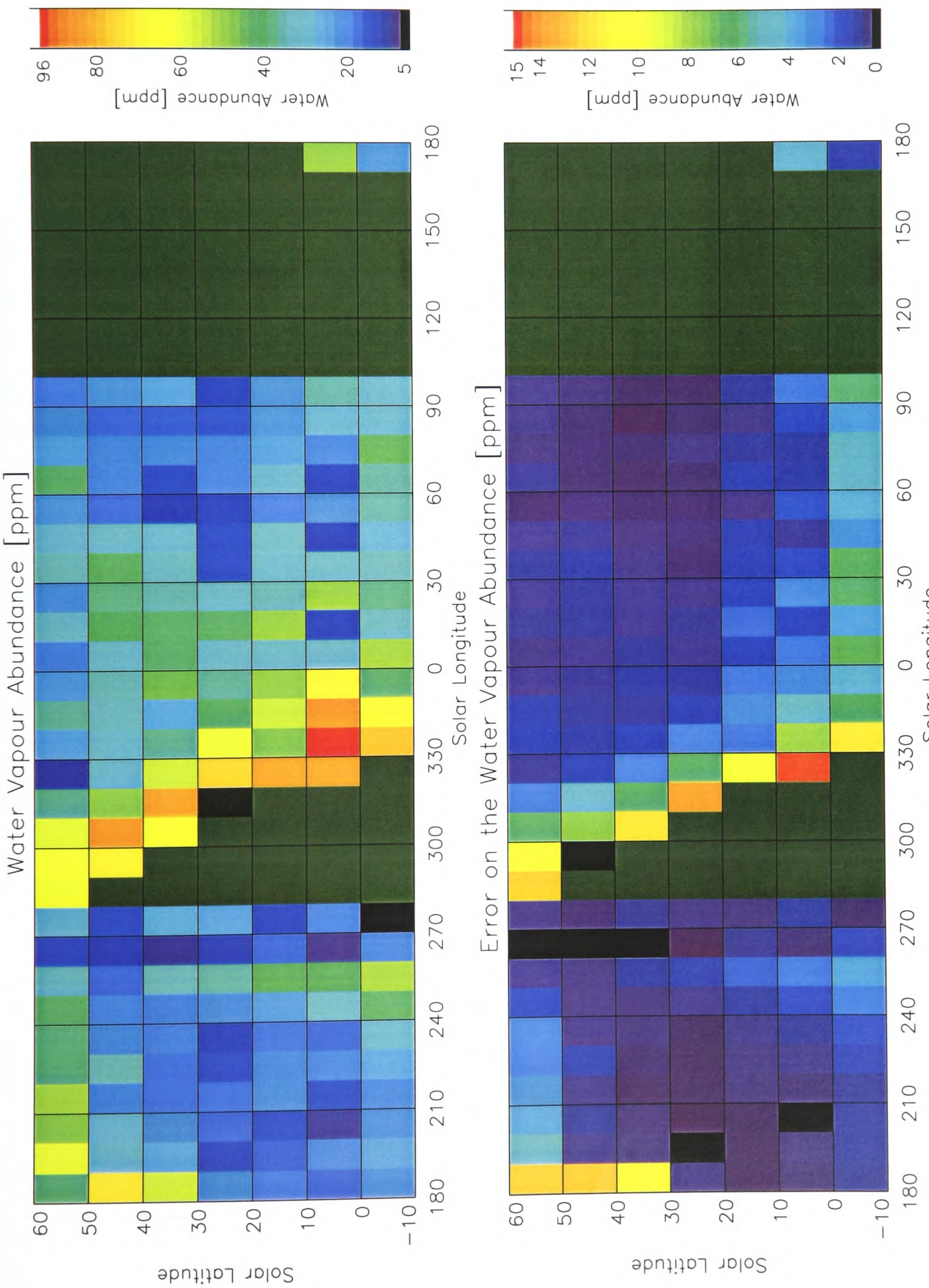

Figure 5.6: *PV OIR* water vapour abundance retrievals and associated errors.

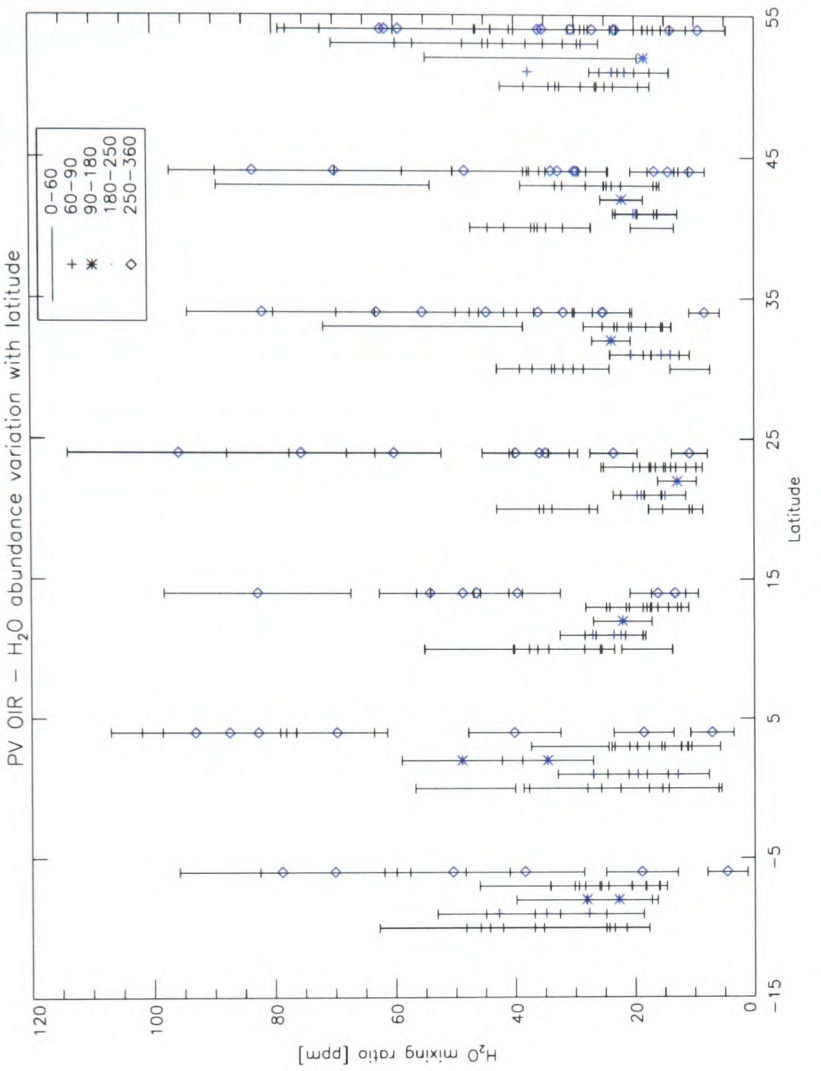

Figure 5.8: *PV OIR* water vapour abundance variation with latitude. The data have been shifted in latitude for clarity purposes.

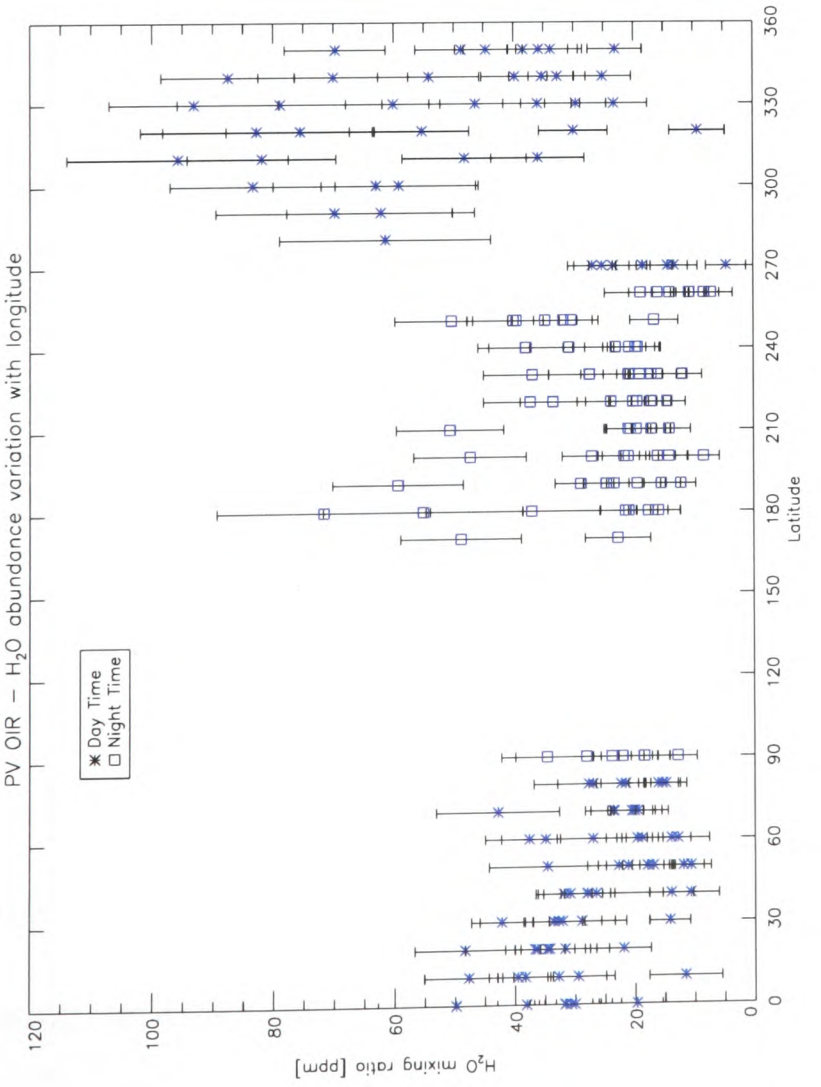

Figure 5.7: *PV OIR* water vapour abundance variation with longitude and associated error bars. The retrieved values shown are the same as those of figure 5.6.

higher temperatures are inferred for that strip than the adjoining latitude/longitude bins.

The retrieved cloud-top pressure and cloud fractional scale height are shown in figure 5.11. The results from the special viewing on-board session spectra (280°E strip) are omitted in this plot. Even though from this colour plate it seems as though there exists high structure in the cloud-top pressure, in figure 5.12 the distinction between day- and night-side measurements is demonstrated more clearly. Starting at the evening terminator (270°E), the cloud-top pressure progressively decreased from a mean of 200 mbars to 150 mbars to reach some of the lowest values observed of 120 mbars at the morning terminator. By the late afternoon/early evening region the cloud has re-established its high cloud-top pressures of ~170 mbars. From figure 5.13, the level of unit cloud optical depth is seen to vary between 60 and 65 km, yielding a mean of 62.5±2.5 km in good agreement with the work of Ignatiev et al. (1999). All on-board and on-Earth *Venera 15* results are included in these line plots. In the bottom panel of figure 5.11, the associated cloud fractional scale height is found to be ~1.0±0.1 times the atmospheric scale height.

The water vapour abundance map derived from the new analysis of the *Venera 15* radiance data is shown in the upper panel of figure 5.14 and its retrieved error in the lower panel. Since, for computational reasons, the natural logarithm of the water vapour mixing ratio in ppm was retrieved, the resultant error is proportional to the final water vapour abundance. The water vapour abundance seems to increase with decreasing latitude (in contrast to Ignatiev et al. (1999) results shown in

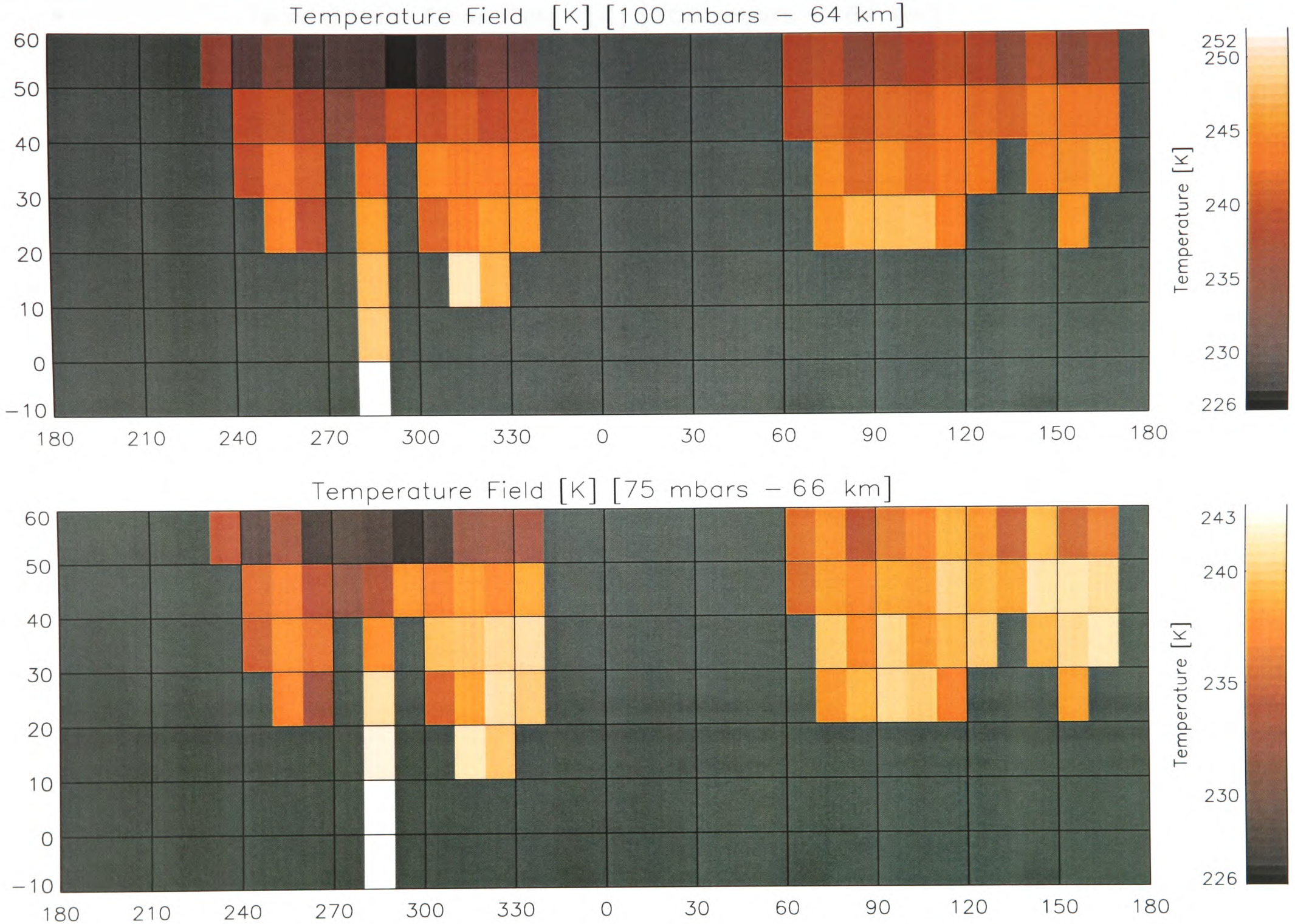

Figure 5.9: *Venera 15* temperature retrievals.

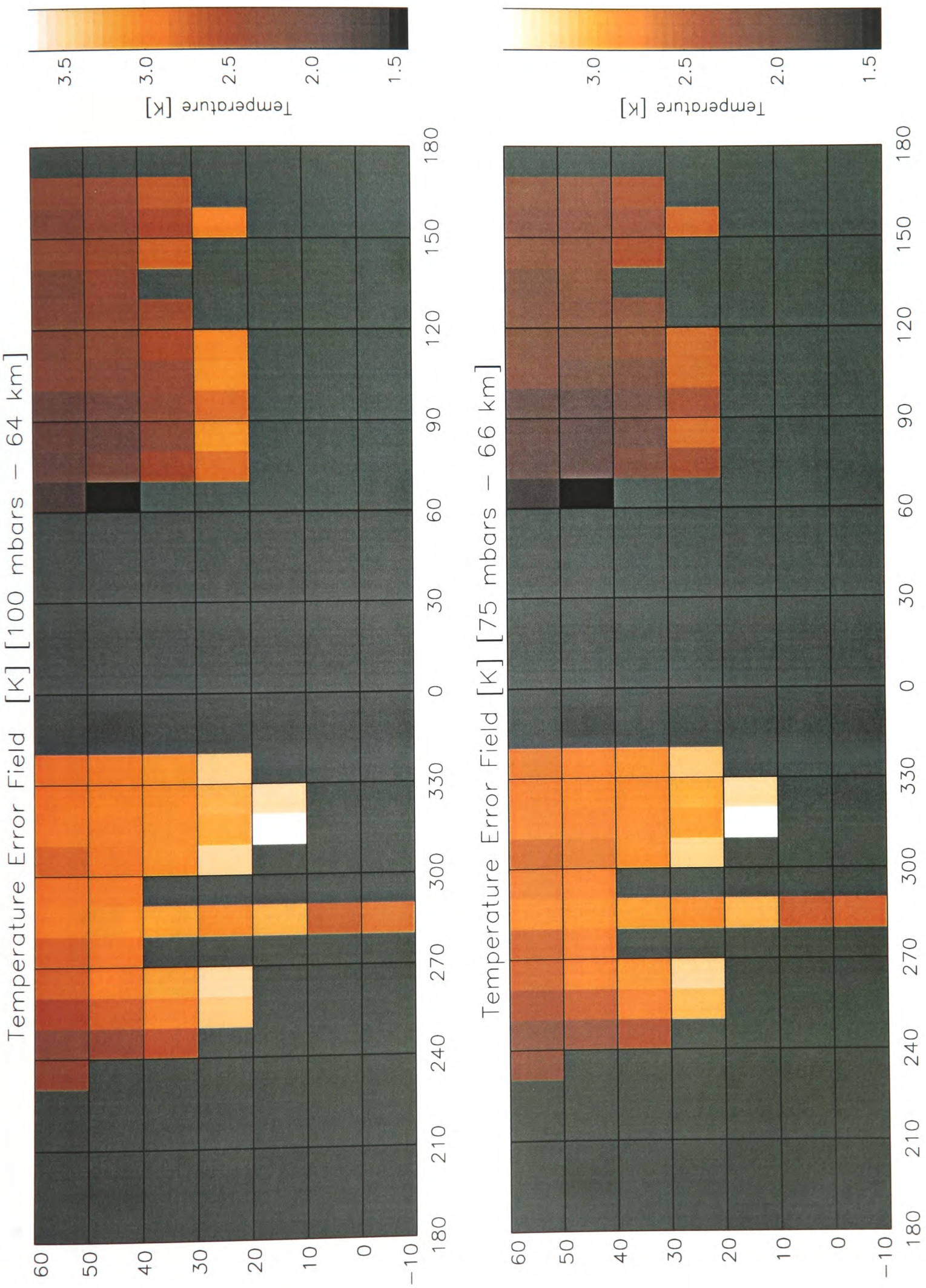

Figure 5.10: *Venera 15* **temperature error retrievals.**

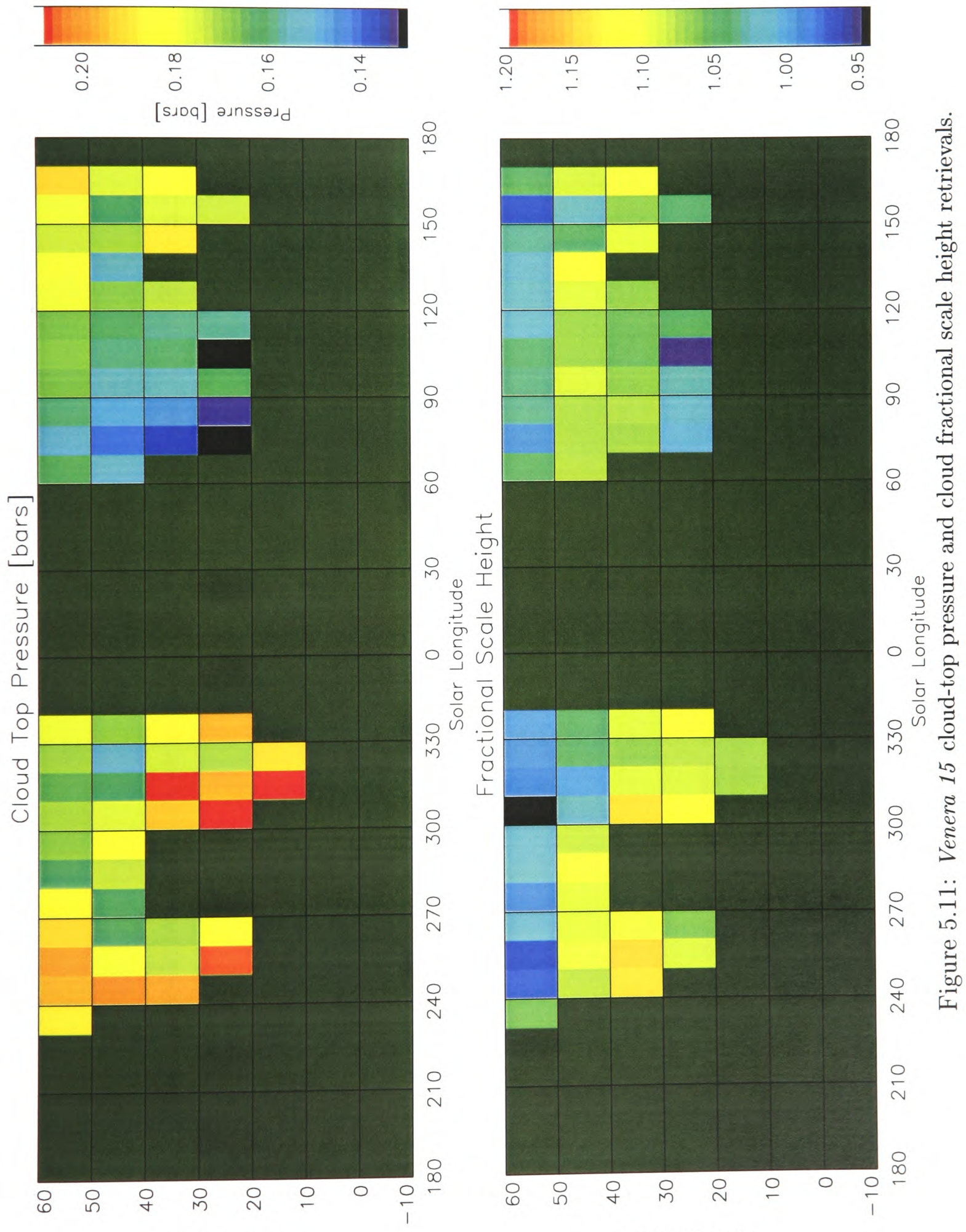

Figure 5.11: *Venera 15* cloud-top pressure and cloud fractional scale height retrievals.

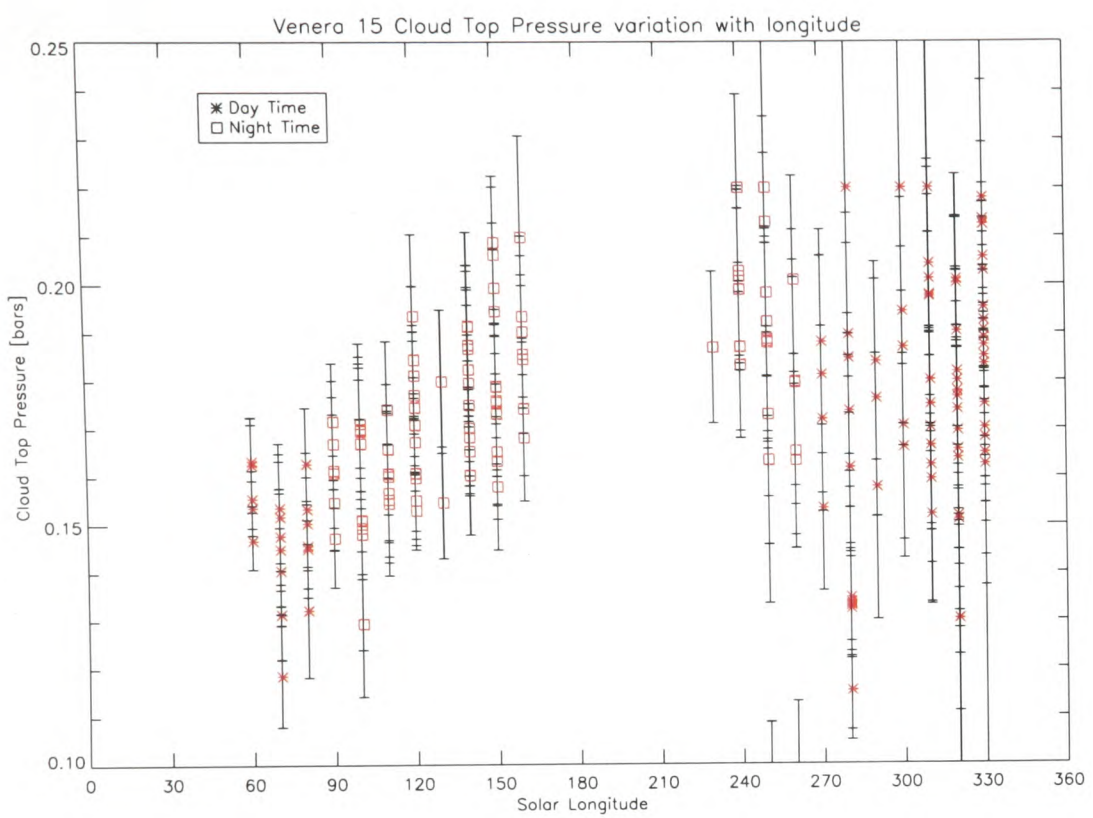

Figure 5.12: *Venera 15* cloud-top pressure variation with longitude and associated error bars. The retrieved values shown are the same as those of figure 5.11.

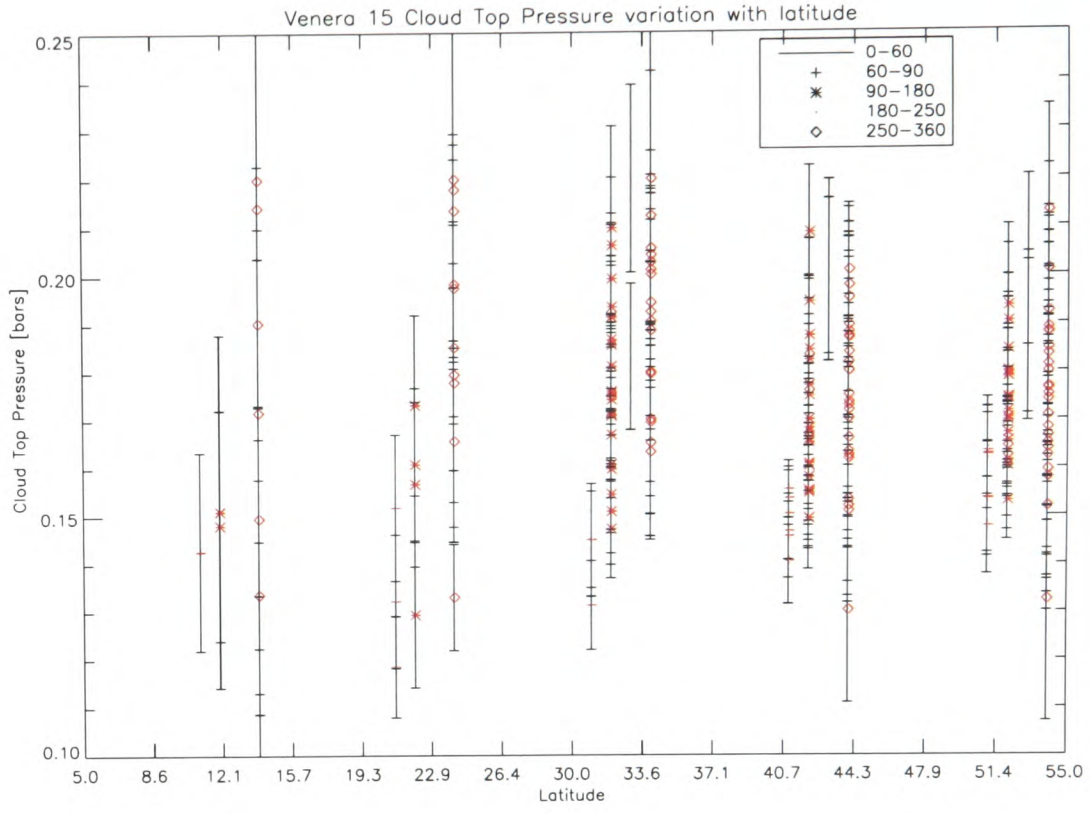

Figure 5.13: *Venera 15* cloud-top pressure variation with latitude. The data has been shifted in latitude for clarity purposes.

figure $2.5_{(2)}$) with the highest values occurring in the daylight hours. However, the large error bars, shown in figure 5.15, do not permit an assessment for day-night variation to be made. On the other hand, the local point-to-point variability first noted by Moroz et al. (1990) cannot be identified either due to the retrieved error bars. The only conclusion that we may reach is that there exists a tentative increase of water vapour abundance with decreasing latitude, as seen in in figure 5.16. The mean water vapour abundance seen in the *Venera 15* observations is thus estimated at 12±5 ppm.

The Viewing Angle Issue

As noted in figure 3.6, there exist *Venera 15* spectra with cosine viewing angle less than 0.25 (75.0°), most of which cover the early afternoon equatorial region. These spectra have a background limb view onto space and not onto the hot sulphuric acid cloud. This poses a logistic problem in their analysis, as there exists no information of the tangent height of view and hence it is not possible to *correctly* model them. We have made efforts to reproduce these spectra, due to their important latitude/longitude placement so close to the equator. The wavenumber region shown in figures 5.17 and 5.18 contains information about water vapour abundance and cloud characteristics. The upper panel depicts the measured and the modelled spectra in brightness temperature space. The residual spectrum, still in brightness temperature space, as well as the measurement noise level, is shown in the lower panel. It is evident that the forward model could not approach the measured

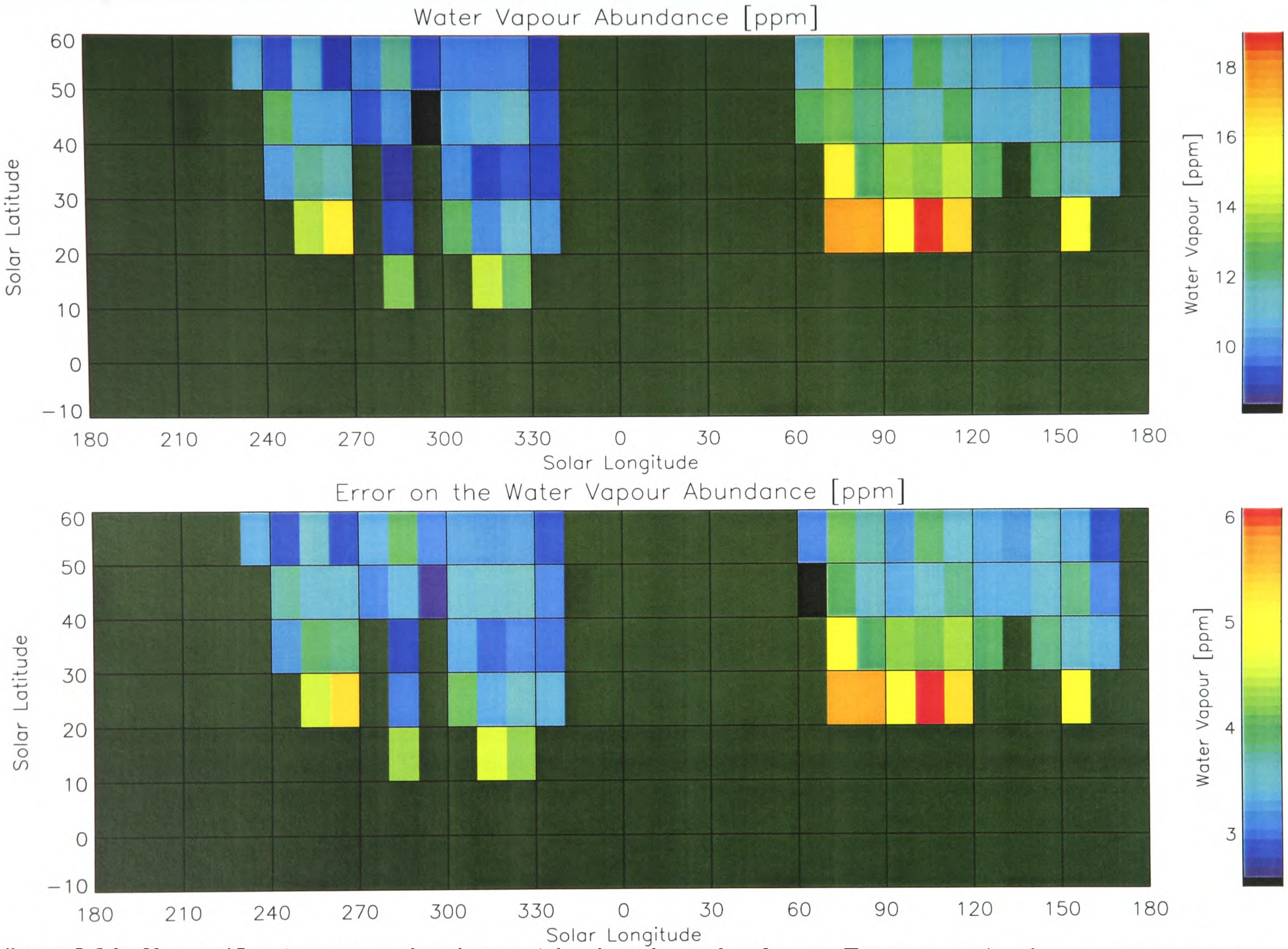

Figure 5.14: *Venera 15* water vapour abundance retrievals and associated error. For computational reasons the water vapour abundance was retrieved as the logarithm of ppm and so the retrieved error is proportional to the retrieved water vapour abundance.

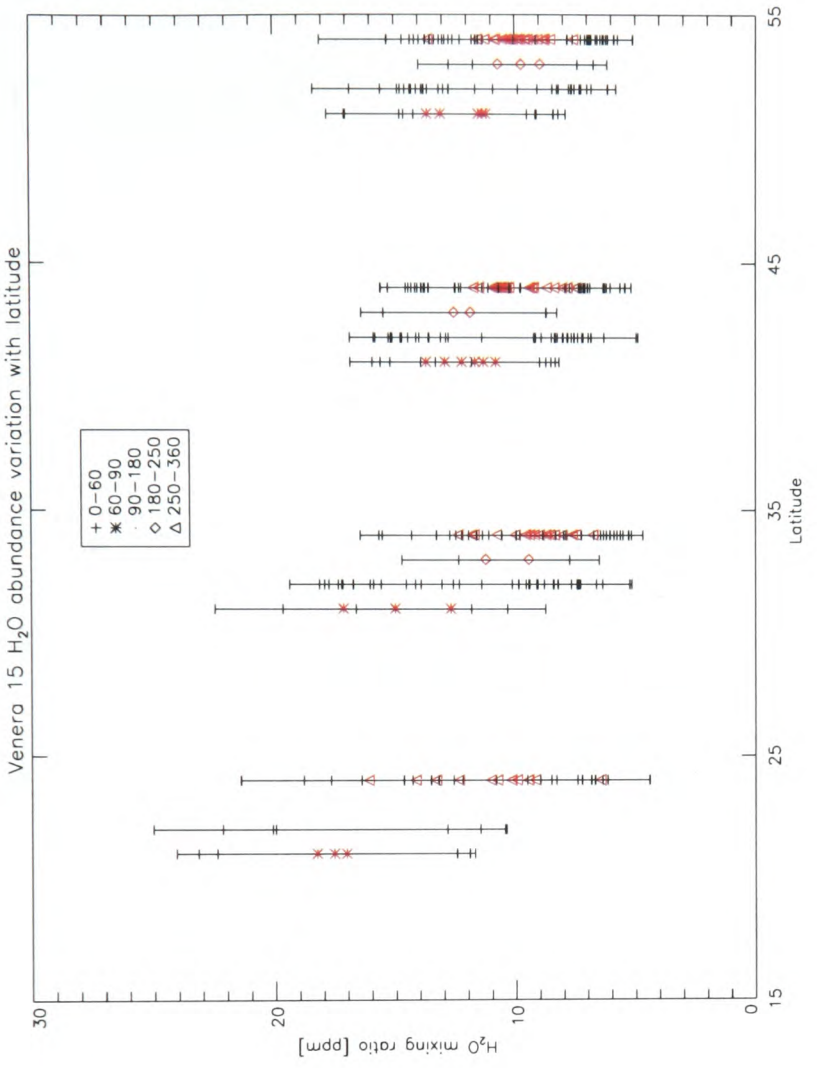

Figure 5.16: *Venera 15* water vapour abundance variation with latitude. The data has been shifted in latitude for clarity purposes.

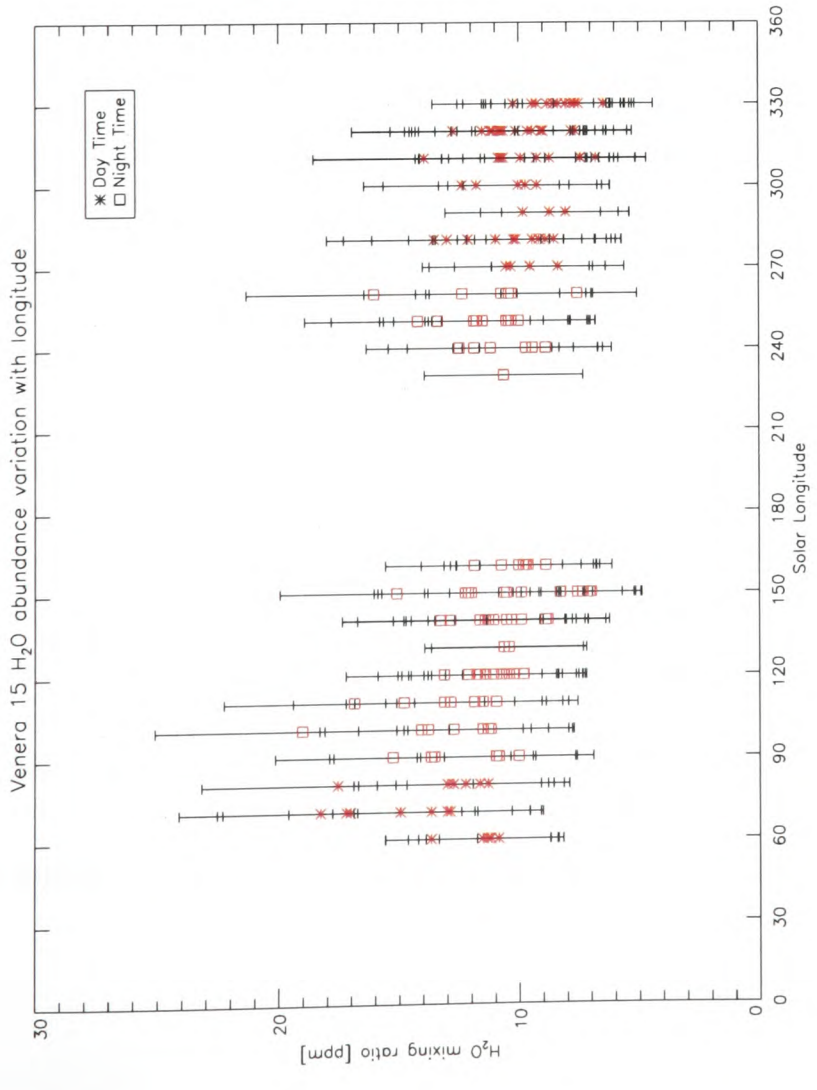

Figure 5.15: *Venera 15* water vapour abundance variation with longitude and associated error bars. The retrieved values shown are the same as those of figure 5.14.

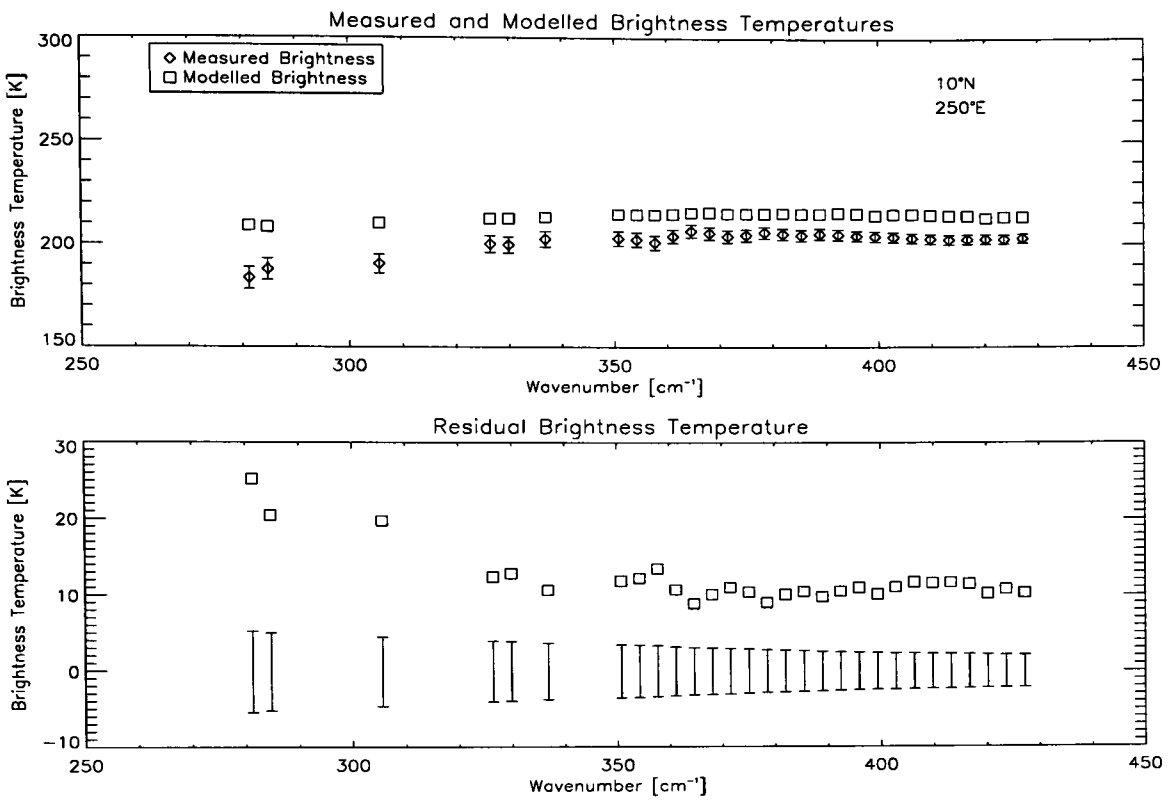

Figure 5.17: Upper panel: measured and modelled *Venera 15* spectrum with small cosine viewing angle. This spectrum is much colder than the nadir viewing ones and the forward model is unable to simulate it accurately. Lower panel: The residual spectrum and associated measurement error bars.

spectrum within noise levels in this case, due to lack of physical knowledge required to correctly reproduce the radiation seen. An example of measured and modelled spectrum in the 10°N, 100°E bin that does not suffer from the viewing angle problem is shown in figure 5.18. The residual spectrum is within measurement errors for the entire region. All *Venera 15* spectra with associated cosine viewing angle less than 0.25 (75.0°) were hence discarded. The *PV OIR* spectra do not "suffer" from any correlation between latitude/longitude and viewing angle as the Pioneer Venus orbiter was spin-stabilised. Hence, most latitudes and longitudes were observed with a variety of viewing geometries, as was shown by the colour bar in figure 3.2.

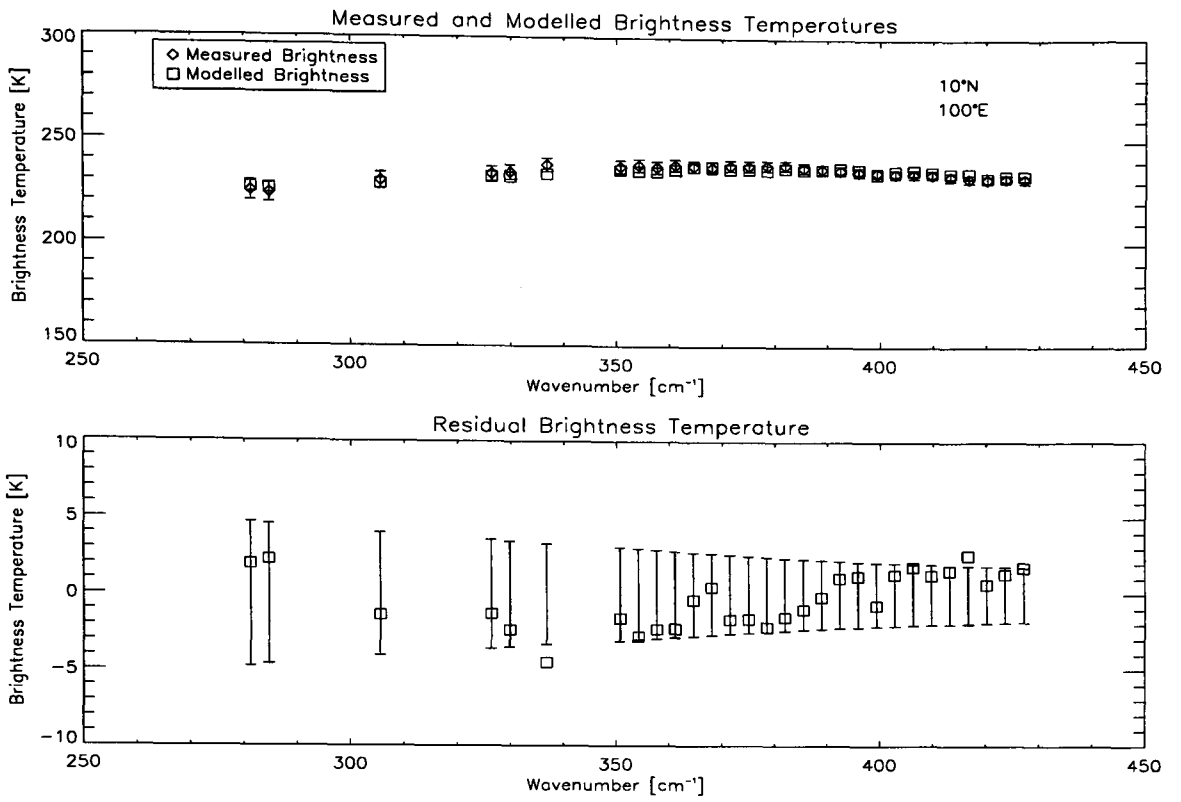

Figure 5.18: Upper panel: measured and modelled *Venera 15* spectrum with average cosine viewing angle. Excellent agreement was achieved in this case. Lower panel: The residual spectrum and associated measurement error bars.

5.3 Joint Results

One of the main goals of this thesis is to validate the individual results of the *PV OIR* and *Venera 15* observations via a common analysis technique. The figures shown in this section contain two global maps, one for each instrument, where only the areas of common coverage are shown. Whenever possible, the same limits were used in the colour bars to facilitate the comparison. We will refer to the two areas covered by the instruments as the "morning terminator" region (60° to 90°E) and "evening terminator" region (230° to 330°E) even though the evening terminator area covers most of the afternoon hours as well.

The temperature composite image, shown in figure 5.19, offered no great insights in view of the isothermal state of Venus' middle atmosphere. On the contrary, the

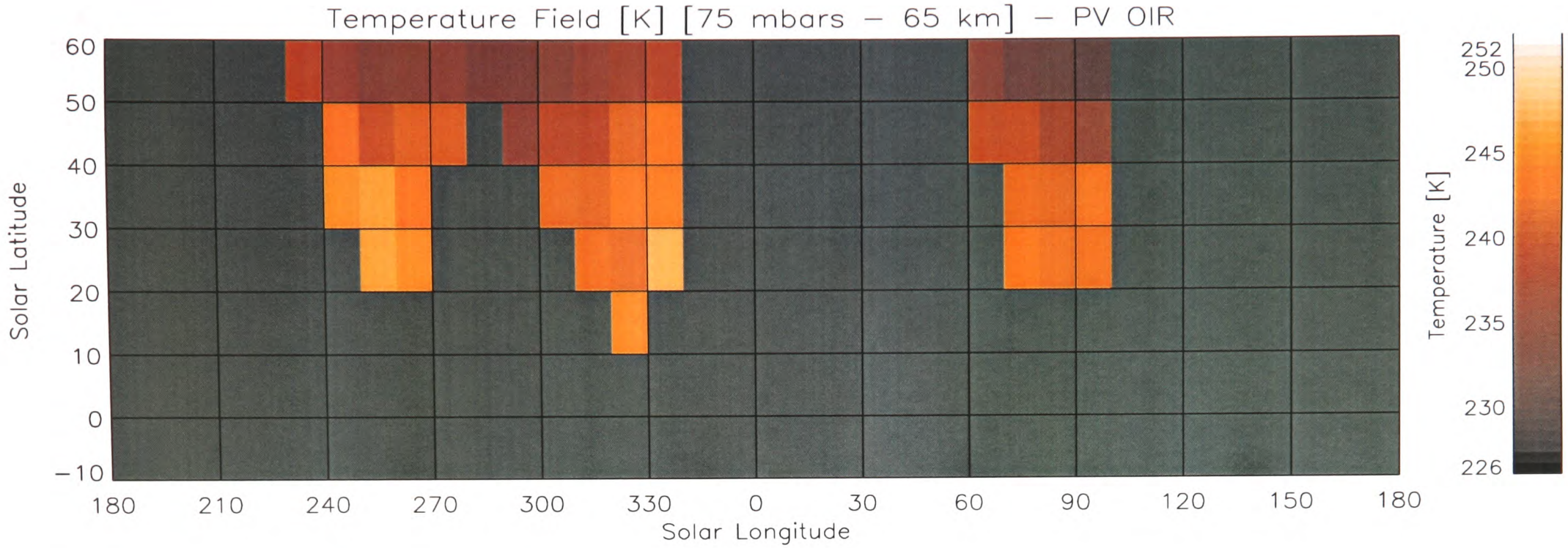

Figure 5.19: *PV OIR* and *Venera 15* temperature retrievals.

cloud-top pressure plot, figure 5.20, revealed a very interesting result. In the morning terminator region similar cloud-top pressures were retrieved from both datasets in direct contrast to the evening terminator region where the *Venera 15* cloud-top pressure (lower panel) was found at ~50 mbar higher (~2.5 km lower) than the *PV OIR* cloud-top pressure (lower panel.) As a direct consequence of these cloud-top pressure findings, the water vapour abundance maps for the two instruments are now placed in a different perspective than initially envisioned. In figure 5.21, the morning terminator regions show homogeneity with an approximate 20-30 ppm of water vapour. In the early afternoon however, before the 270° parallel, this picture is reversed, with the *PV OIR* plate (upper panel) having a marked dayside enhancement of up to 80 ppm and the *Venera 15* plate (lower panel) showing a slight decrease to ~10 ppm. The possible effect of the changes of cloud-top pressure on the observed water vapour abundance is extensively discussed in section 6.4, where the variation of both parameters with longitude is investigated.

5.4 Validation of Results

In understanding problems with multiple variables, the question of uniqueness of the solution is one which always must be addressed, along with the critical assessment of errors. The validation of the forward model, the retrieval technique and the final results is a procedure that compliments the analysis of remote sounding observations. In the following section, we recapitulate some of these issues already discussed throughout chapter 4, we describe a number of further tests performed during the

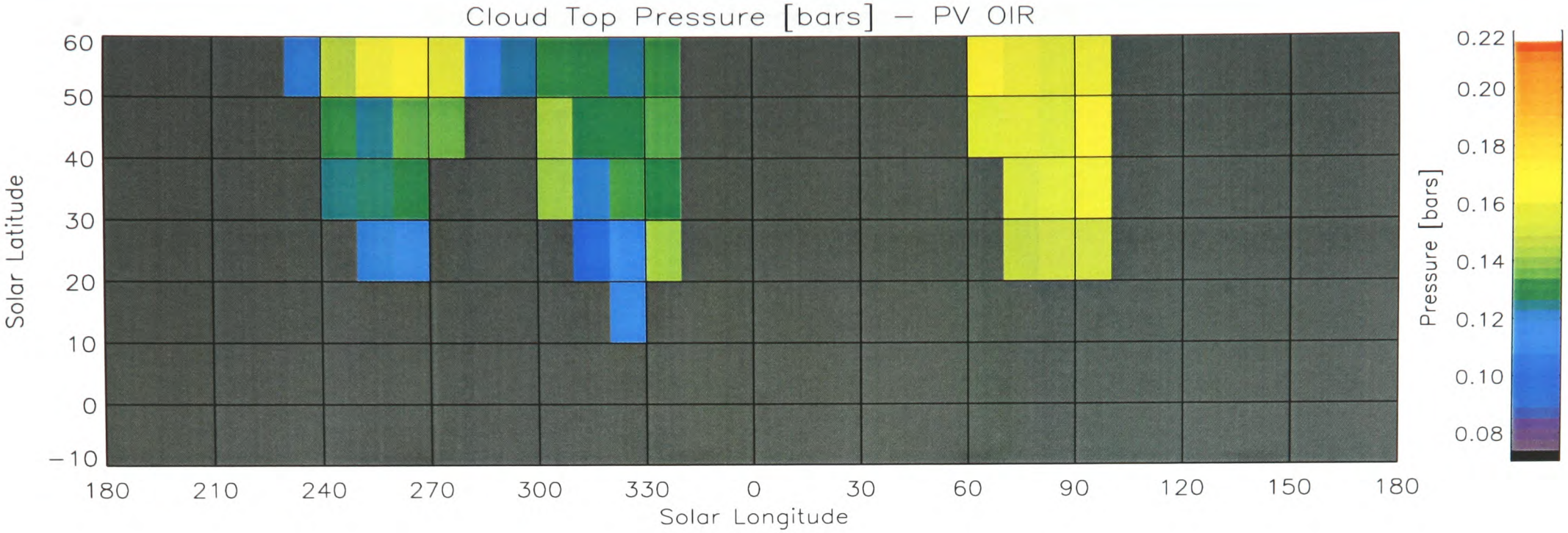

Figure 5.20: *PV OIR* and *Venera 15* cloud-top pressure retrievals.

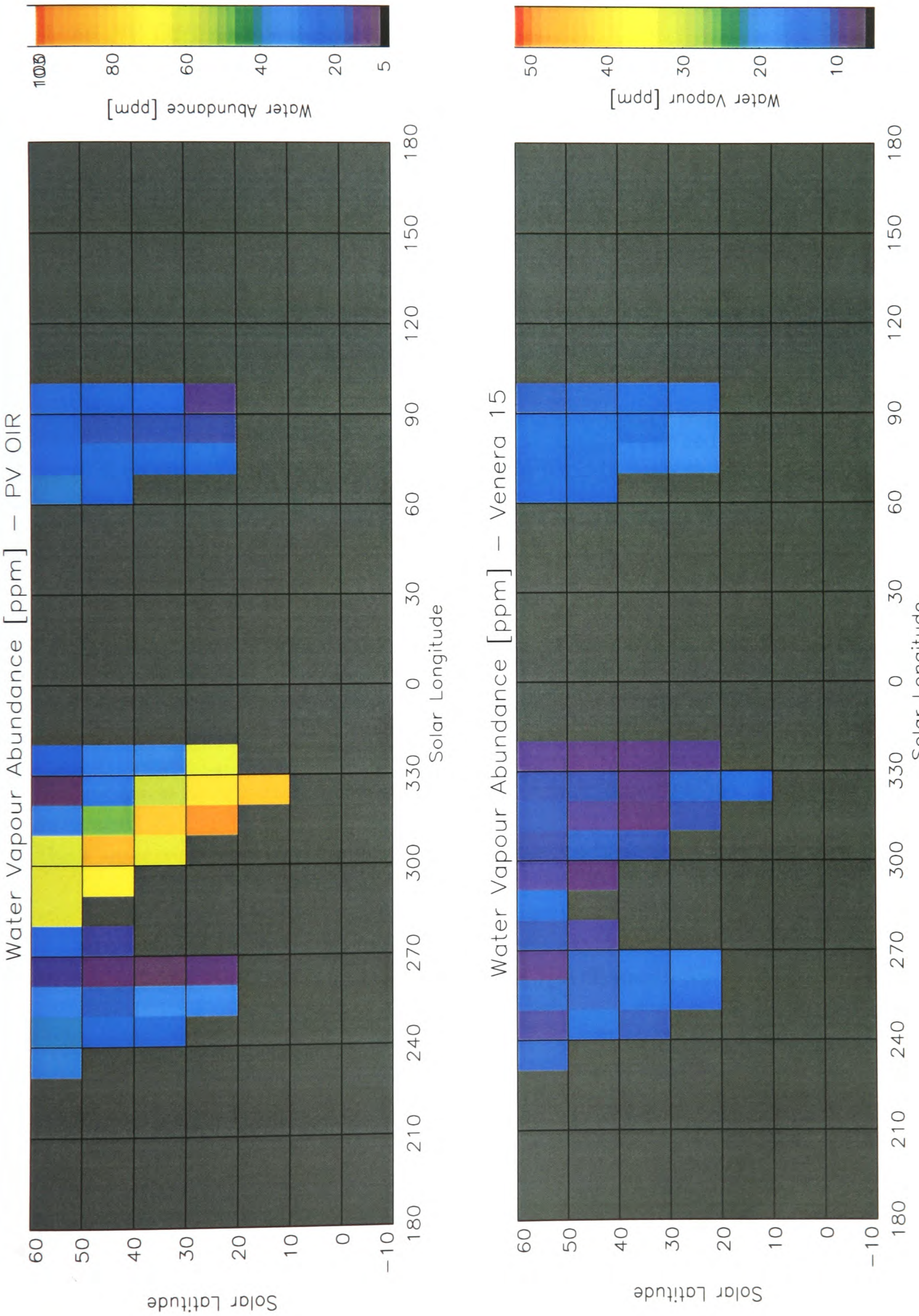

Figure 5.21: *PV OIR* **and** *Venera 15* **water vapour abundance retrievals.**

analysis and thence present the reasons which install confidence in the new retrievals of the *PV OIR* and *Venera 15* measurements.

The initial reduction of both data sets by projecting their measurements onto a grid of nine different viewing angles, discussed in sections 3.1 and 3.2, requires no further deliberation. Extensive work has been further performed on the *Venera 15* spectra via the diagnostic tools described in section 4.4.3 in order to exploit the spectral points with maximum information content. By selecting and retrieving the best spectral channels not only does the computational time decrease, but also the noise in the modelled radiances is reduced and hence, the retrieval converges to the respective solution more effectively.

The effect of the non-temperature retrieved parameters on the modelled radiation depends on the efficiency of the forward model to capture the contribution of the variation of each individual parameter on the predicted radiance *independently* of the contribution by the rest of the parameters. Hence, the correlation of the elements of the $\mathcal{K}$-matrix for the non-temperature parameters (i.e. the two cloud parameters and the water vapour abundance) was checked in the beginning of the retrieval process. Pearson's Standard Test (Press et al., 1995) was used for this purpose. It was verified that no significant correlation (always less than 0.1, for both datasets) exists between the cloud-top pressure/water vapour abundance and the fractional cloud scale height. However the cloud-top pressure and the amount of water vapour visible by the satellites are not completely un-related. In simple terms, an atmospheric path with high cloud-top pressure and low water vapour column abundance *might*

produce a similar intensity of radiation, as a path with lower cloud-top pressure and higher water vapour column abundance. Hence, the combined cloud-top pressure and water vapour abundance retrieved result may be anti-correlated, if one could ignore for the sake of the argument the fact that different cloud-top pressures will differ in their temperature structures as well. For the case of the *PV OIR* data, this anti-correlation was less than 0.5 for all cases bar for latitude/longitude bins with one or two sets of measurements, where it rose to ~0.7-0.8. For the case of the *Venera 15* data, the coefficient was always small (less than 0.3) bar the cases of very small cosine viewing angle (limb viewing) where the forward model could not perfectly model the incident radiance. However, as discussed in section 5.2, spectra with cosine viewing angle less than 0.25 were excluded from the analysis.

The retrieval technique was substantiated via the "bias error" investigation (section 4.4.2), whereupon the retrieval was initialised with a synthetic spectrum created with known input profiles and returned those same input profiles as retrieved products. In addition, three different retrieval techniques, namely the linear relaxation technique of Rodgers (1976), the statistical regularisation of Ustinov (1991) and the non-linear relaxation method of Chahine (1972) have resulted in approximately similar solutions. Even though these retrieval formalisms are based on different principles, the information contained in the *PV OIR* and *Venera 15* observations is substantial and led these diverse mathematical formalisms to the same solution. The stability of the retrievals was also verified using a number of different input parameters, for example, different *a priori* and/or initial guess

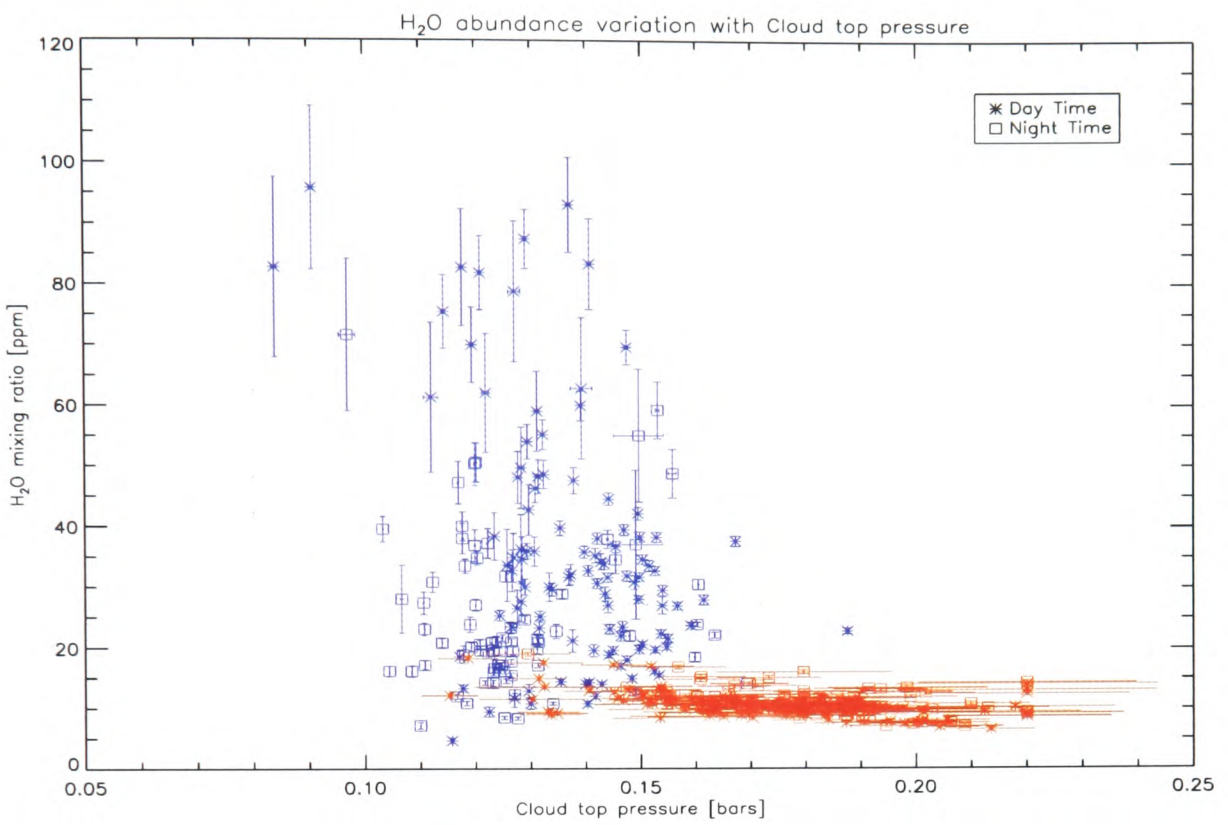

Figure 5.22: *PV OIR* and *Venera 15* cloud-top pressure and water vapour abundance retrievals. Results from the common bins are only shown. The blue markers show the *PV OIR* data and the red markers the *Venera 15* data.

temperature and absorber profiles. A suite of extreme cloud-top pressures and water vapour abundances were used as initial guess and verified the robustness of the retrieval in finding the same solution. A particularly rigorous test was to use the retrieved cloud parameters, water vapour abundance and temperature field of the *PV OIR* measurements as an initial guess for the *Venera 15* retrievals, and vice versa. The results remained within retrieved error, for both datasets, verifying that most information in the retrieved results does originate from the measurements themselves and not in the choice of *a priori* and initial guess profiles.

One final concern has been the possibility that the retrieval technique has retrieved cloud-top pressure and water vapour abundance for both sets of measurements, that belong to the same solution space. This concern is different from the

correlation-type effects between cloud-top pressure and water vapour abundance discussed previously. Here we are discussing the capability of both the forward model and retrieval code to accurately distinguish between different possible solutions and converge towards the most probable. This capability depends on the accuracy of the measurements, on the ability of the forward model to distinguish between different contributions to the radiation observed and on the retrieval technique to result in the correct solution. The two latter issues have already been addressed above. The former one is discussed below.

For the *PV OIR* and *Venera 15* measurements, even though the radiation sensed by the *PV OIR* water channel at 228 cm^{-1} and the *Venera 15* pure rotational water spectral points is "contaminated" with cloud absorption features, both instruments have dedicated cloud sensing channels, namely the *PV OIR* channel at 872 cm^{-1} and all the *Venera 15* cloud channels revealed by the diagnostic selection performed. Hence, we are confident that most cloud information is obtained from a separate spectral region than from the water vapour rotational band region and that, within their respective retrieved errors, the two solutions for the *PV OIR* and the *Venera 15* observations are indeed unique. The retrieved cloud-top pressure and the water vapour abundance from both instruments is shown in figure 5.22. The blue markers show the *PV OIR* results and the red markers the *Venera 15* results. All common latitude and longitude bins are included in this figure. Due to the vertical scale used, the *Venera 15* error bars overwhelm the *Venera 15* result data points themselves. It is evident that the two sets of results occupy different areas of the solution space,

strengthening our belief that the analysis has performed adequately in retrieving cloud-top pressure, water vapour abundance and temperature from the *PV OIR* and *Venera 15* observations. To further satisfy ourselves that this was indeed the case, the *PV OIR* results were used as input to create synthetic *Venera 15* spectra which were then compared to the real *Venera 15* spectra for the specific latitude/longitude bin, and vice versa. In both cases, the spectral regions sensitive to cloud and water vapour absorption features of the synthetic spectrum did not agree with the real spectrum and were well outside the measurement error. This fact certifies that the atmospheric state changed sufficiently between the two visits and that, had it not, both sets of observations should have converged to the same cloud-top pressure and water vapour abundance solutions.

In conclusion, the joint analysis of the *PV OIR* and *Venera 15* observations has been validated and we are confident that the novel treatment of the measurements using new radiative transfer and retrieval algorithms has led to indisputable and unbiased results. Our faith in the accuracy of the analysis is leading us to conclude that during the *PV OIR* visit both cloud-top pressure and water vapour abundance showed elevated variability whereas during the *Venera 15* visit there was almost no variation in the water vapour abundance but high and well-structured variability in the cloud-top pressure.

5.5 Synopsis

The main features of Venus' middle atmosphere revealed by the common analysis of the *PV OIR* and *Venera 15* observations are summarised here. The *temperature structure*, as seen by both instruments, was found to be almost isothermal with variations of 5-10 K. The *cloud-top pressure* has a minimum of ~110±10 mbars in the evening equatorial region and a maximum of ~160±12 mbars in the morning mid-latitude regions in the *PV OIR* data. In the *Venera 15* observations, the cloud-top pressure increases steadily after the morning terminator from ~120±10 to 200±30 mbars in the late afternoon/early evening region. The day-night variation in *water vapour abundances* seen by the *PV OIR* instrument was found to fluctuate from 10±5 ppm at night up to 85-95±15 ppm in the equatorial region right after the sub-solar point, the wet spot region. The mean *Venera 15* water vapour abundances were found to be of the order of 12±5 ppm with no clear day-night distinction. In the following chapter, possible physical explanations for the above observations are developed and elaborated upon.

Chapter 6

Physical Explanations

The analysis of the observations of Venus' middle atmosphere made by the *PV OIR* and *Venera 15* instruments have been presented in the previous chapter in the form of temperature structure, cloud-top pressure and water vapour abundance global maps. In this chapter the possible physical explanations behind these observations are discussed with particular focus on the water vapour abundance distribution. The complexity of the Venus cloud system provides no assurances that the behaviour of the water vapour abundance will be as straightforward as the more or less homogeneous temperature structure of the Venus middle atmosphere at low and middle latitudes.

Recapitulating the information provided by the results in the previous chapter; the *PV OIR* experiment has observed a significant day-night variation in the water vapour abundance content of the cloud-top Venus atmosphere. Furthermore, a local enhancement of water vapour is retrieved in the sub-solar equatorial region, above

mean day-side abundances. The *Venera 15* observations, due to their small coverage of the equatorial and mid-latitude atmosphere cannot offer a clear global picture of the water vapour abundance. During the *Venera 15* orbiter visit no day-night water vapour abundance variation is observed, or strong local enhancements.

In the following, we will discuss on a more theoretical level the physical significance behind the local water vapour enhancement and the cloud-top pressure variability.

6.1 Introduction

A number of ideas based on simple physical principals have been put forward in the past, in order to explain the observed diurnal and local variability of water vapour abundance using simple but informative arguments. In the following we develop and discuss an original idea briefly mentioned in Schofield and Taylor (1982).

They conjectured that the latitude and local solar time variability of the global water vapour abundances and especially the concentration of water vapour above the clouds in the equatorial day side may be generated by solar radiation heating the cloud aerosol particles at the sub-solar point. This would imply that a 75% H_2SO_4 and 25% H_2O cloud particle composition would turn, for example, into a 80% H_2SO_4 and 20% H_2O composition, releasing 5% as free water vapour in the upper cloud deck in the early afternoon. As H_2SO_4 droplets get warmer, water molecules, previously enclosed in the droplets, evaporate. This increases the acid concentration of the droplets and reduces their mean radius. This alters their

extinction coefficient and absorption characteristics and hence the contribution to the observed radiance. This contribution is not linearly related to the mean radius, distribution or acid concentration of the droplets and a simple prognosis of the effect of altering these clouds parameters is hence impossible. A simple numerical calculation shows that the local heating of the sulphuric acid droplets at the sub-solar point, which evaporates water from them, and so increases the column abundance of water which is detected in the vapour state cannot explain the order of magnitude enhancement seen (Irwin and Taylor (1996), model 1.) The main reason is that the actual amount of water enclosed in the H_2SO_4 droplets is far smaller than a mean ambient water vapour abundance of ~20 ppm at the cloud tops and will add little to the total water vapour abundance even if all droplets become completely evaporated.

6.2 The existence of wet spots

A more promising idea proposes that convection might occur at deeper levels in the sub-solar region and, coupled with uplift of water from deeper moister levels to the cloud tops, may explain the observed selective concentration of water vapour. This conjecture demands a more careful consideration as there are two prerequisites for its validation; firstly, excess water vapour and sulphur dioxide must exist in the lower and middle cloud layers and secondly, convection, or some vertical mixing motion, must occur in the lower cloud levels.

6.2.1 The presence of H_2O and SO_2

First of all, the existence of surplus water vapour and sulphuric acid in the lower and middle cloud layers is substantiated by discussing experimental evidence for the lower cloud region and also for the cloud-tops. Recalling table 2.4, the *in situ*measurements of Venera 11, 13, 14 and Pioneer Venus Sounder probes did report high water vapour abundances in the 40-55 km altitude region, of the order of 1000±500 ppm. Since all three of these probes landed approximately at the sub-solar point (see figure 2.3), they provide direct measurement of the conditions within the cloud at this very interesting equatorial region. The cloud-top water vapour abundance has been observed by the *PV OIR* and *Venera 15* experiments (Schofield et al., 1983; Ignatiev et al., 1999) and was found to vary between 10 and 100 ppm. Our study confirmed the day-night variation in the *PV OIR* data and the moderate local variability of the *Venera 15* observations (figures 5.6 and 5.14.)

Accordingly, below the main cloud deck, the abundance of SO_2 was derived to be 120±20 ppm near 42 km altitude from Vega 1, 2 observations (Bertaux et al., 1996) whereas Earth-based studies also yield 130±40 ppm in the 35-45 km region (Bézard et al., 1993). Photochemical models further corroborate the high abundances in the lower cloud layers. Krasnopolsky and Parshev (1983) calculated the photochemical stability of a number of minor species in Venus' atmosphere between 50 and 100 km and reported that a SO_2 abundance of 130 ppm and H_2O abundance of 150 ppm at 50 km altitude were required for their calculations. The cloud-top abundance of SO_2 is shown to be between 10 - 100 ppb from the ultraviolet spectroscopy from

the P V Orbiter in the years 1978 to 1986 (Esposito et al., 1988). A common study of infrared measurements from *Venera 15* and the ultraviolet measurements from the P V Orbiter revealed that, at low and mid-latitudes, the SO_2 mixing ratio spans from 10 to 1000 ppb between 62 and 69 km altitude (Zasova et al., 1993). A significant depletion of the species is hence expected inside the cloud region and this is indeed provided by the photochemical region of formation of H_2SO_4. Both Yung and DeMore (1982) and Krasnopolsky and Parshev (1983) have shown that the H_2SO_4 formation occurs within a thin layer centred at ~60 km altitude. So, it might be expected that any excess water vapour and sulphur dioxide that rises from the lower cloud levels will quickly photodissociate to create H_2SO_4 droplets.

A brief discussion on the chemical processes responsible for the dissociation of H_2SO_4 is imperative at this stage. H_2SO_4 is thermally decomposed in the lower, hotter atmosphere at 432K (Bullock and Grinspoon, 2001), following the composite reaction: $H_2SO_4 + CO \longrightarrow SO_2 + H_2O + CO_2$. To be precise, H_2SO_4 is decomposed into SO_3 and H_2O in the first instance. Then, SO_3 is transformed into SO_2 through reacting with CO and producing SO_2 and CO_2 (von Zahn et al., 1983). Radio occultation measurements have verified this process through observations of H_2SO_4 vapour mixing ratios dropping rapidly below the 38 km altitude (Jenkins et al., 1994). The products of the reaction, SO_2 and H_2O, are available to be transported upwards.

6.2.2 Convection and other dynamical effects

Having argued for the presence, and the physical meaning behind the presence of both water vapour and sulphuric acid in the cloud region of Venus, the possibility of convection occurring at equatorial altitudes is now examined via the eddy diffusion coefficient. The vertical eddy diffusion coefficient, used in the calculation of the typical vertical motion timescales, exhibits a curious behaviour in the middle altitudes of Venus. From radio scintillation experiments Woo et al. (1982) deduced a value of $\sim$0.2 m^2 s^{-1} at 45 km altitude (45°N), whereas in the 51-56 km altitude a much larger value is required in order to represent convective mixing. Convective activity was observed at low latitudes (see figure 2.3) by the Vega balloons (Blamont et al., 1986) and further postulated in Schubert (1980) based on observations of unstable stratification in the lower cloud levels. The value of eddy diffusion coefficient adopted for those altitudes is hence $\sim$ 140 m^2 s^{-1} based on calculations from the observations of static stability by Imamura and Hashimoto (1998). Photochemical modelling above the cloud levels by Krasnopolsky and Parshev (1983) and Yung and DeMore (1982) resulted in a coefficient of 2 m^2 s^{-1} above the 60 km level. The characteristic time for vertical diffusion is given by H^2/K, where H is the scale height of the atmosphere and K the eddy diffusion coefficient. The scale height decreases from $\sim$7.8 km at 40 km altitude to $\sim$5.8 km at 60 km altitude. Hence, below the clouds the vertical mixing time scale is $\sim$ 3500 days, in the convective region $\sim$4 days and at the cloud-top $\sim$ 200 days. Schubert (1980) included turbulence and small-scale upwelling and downwelling in his models of the equatorial cloud region in order to

explain the Pioneer Venus observations. Based on the great uncertainties on the small scale dynamical effects and their unknown interaction with the well-defined photochemistry regions, the idea of vertical transport bringing species from the lower Venus cloud to the cloud-top region seems reasonable and adapted in the remainder of this discussion as valid. The transport of SO_2 from below the clouds to higher levels due to atmospheric motions is also favoured by Na and Esposito (1997), from their recent UV observational campaign of Venus.

In conclusion, a tentative explanation both for the presence of excess water vapour and sulphur dioxide at lower cloud levels and their vertical transport has been discussed. Wet spots may therefore appear at the cloud tops, as postulated by a number of scientists whose work was presented in chapter 2, e.g. Barker (1975b); Oyama et al. (1980); Surkov et al. (1982); Revercomb et al. (1985). However, the argument is not completed here. In order to fully understand the *PV OIR* observations we are further required to explain the disappearance of the wet spot in the evening equatorial Venus cloud-top atmosphere.

6.3 The disappearance of wet spots

In figure 5.6, due to the smaller binning of the observational data compared to previous works, a significant westward trend with increasing latitude was revealed in the shape of the wet spot. As a first glance, it might look as if a poleward wind has transported material from the sub-solar point northwards and the super-rotational zonal wind has transported it westwards. In this section, we discuss why

such dynamical explanations fail to completely encompass the problem.

The prevailing zonal wind at the equatorial latitudes and altitudes is westwards at 90-100 m s^{-1} so it it would take ~15-20 minutes for an equatorial parcel of air to travel 1° westwards, or to cover ~105 km. As was seen from figure 1.8 there is a strong decrease of the super-rotational wind with increasing latitude with wind speeds decreasing to 40-80 m s^{-1} at 30-50°N. So, in mid-latitudes, it would take ~20-45 minutes to travel 1° westwards. Now, the poleward circulation of Venus has been revealed through near-infrared cloud images at 50 km altitude (Belton et al., 1991; Carlson et al., 1991) and through UV cloud motion tracking at 65 km altitude (Del Genio and Rossow, 1990). The poleward velocity was found to be of the order of 2-5 m s^{-1}. Each latitude degree is ~210 km so a parcel of air will take ~1.2 days to travel 1° northwards. It becomes clear that the zonal wind component completely overtakes the northwards one.

In addition, the wet spot was observed for three solar hours, or 45° in solar longitude (4725 km), as seen in figure 5.6. Assuming an equatorial zonal wind of 100 m s^{-1}, an air parcel will have to travel ~13-14 hours in order to cover the distance. During this time frame, the excess water has to vanish from satellite view, as can been seen in the figure. If the water vapour did not disappear then the zonal winds would quickly transport it around the planet and the *PV OIR* observations would show an zonal equatorial region water vapour enhancement. However, no such zonal enhancement is observed in the data which testifies that the water vapour must be depleted within ~13-14 hours from the sub-solar point.

Two simple mechanisms are proposed for the water vapour disappearance; firstly, that water vapour condenses onto H_2SO_4 droplets within a few hours and hence cannot be observed in the infrared range anymore and secondly, that an "avalanche" effect takes place, with water vapour condensing onto H_2SO_4 droplets, changing the delicate balance of the Venus cloud composition and changing its cloud-top pressure and overall cloud structure. In the following, we discuss these two ideas in turn.

In order to discuss the possible sinks of water vapour in the Venus cloud system, a description of the photochemical creation of H_2SO_4 is required. After (Krasnopolsky and Parshev, 1983), the H_2SO_4 cycle is described by:

$$SO_2 + h\nu \longrightarrow SO + O$$

$$SO_2 + O + CO_2 \longrightarrow SO_3 + CO_2$$

$$SO_3 + H_2O \longrightarrow H_2SO_4$$

$$SO + SO \longrightarrow SO_2 + S$$

If the droplets are 85% H_2SO_4 by weight, then the above reactions can be summarised in the following:

$$3SO_2 + 4H_2O \longrightarrow 2\,(H_2SO_4 \cdot H_2O) + S$$

The net result of the H_2SO_4 cycle is given by Krasnopolsky and Pollack (1984) as $3\ SO_2 + 2\ h\nu \longrightarrow 2\ SO_3 + S$ which basically divulges that the production rate of SO_3 is this equal to 2/3 of the photodissociation rate of SO_2. As a result, three SO_3 molecules can remove four H_2O molecules in order to create

75% H_2SO_4 droplets. A simple calculation will now persuade us that the time required for this chemical scheme to absorb 100 ppm H_2O is far too long to confirm the observations. The production rate for SO_3 at noon equatorial conditions is 4.4×10^{13} molec cm^{-2} s^{-1} (Krasnopolsky, 1986) and as 100 ppm of water vapour is equivalent to $\sim1.5\times10^{20}$ molec cm^{-2}, it will take about 150 days to completely deplete it. Another possible sink of water vapour is its direct condensation onto existing H_2SO_4 droplets. This is an almost instantaneous process, with respect to the timescales considered, that decreases the sulphuric acid particles' acidity and size. However, we have performed basic numerical calculations based on the one-dimensional models developed by Irwin and Taylor (1996). These irrevocably showed that, after an initial sharp decline in the amount of free water vapour (of the order of a few pr μm) and the re-equilibration of the Venus cloud system, no great amounts of water vapour can be lost due to this process, and photolysis soon takes over as the dominant depletion mechanism.

Hence, unless there exists a more important chemical scheme inside the cloud region that depletes H_2O fast, chemistry alone cannot be expected to explain the *PV OIR* observations. In the following section, we revisit Venus' cloud and, through a composite figure, try and examine the second possible idea for the water vapour disappearance.

6.4 Venus' cloud revisited

In order to fully investigate the relative balance between water vapour and cloud characteristics, the combined observations of water vapour and cloud-top pressure from both instruments will be discussed qualitatively. To aid this endeavour, figures 6.1 and 6.2 were created. The cloud-top pressure and water vapour retrieved results from both satellites are shown on the same scale. The blue markers are the *PV OIR* observations and the red markers the *Venera 15* observations.

In figure 6.1, the difference between the behaviour of the cloud-top pressure in the two observational data sets is evident. Starting with the *Venera 15* cloud (red colour); it shows a decreasing trend from the late afternoon/early evening region (320° to 240°E) through the night (not covered) towards the morning terminator (90°E). Even though the large error bars prohibit a clear statement to be made, the *Venera 15* water vapour (red colour) is simultaneously low in the evening terminator region (320° to 240°E) during which time the cloud-top pressure reaches maximum value and slightly higher in the morning terminator region during cloud-top pressure minimum (figure 6.2.) This observation seems to conflict with the tentative assumption that if the cloud-top pressure decreases, water vapour will be "shielded" from view due to the cloud hiding it. The change of cloud-top pressure indicates a change in the mass loading of the atmosphere due to cloud droplets. The mass loading changes can be attributed to more reasons other than the condensation of free water vapour in the atmosphere. Krasnopolsky and Pollack (1984) quote in their conclusions that "a strong gradient of the H_2SO_4 vapour mixing

ratio near the bottom of the cloud layer drives a large upward flux of H_2SO_4 which condenses and forms the excess downward flux of liquid sulphuric acid." So, the *Venera 15* cloud-top pressure observations may even prove to be indirect evidence for a H_2SO_4 "rainfall".

A different picture emanates from the *PV OIR* observations, as seen in the two composite figures 6.1 and 6.2. A more steady cloud-top pressure in the daytime (90° to 300°E) with the nighttime decrease around the evening terminator, which is coupled with the lowest fractional scale heights. This indicates, as in the *Venera 15* results, that the composition of the cloud may have changed during the Venus day in accordance with the unit optical depth region. With respect to the water vapour abundance, a different perspective would be to note that there exists a background value of 20-40 ppm with localised enhancements of up to 100 ppm in the equatorial day-side. One might hence postulate that during the *PV OIR* visit, an upwelling of water vapour from lower cloud layers was observed, whereas during the *Venera 15* visit Venus' middle atmosphere reverted back to typical water vapour abundances with the cloud showing distinct features.

Even though the Pioneer Venus and Venera era observations pointed to a horizontally stratified and well-defined cloud region, the *PV OIR* and *Venera 15* experimental results do show inhomogeneities in the cloud's temporal and spatial structure. Fresh remote sensing observations, coupled with a full scale photochemical and dynamical model, will provide in the future the answers to the interesting questions posed in this chapter.

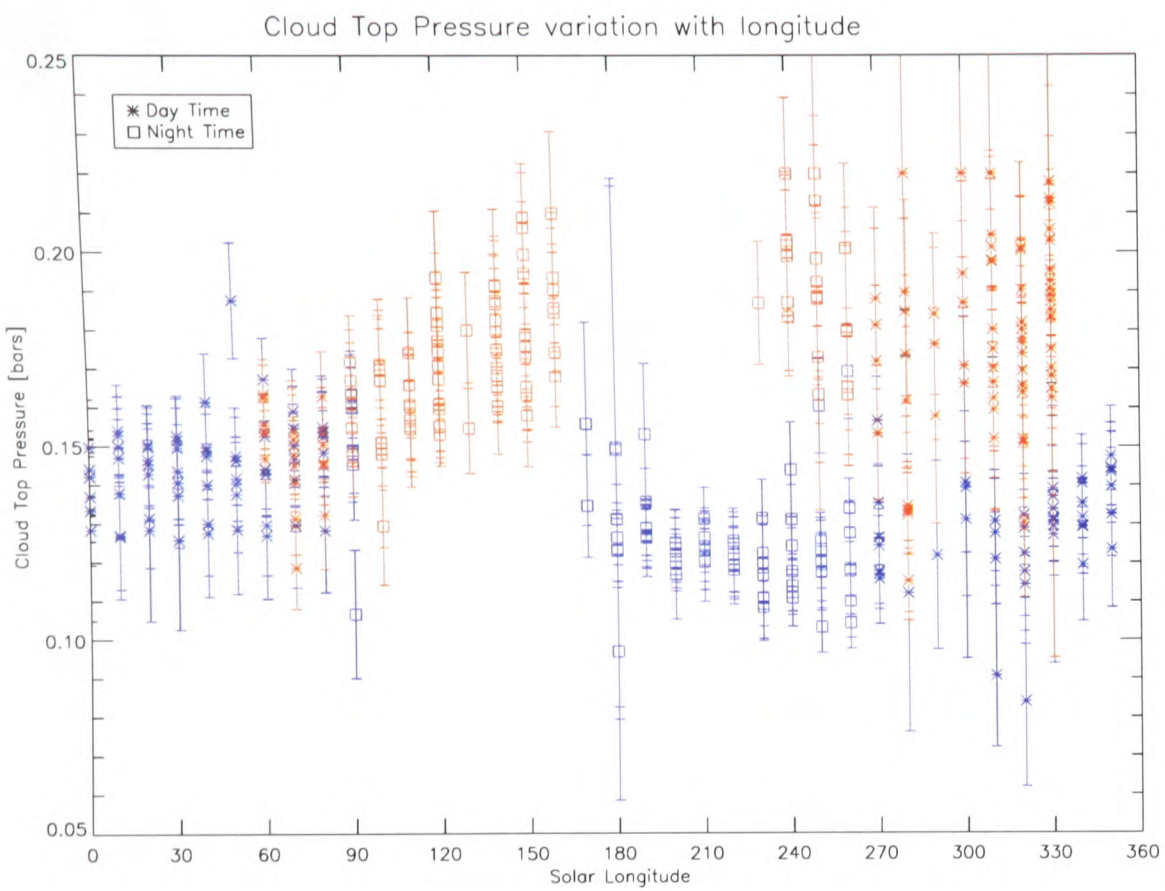

Figure 6.1: *PV OIR* and *Venera 15* cloud-top pressure variation with longitude. The blue markers are the *PV OIR* results and the red markers the *Venera 15* results.

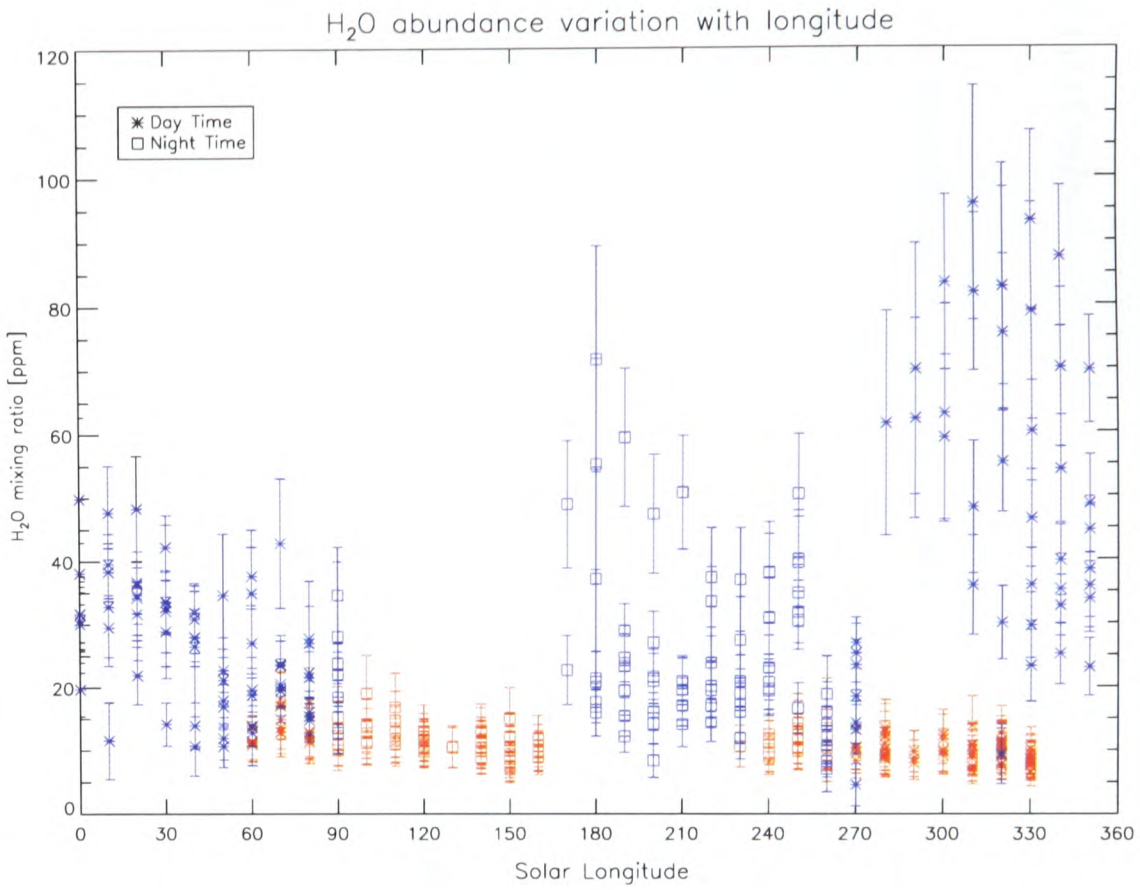

Figure 6.2: *PV OIR* and *Venera 15* water vapour abundance variation with longitude. The blue markers are the *PV OIR* results and the red markers the *Venera 15* results.

6.5 Synopsis

In this chapter, the following physical explanations were developed and qualitatively discussed; H_2SO_4 vapour dissociates in the lower Venus cloud, around 38-40 km, and H_2O and SO_2 are produced. These may be uplifted to the upper Venus cloud region via the convective region centred at 50-55 km and small-scale turbulence in the middle cloud region, possibly creating a short-lived water vapour enhancement. H_2SO_4 droplets form in a well-defined thin layer at the cloud-top, around 60 km, destroying both H_2O and SO_2, but not in the rates required to explain the sharp disappearance of ~50-60 ppm water vapour in the early evening Venus middle atmosphere observed by *PV OIR* . On the contrary, the cloud-top pressure exhibited a well-defined structure during the *Venera 15* encounter, coupled with low background H_2O abundances. We can only conclude that the H_2SO_4 cloud in Venus' middle atmosphere, irrespective of its omnipresence, shows temporal and spatial variations that remote sensing instruments are sensitive to. The findings of the Near Infrared Mapping Spectrometer, NIMS, which observed the 2.3 μm spectral window during the Galileo fly-by (Carlson et al., 1991), indeed revealed that the clouds of Venus are highly horizontally, as well as vertically, inhomogeneous. The origin of the contrasts is probably due to variable condensation of cloud material in large-scale cumulus-type dynamics in the deep atmosphere of Venus (Taylor, 2002). Hence, a high spectral, and mainly altitude, resolution instrument that would cover globally the equatorial and mid-latitudes regions might provide the comprehensive information required to understand the physics at work inside the H_2SO_4 cloud.

With respect to the photochemical model, the Venus cloud region chemistry is too complicated for one dimensional models to be able to encompass all the photochemically active processes, even though earnest efforts have been made in the past, e.g. by Winick and Stewart (1980) and Yung and DeMore (1982). The Winick and Stewart (1980) model focused on explaining the SO_2 observations made by the Pioneer Venus instruments and kept the water vapour profile fixed at 1 ppm. They note that since they do not include heterogeneous processes in their model, such as H_2SO_4 droplets creation, a fixed 1 ppm of H_2O will cause little error since H_2O interacts slowly with other species. The Yung and DeMore (1982) model also assumes an upper limit of 1 ppm for H_2O for the entire stratospheric region between 58 and 110 km. Both these models are one-dimensional and hence, even if they did focus on the H_2O chemistry, would not have provided us with the latitude/longitude predictions for H_2O required to explain the observations. The Krasnopolsky and Pollack (1984) model, much discussed throughout this chapter, highlighted that small deviations in water vapour abundance are sufficient for a complete discrepancy with experimental data. A two-dimensional chemistry model with a lower boundary at the bottom cloud levels, around 45 km, with small-scale dynamical activity incorporated, would complement nicely any satellite UV or infrared remote sensing observations of the middle Venus atmosphere.

Chapter 7

Conclusions

In the beginning of this chapter, the basic aims of the thesis and the associated results are summarised followed by a brief discussion on the main limitations encountered during the course of this work. At the end, future exploration plans and how they will further address the mystery of the Venus cloud-water system are briefly touched upon.

7.1 Synopsis

The main aim of this thesis was to reconcile the differences between the previous results of the *PV OIR* and *Venera 15* FTS experiments, through a common retrieval of the observations. An equally important aim was to validate the presence of a local water vapour enhancement in the equatorial region observed during the *PV OIR* mission.

Both these aims have been achieved through the development and use of a new

forward model that utilises the correlated-k treatment for calculating the absorption coefficients of the infrared gases active in Venus' middle atmosphere. The extinction coefficients that characterise the contribution of the H_2SO_4 cloud to the observed radiation were calculated anew using up-to-date refractive index data, where available. For the regions of no availability of new refractive indices, correction coefficients were successfully retrieved. Associated with the new forward model, a modern optimal estimation retrieval technique was employed in order to optimise the treatment of measurement and retrieval errors.

The work presented in this thesis verifies the results that previous, separate analyses had reached, i.e. the works of Schofield et al. (1983) and Ignatiev et al. (1999), which have been amply discussed in the text. The differences between the original results can now be attributed to different conditions in Venus' middle atmosphere during the length of the two missions. We discussed in section 3.3 that the general features of Venus' atmosphere, e.g. isothermal low and middle latitudes, strong constant super-rotational winds, omnipresent sulphuric acid clouds, etc., are expected to remain stable during the visits of the two spacecraft. However, annual fluctuations in particular aspects of the Venus atmosphere have long been established, e.g. the decline in the cloud-top abundance of SO_2 between 1978 and 1986 reported by Esposito et al. (1988). Furthermore, in chapter 2 we have seen that diurnal, temporal and local variations of water vapour abundance have also been reported in literature. Hence, the results of chapter 5 should not surprise us. We are confident that the presented work has completed a full cycle of analysis on

the *PV OIR* and *Venera 15* observations.

The main features of Venus' middle atmosphere revealed by the common analysis of the *PV OIR* and *Venera 15* observations are as follows; the *temperature structure*, as seen by both instruments, was found to be almost isothermal with variations of 5-10 K. The *cloud-top pressure* has a minimum of ~110±10 mbars in the evening equatorial region and a maximum of ~160±12 mbars in the morning mid-latitude regions in the *PV OIR* data. In the *Venera 15* observations, the cloud-top pressure increases steadily after the morning terminator from ~120±10 to 200±30 mbars in the late afternoon/early evening region. The day-night variation in *water vapour abundances* seen by the *PV OIR* instrument was found to fluctuate from 10±5 ppm at night up to 85-95±15 ppm in the equatorial region right after the sub-solar point, the wet spot region. The mean *Venera 15* water vapour abundances were found to be of the order of 12±5 ppm with no clear day-night distinction.

7.2 Limitations

The main limitation of any remote sounding radiative transfer study is the uncertainty on the physical information required in order to describe the observed atmosphere. Even though our general knowledge of the middle atmosphere of Venus is quite impressive, numerous details are still not available.

The key drawback for this analysis, in both *PV OIR* and *Venera 15* observations, was the insufficient knowledge of the optical property characteristics of the H_2SO_4 aerosol in the longer wavelengths, around the 45 μm fundamental water

vapour absorption band. Compensating measures were adopted both in this work and the previous ones, by Schofield et al. (1983) and Ignatiev et al. (1999). This specific uncertainty (an estimate of 10% on the absorption coefficient is given in Jones (1976)) precluded more accurate investigations into the H_2SO_4 cloud, e.g. changes in the acidity of the droplets (% of H_2SO_4), changes in the mean droplet radius, multi-modal clouds (more than one cloud distributions contributing to the observed radiance), impurities within the cloud aerosol particles, etc. Without precise optical properties it would be unreasonable to expect to retrieve such cloud features in great detail from the *PV OIR* and *Venera 15* observational data.

7.3 The Future

Even though traditionally this section is reserved for suggestions on follow-up work to the presented thesis, we believe that twenty years of analysis of the *PV OIR* and *Venera 15* data have exhausted most possibilities of novel approaches. Apart from a re-analysis using new H_2SO_4 cloud optical properties data at long infrared wavelengths, if and when those become available, there would appear to be little more that can done with the existing data to address the question of water vapour in the middle atmosphere of Venus. However, after working with these two datasets for the past three years, a few recommendations can be made regarding specific requirements of future remote sensing experiments studying Venus' middle atmosphere.

In order to understand the cloud system, we believe that a high spacial ($\sim$1 km) and spectral resolution nadir-viewing infrared spectrometer is paramount. In view of

the narrow photochemical destruction and creation layers and the inhomogeneity of the Venus main cloud deck, a 1-kilometre altitude resolution would also be important for the 40 to 65 km altitude region. This resolution could be attained by a limb-viewing spectrometer. Simultaneous observations via an ultraviolet spectrometer would enable the precise classification in terms of size, acidity and distribution of the Venus aerosol droplets. Hence, the combined radiative transfer analysis from these simultaneous observations of the Venus middle atmosphere would provide the necessary understanding of the fascinating Venus cloud system and permit the confident retrieval of water vapour abundance.

The proposed European Space Agency *Venus Express* mission will carry a number of instruments to explore Venus' atmosphere and surface geology from orbit. Among them, a high resolution IR Fourier spectrometer, a UV and IR spectrometer for solar occultation and nadir observations and a UV-visible-near IR imaging spectrometer are bound to shed light on the fascinating and important question of water vapour in Venus' middle atmosphere.

Appendix A

A priori Information

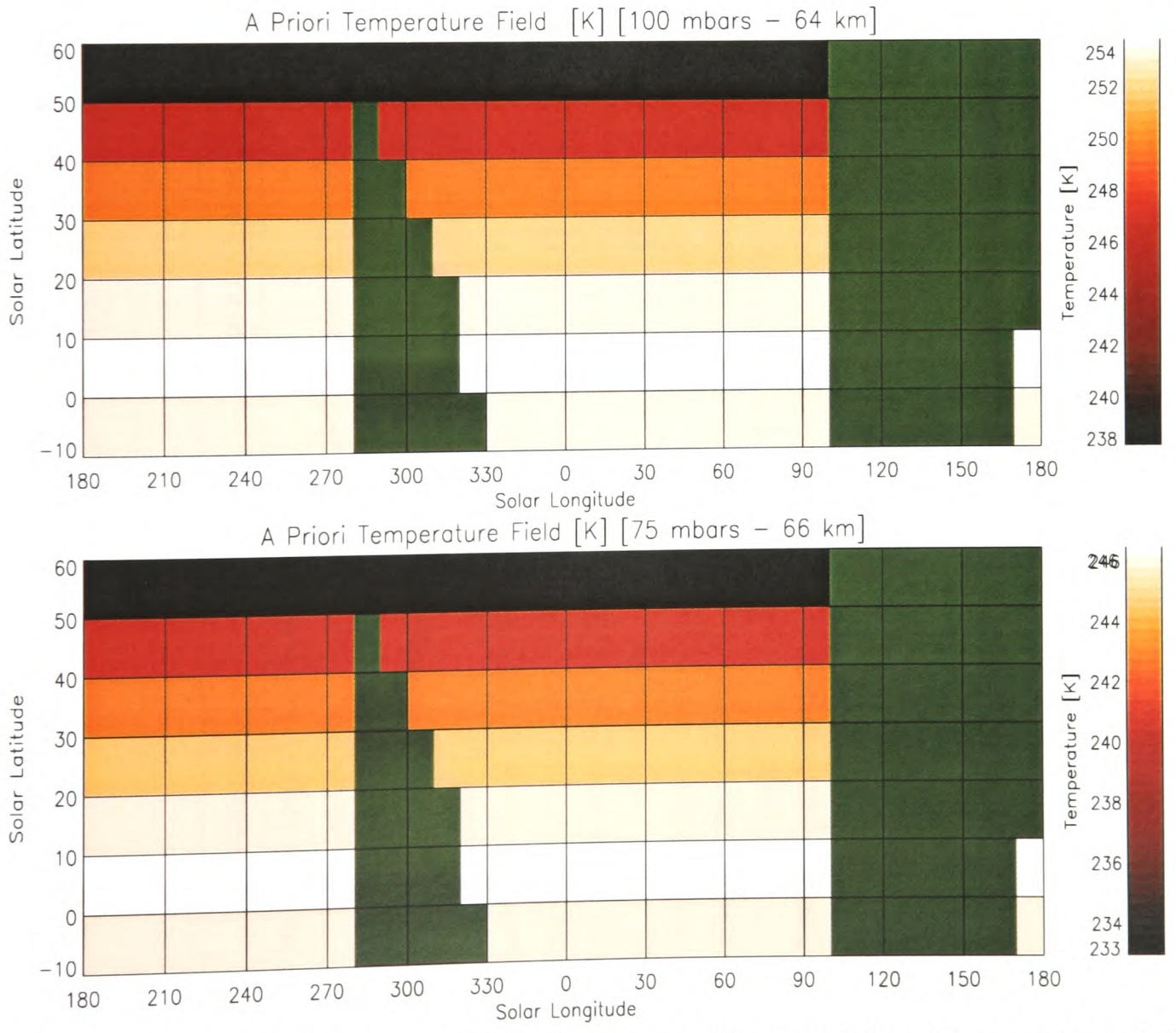

Figure A.1: A priori temperature field corresponding to retrieved temperature field shown in figures 5.1 and 5.9.

Parameter	A priori value	Reference
Forward model input information		
Temperature	See figures 4.1 and A.1	Seiff et al. (1980); Kliore and Patel (1982)
Pressure profile	See figure 4.1	
Absorber amount profiles	See figure 4.2	
Line data base	*Hitran* 96	Rothman et al. (1998)
Retrieval *a priori* information		
cp0, unit cloud optical depth	120±40 mbars	Marov et al. (1980); Esposito et al. (1983)
hc, cloud fractional scale height	1.0±0.2	
f_{H_2O}, H_2O abundance	30±10 ppm	See figure 2.1
Temperature error	5 K	
Correlation length	10 km	
ϕ limit	0.1	
Cloud properties		
Mean radius and variance	1.05 μm, 0.07	Hansen and Honevier (1974)
Distribution	Log-normal	Knollenberg and Hunten (1980)
Optical properties		Jones (1976); Biermann et al. (2000)
Optical depth ratios	r58 = 0.3433, r54 = 2.1765	

Table A.1: A priori values for all parameters required for the nominal forward model calculations and retrievals.

[redacted]

Table A.2: Water vapour mixing ratios [ppm] observed by *Venera 11* (Young et al., 1984).

A.1 The importance of *a priori* information revealed

The nature of remote sounding poses a few constraints on the analysis of the measurements obtained. The main one is that sensible *a priori* knowledge of the observable system is required in order to acquire the information that the remote sensing measurements have to offer. Two examples are presented below for information purposes.

The Venera 11 0.7 to 1.2 μm spectra were re-analysed by Young et al. (1984) following up the work of Moroz et al. (1979a). By calculating synthetic spectra, they tried to combine the existing models of Moroz et al. (1979b) with the measured spectra giving a profile for the water vapour mixing ratio as shown in Table A.2. Moroz et al. (1979a) and Moroz et al. (1979b) used a less detailed method of treating molecular absorptions, while laying emphasis on scattering. On the other hand, Young et al. (1984) paid particular attention to the molecular absorptions and conversely made only an approximate allowance for scattering. The difference between the predicted water vapour volume mixing ratio is staggering, not only in absoluter magnitude terms, but mostly in variation of the species with altitude. Moroz et al. (1979a) predict a significant enhancement in the main cloud region centred at 60 km, with decreasing abundance towards the surface, whereas Young et al. (1984) predict a water enhancement right under the main cloud deck with strong depletion inside the cloud region.

On a similar issue, Donahue and Hodges (1992) analysed in detail the Pioneer

Venus large-probe neutral mass spectrometer data and concluded that the abundance of Venus deuterium as being two orders of magnitude larger than that of terrestrial deuterium. They also report that the mixing ratio for water increases by a factor of four between 0 and 10 km to a value of *67 ppm* and drops to *10 ppm* above 50 km. In a later analysis, Donahue and Hodges (1993) report a microleak of gases in the experiment which has mislead them in the previous assessment that there exists a sharp near-surface gradient for H_2O and revise their value to *28 ppm* constant with altitude below 25 km.

Both these examples have rendered us very careful when constructing the mathematical and computational formalism that would permit us to analyse the *PV OIR* and *Venera 15* data. Numerous tests have been performed at each stage of the retrieval process in order to verify the validity of particular choices made. Most of these are discussed in the main text of this thesis.

Appendix B

Radiative Transfer and Retrieval Equations

B.1 Levenberg-Marquard Method

Levenberg (1944) proposed the following iterative method:

$$x_{i+1} = x_i + (\mathcal{K}\mathcal{K}^T + \lambda_i\, I)^{-1}\mathcal{K}^T\,(y - y_n) \tag{B.1}$$

where, λ_i is chosen in each step to minimise the cost function, ϕ.

- If $\lambda_i \to 0$ the step tends to Gauss-Newton's method.

- If $\lambda_i \to \infty$ the step tends to the steepest descent but the step size tends to zero.

This method is computationally expensive since y_n has to be evaluated at each iteration. Marquardt (1963) simplified it by not trying to find the best λ_i at each iteration but starting a new step as soon as a value that minimises ϕ is found. An arbitrary λ_i is initially used. Press et al. (1995) further simplified the Marquardt-Levenberg idea as follows:

- If ϕ increases, increase λ_i, do not update x_i and try again.
- If ϕ decreases, decrease λ_i, update x_i and move to the next step.

The factor by which λ is increased or decreased is a matter of experimenting in each particular case. Marquardt (1963) suggested a factor of ten either way. Fletcher (1971) proposed a factor of two for reducing λ and a factor between 2 and 10 for increasing it. In this work, we have arbitrarily chosen to decrease λ by 0.3 and increased it by 10.

B.2 Different retrieval methods

The analysis performed by Schofield and Taylor (1982), Ignatiev et al. (1997) and this work aspire to the same thing, namely the inversion of the measured radiances to temperature, cloud and water vapour abundance profiles. However, three different mathematical retrieval techniques were used to achieve this goal and we deem it important to at least mention them and discuss their subtle but possibly important differences.

The Statistical Regularisation

In the work of Ignatiev et al. (1999) , the formalism of Ustinov (1991), known in Russian literature as "the statistical Regularisation", was used to solve the inverse problem. This technique is based on the idea of using *a priori* information in order to regularise the solution of the inverse problem, very similar to the Rodgers (1976) technique. Both fall under the "linear relaxation" school of techniques for solving equation 4.1. However, Ignatiev et al. (1999) have used a slightly different iterative equation in lieu of equation 4.26.

Replacing x_o by x_i, the iteration reduces to:

$$x_{i+1} = x_i + (S_a^{-1} + \mathcal{K}_i^T\ S_\epsilon^{-1}\ \mathcal{K}_i)^{-1}\mathcal{K}_i^T\ S_\epsilon^{-1}\{(y - F(x_i)) - \mathcal{K}_i(x_i - x_i)\}$$
$$= x_i + G_i\ [y - F(x_i)] \tag{B.2}$$

where, $G_i = (S_a^{-1} + \mathcal{K}_i^T\ S_\epsilon^{-1}\ \mathcal{K}_i)^{-1}\mathcal{K}_i^T\ S_\epsilon^{-1}$.

If this equation converges, the solution will satisfy:

$$\hat{x} = \hat{x} + G_i\ [y - F(x_i)] \tag{B.3}$$

which is clearly a non-optimal "exact" solution, for which $y = F(x_i)$.

Non-linear Relaxation Methods

In Schofield and Taylor (1982) and Schofield et al. (1983) a non-linear relaxation technique was used based on the Twomey-Chahine Method (e.g. Twomey et al. (1977), Chahine (1972), Smith (1970)). The temperature and two-parameter cloud model are retrieved using first-guess models and a sophisticated iterative and relaxation technique, briefly reproduced below.

A two dimensional iteration for unit cloud optical depth, cp0, and fractional scale height, hc, was used to find the optimum cloud model and temperature profile by minimising the weighted residual:

$$R(cp0, hc) = \frac{\sum\ (y - y_i)(S_\epsilon^{-1})^2}{\sum(S_\epsilon^{-1})^2} \tag{B.4}$$

where, $R(cp0, hc)$ is the weighted residual to be minimised, y is the measured radiance, y_n is the forward modelled radiance and S_ϵ is the measurement error. The iterative process had to manually be stopped after a specified number of relaxations as convergence was being reached. The nature of the relaxation scheme shown in equations B.5 made the shape of the retrieved profile dependent on the first-guess

profile and the shape of the weighting functions[1]. A very similar relaxation scheme was developed for the water vapour abundance retrievals, which were performed as a separate second step using as input the already retrieved cloud structure and temperature profile.

$$T_{n+1} = T_n F_{1,n} \tag{B.5}$$

$$F_{1,n} = \frac{\sum(S_\epsilon \, W \, F_{2,n})}{\sum(S_\epsilon \, W)} \tag{B.6}$$

$$F_{2,n} = \frac{B^{-1}_{\tilde{\nu_0}}(y)}{B^{-1}_{\tilde{\nu_0}}(y_n)} \tag{B.7}$$

where, W are the weighting functions and $B^{-1}_{\tilde{\nu_0}}$ is the inverse Planck function calculated for the measured and modelled radiances.

[1]By analogy, the nature of our retrieval scheme explained in section 4.4 makes the retrieved profile dependent on the *a priori* profile and on the averaging kernel, $\mathcal{K}$-matrix.

Appendix C

Line Strengths

In this section, the line strengths (S in equation 4.11) for the radiatively active species in the infrared region of interest are shown in the four following figures. These line strengths are derived from the *Hitran* 96 spectroscopic data base (Rothman et al., 1998). Note that the best indicator for the relative importance of each species is comparing the line strengths directly.

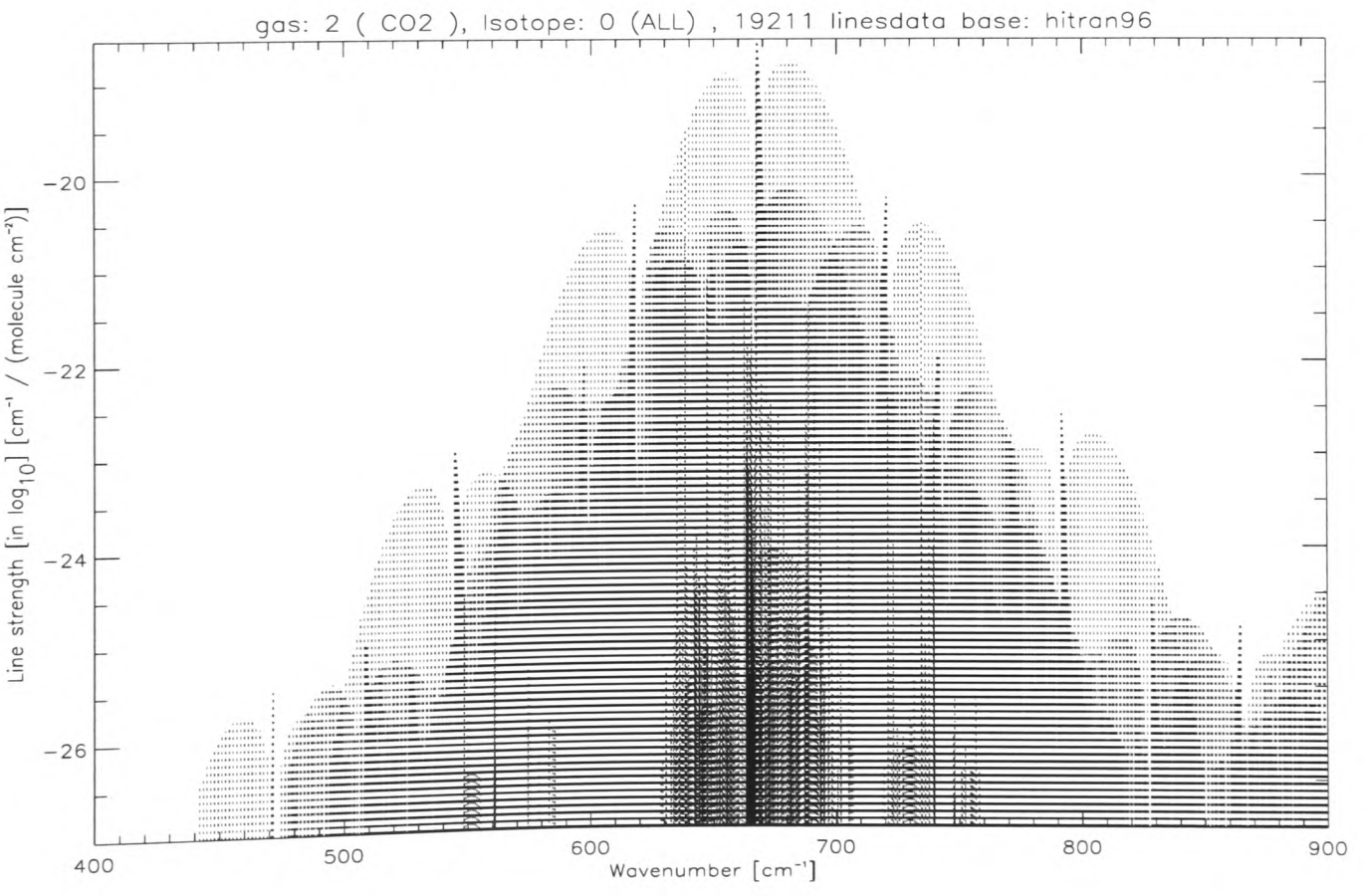

Figure C.1: CO_2 line strengths in cm^{-1}/molecule cm^{-2}.

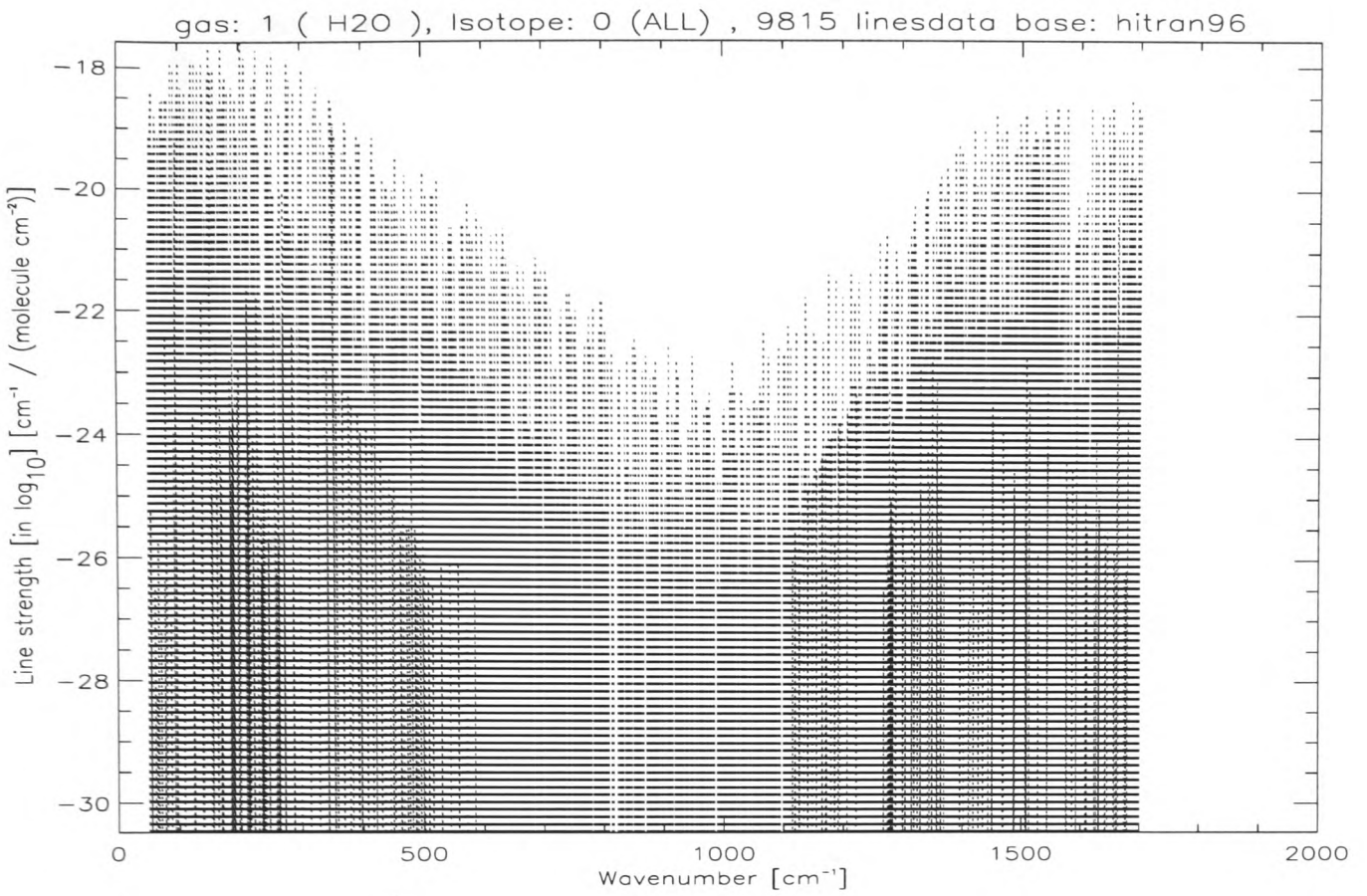

Figure C.2: H_2O line strengths in cm^{-1}/molecule cm^{-2}.

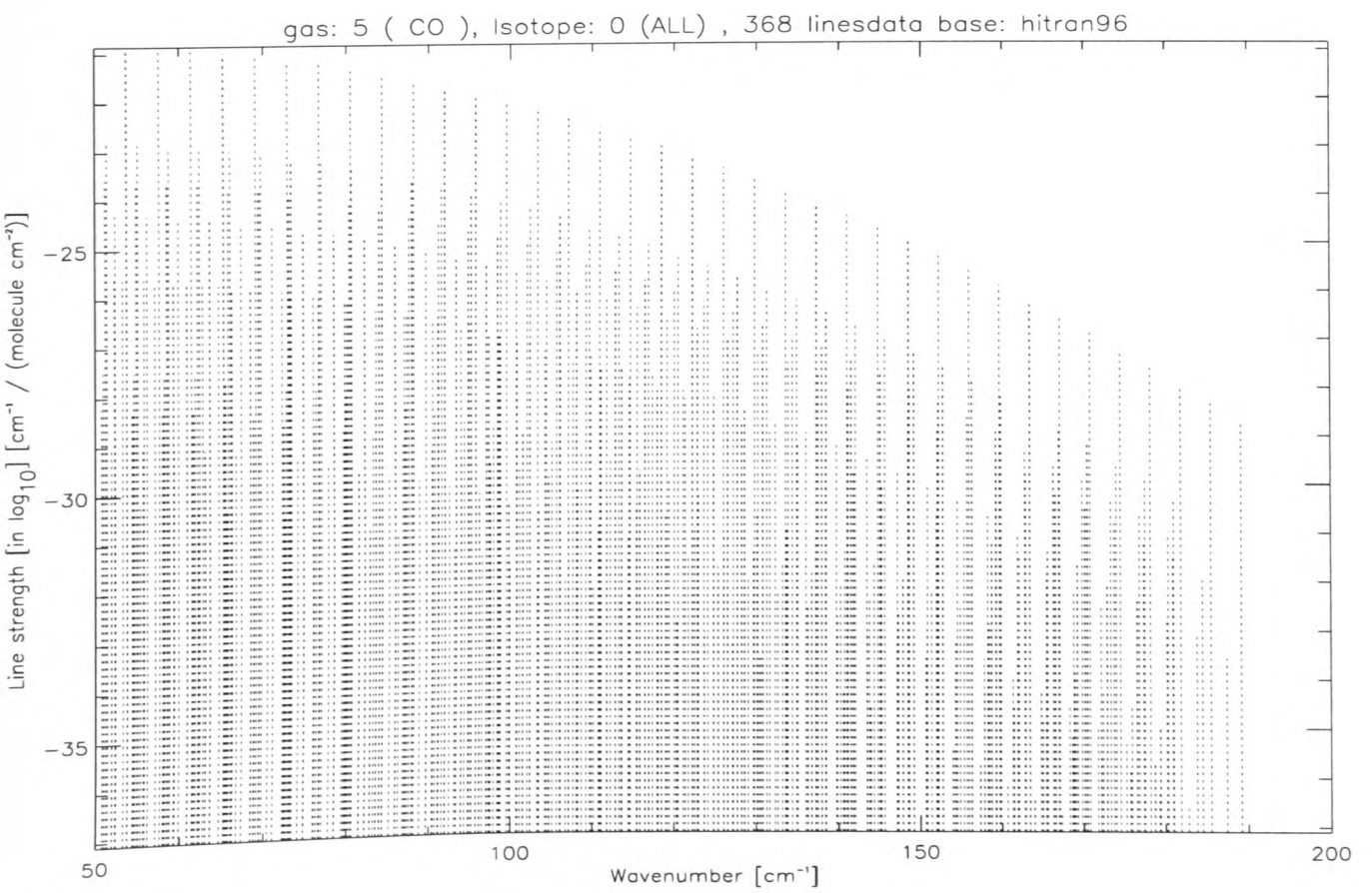

Figure C.3: CO line strengths in cm^{-1}/molecule cm^{-2}.

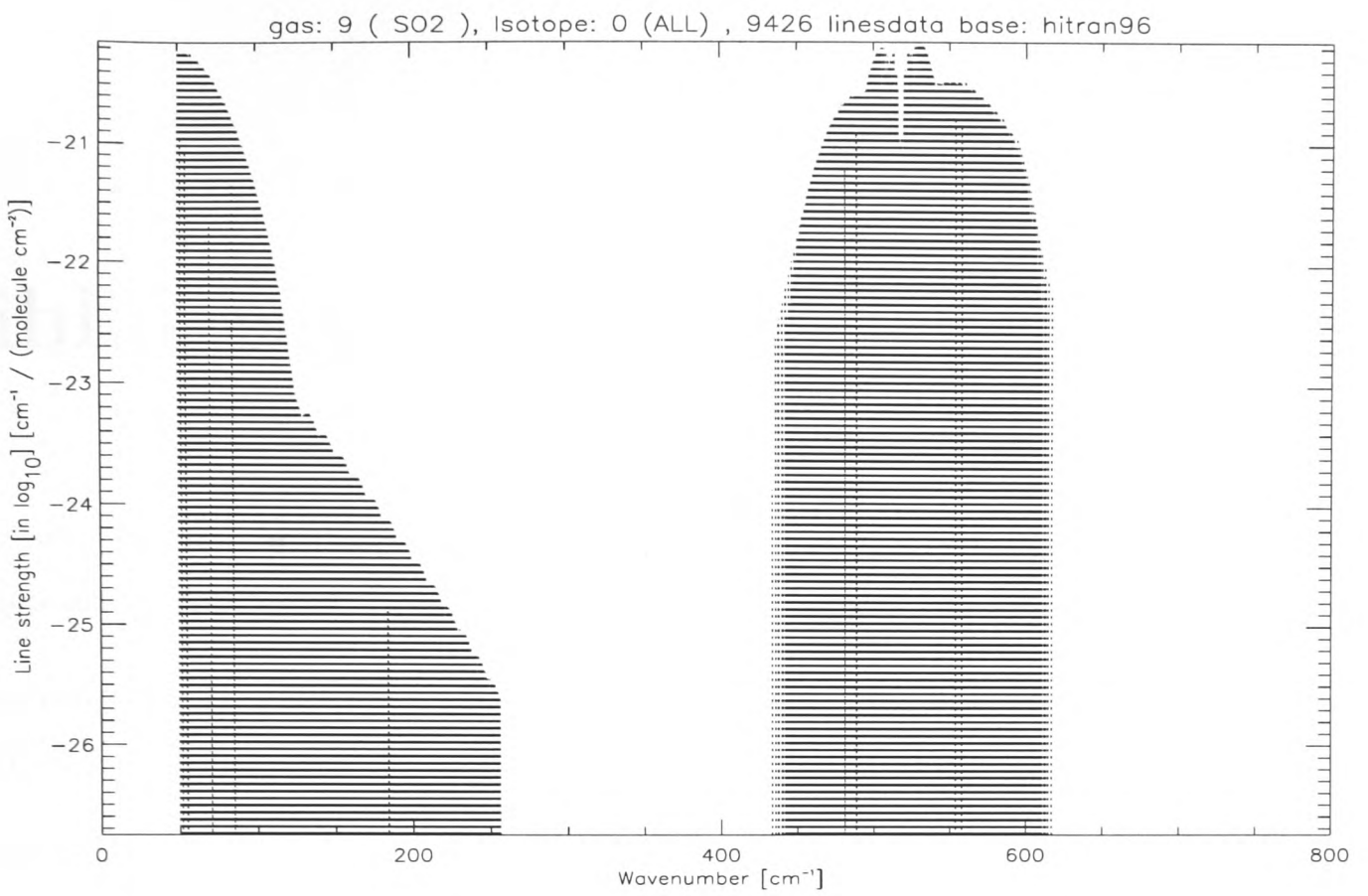

Figure C.4: SO_2 line strengths in cm^{-1}/molecule cm^{-2}.

Bibliography

Andrews, D. A., Holton, J. R., and Leovy, C. B. (1987). *Middle Atmosphere Dynamics*. Academic Press.

Armstrong, B. H. (1967). Spectrum line profiles: The Voigt function. *J.Q.S.R.T.*, 7:66–88.

Aumann, H. H. and Orton, G. S. (1979). The 12 to 20 micron spectrum of Venus: Implications for temperatures and cloud structure. *Icarus*, 38:251–266.

Barker, E. S. (1975a). Comparison of Simultaneous CO_2 and H_2O observations of Venus. *J. Atmos. Sci.*, 32:1071–1075.

Barker, E. S. (1975b). Observations of Venus Water Vapour over the Disk of Venus: The 1972-1974 data using the H_2O lines at 819.7 and 817.6 nm. *Iracus*, 25:268–281.

Bayers, R. M. (1763). An Essay towards solving a problem in the Doctrine of Chances. *Phil. Trans. R. Soc. Lond.*, 53:370.

Bell III, J. F., Crisp, D., Lucey, P. G., Ozoroski, T. A., Sinton, W. M., Willis, S. C., and Campbell, B. A. (1991). Spectroscopic Observations of Bright and Dark Emission Features on the Night Side of Venus. *Science*, 252:1293–1296.

Belton, M. J. S., Gierasch, P. J., Smith, M. D., and collaborators. (1991). Images from Galileo of the Venus cloud deck. *Science*, 253(5027):1531–1536.

Belton, M. J. S., Hunten, D. M., and Goody, R. M. (1968). Quantitative spectroscopy of Venus in the region 800-1100 nm. In Brandt, J. C. and McElroy, M. B., editors, *The Atmospheres of Venus and Mars*, pages 69–98. New York:Gordon and Breach.

Bertaux, J. L., Widemann, T., Hauchecorne, A., I., M. V., and Economov, A. P. (1996). Vega 1 and Vega 2 entry probes: an investigation of local UV absorption

220-440 nm in the atmosphere of Venus (SO_2, aerosols, cloud structure). *J. Geophys. Res.*, 101(E5):12709–12745.

Bézard, B., de Bergh, C., Crisp, D., and Maillard, J. (1990). The deep atmosphere of Venus revealed by high-resolution night side spectra. *Nature*, 345:508–511.

Bézard, B., de Bergh, C., Maillard, J. P., Crisp, D., Owen, T., Pollack, J. B., and Grinspoon, D. (1993). The abundance of sulphur dioxide below the clouds of Venus. *Geophys. Res. Let.*, 20:1587–1590.

Biermann, U., Luo, B. P., and Peter, T. (2000). Absorption Spectra and Optical Constants of Binary and Ternary Solutions of H_2SO_4, HNO_3 and H_2O in the mid-infrared at atmospheric temperatures. *J. Phys. Chem. A.*, 104:783–793.

Blamont, J. E., Young, R. E., Seiff, A., Ragen, B., Sagdeev, R., Linkin, V. M., Kerzhanovich, V. V., Ingersoll, A. P., Crisp, D., Elson, L. S., Preson, R. A., Golistyn, G. S., and Ivanov, V. N. (1986). Implications of the Vega balloon results for Venus atmospheric dynamics. *Science*, 231(4744):1422–1425.

Bottema, M., Plummer, W., and Strong, J. (1964). Water vapour in the atmosphere of Venus. *The Astrophysical Journal*, 139(3):1021–1022.

Bougher, S. W., Dickinson, R. E., Ridley, E. C., and Roble, R. G. (1988). Venus mesosphere and thermosphere III. Three-dimensional general circulation with coupled dynamics and composition. *Icarus*, 73:545–573.

Bougher, S. W. and Roble, R. G. (1991). Comparative terrestrial planet thermospheres. 1. Solar cycle variation of global mean temperatures. *J. Geophys. Res.*, 96:11045–11055.

Bullock, M. A. and Grinspoon, D. H. (2001). The recent evolution of climate on Venus. *Icarus*, 150:19–37.

Carlson, R. W., Kamp, L. W., Baines, K. H., Pollack, J. B., Grinspoon, D. H., Encrenaz, T., Drossart, P., and Taylor, F. W. (1991). Variations in Venus cloud particle properties: a new view of Venus' cloud morphology as observed by the Galileo Near-Infrared Mapping Spectrometer. *Planet. Space Sci.*, 41(7):477–485.

Chahine, M. T. (1970). Inverse problems in Radiative Transfer: Determination of Atmospheric Parameters. *J. Atmos. Sci.*, 27:960–967.

Chahine, M. T. (1972). A general relaxation method for Inverse Solution of the Full Radiative Transfer Equation. *J. Atmos. Sci.*, 29:741–747.

Chahine, M. T. (1974). Remote Sounding of Cloudy Atmospheres. I. The Single Cloud Layer. *J. Atmos. Sci.*, 31:233–243.

Chamberlain, J. W. and Hunten, D. M. (1987). *Theory of Planetary Atmospheres.* Academic Press.

Clough, S. A., Kneizys, F. X., and Davies, R. W. (1989). Line shape and the water vapour continuum. *Atmospheric Research*, 23:229–241.

Clough, S. A., Kneizys, F. X., Davies, R. W., Gamache, R. R., and Tipping, R. (1980). Theoretical line shape for H_2O vapour: Application to the continuum. In Deepak, A., Wilkerson, T. D., and Ruhnke, L. H., editors, *Atmospheric Water Vapour*, pages 25–46. Academic Press, New York.

Colin, L. (1980). The Pioneer Venus Program. *J. Geophys. Res.*, 85(A13):7575–7598.

Collard, A. D., Taylor, F. W., Calcutt, S. B., Carlson, R. W., Kamp, L. W., Baines, K. H., Encrenaz, T., Drossart, P., Lellouch, E., and Bézard, B. (1993). Latitudinal distribution of carbon monoxide in the deep atmosphere of Venus. *Planet. Space. Sci.*, 41(7):487–494.

Connes, J. and Connes, P. (1966). Near-infrared planetary spectra by Fourier Spectroscopy. I. Instruments and results. *J. Opt. Soc. Amer.*, 56:869–910.

Cousin, C., Le Doucen, R., Boulet, C., and Henry, A. (1985). Temperature dependence of the absorption in the region beyond the 4.3 μm band head of CO_2. 2: N_2 and O_2 broadening. *Applied Optics*, 24(22):3899–3907.

Crisp, D. (1986a). Radiative Forcing of the Venus Mesosphere I. Solar Fluxes and Heating Rates. *Icarus*, 67:484–514.

Crisp, D. (1986b). Radiative Forcing of the Venus Mesosphere II. Thermal Fluxes, Cooling Rates and Radiative Equilibrium Temperatures. *Icarus*, 77:391–413.

Crisp, D., Allen, D., Grinspoon, D., and Pollack, J. (1991a). The dark side of Venus: Near-Infrared Images and Spectra from the Anglo-Australian Observatory. *Science*, 253:1263–1266.

Crisp, D., McMuldroch, S., Stephens, S. K., Sinton, W. M., Ragent, B., Hodapp, K. W., Probst, R. G., Doyle, L. R., Allen, D. A., and Elias, J. (1991b). Ground-based near-infrared imaging observations of Venus during the Galileo encounter. *Science*, 253(5027):1538–1541.

Dave, J. V. (1969). Scattering of electromagnetic radiation by a large, absorbing sphere. *IBM J. Res. Dev.*, 13(3):302–313.

de Bergh, C., Bézard, B., Crisp, D., Maillard, J., Owen, T., Pollack, J., and Grinspoon, D. (1995). Water in the deep atmosphere of Venus from the High-Resolution Spectra of the night side. *Adv. Space. Res.*, 15:(4)79–(4)88.

Del Genio, A. D. and Rossow, W. B. (1990). Planetary-scale waves and the cyclic nature of cloud top dynamics of Venus. *J. Atmos. Sci.*, 47:293–318.

Delderfield, J., Schofield, J. T., and Taylor, F. W. (1980). Radiometer for the Pioneer Venus Orbiter. In *IEEE Transactions on Geoscience and Remote Sensing*, volume 18, pages 70–76.

Donahue, T. M. and Hodges, R. R. (1992). Past and Present Water Budget on Venus. *J. Geophys. Res.*, 97:6093–6091.

Donahue, T. M. and Hodges, R. R. (1993). Venus Methane and Water. *Geophys. Res. Let.*, 20:591–594.

Drossart, P. Bézard, B., Encrenaz, T., Lellouch, E., Roos-Serote, M., Taylor, F. W., Collard, A., Grinspoon, D., Carlson, R., Baines, K., and Kamp, L. (1993). Search for spatial variations of the H_2O abundance in the lower atmosphere of Venus from NIMS-Galileo. *Plan. Space Sci.*, 41:495–504.

Encrenaz, T., Lellouch, E., Gernicharo, J., Paubert, G., Gulkis, S., and Spilker, T. (1995). The Thermal Profile and Water Abundance in the Venus Mesosphere from H_2O and HDO Millimetre Observations. *Icarus*, 117:162–172.

Encrenaz, T., Lellouch, E., Paubert, G., and Gulkis, S. (1991). First detection of HDO in the atmosphere of Venus at radio wavelengths: an estimate of the H_2O vertical distribution . *Astronomy and Astrophysics*, 246:63–66.

Esposito, L. W. Winick, J. R. and Stewart, A. I. (1979). Sulphur dioxide in the Venus atmosphere: Distribution and implications. *Geophys. Res. Let.*, 6:601–604.

Esposito, L. W., Copley, M., Eckert, R., Gates, L., Stewart, A. I. F., and Worden, H. (1988). Sulphur dioxide at the Venus cloud tops: 1978-1986. *J. Geophys. Res.*, 93:5267–5276.

Esposito, L. W., Knollenberg, R. G., Marov, M. Y., Toon, O. B., and P., T. R. (1983). *The clouds and hazes of Venus*, pages 215–279. Space Science Series. University of Arizona Press.

Fink, U., Larson, H. P., Kuiper, G. P., and Poppen, R. F. (1972). Water vapour in the atmosphere of Venus. *Icarus*, 17:617–631.

Fletcher, R. (1971). A modified Marquardt subroutine for nonlinear least squares fitting. Technical report, Report R6799, A.E.R.E., Harwell.

Gamache, R. R., Hawkins, R. L., and Rothman, L. S. (1990). Total internal partition sums in the temperature range 70-3000 K - Atmospheric linear molecules. *J. Molec. Spec.*, 142(2):205–219.

Gmitro, J. I. and Vermeulen, T. (1964). Vapour-liquid equilibria for aqueous Sulphuric Acid. *Am Inst Chem Eng*, 10:740–746.

Goody, R. M., West, R., Chen, L., and Crisp, D. (1989). The Correlated-k method for radiation calculations in non-homogeneous atmospheres. *J. Q. S. R. T*, 42:539–550.

Goody, R. M. and Yung, Y. L. (1989). *Atmospheric Radiation,Theoretical Basis.* Oxford University Press.

Grinspoon, D. H. (1987). Was Venus wet? Deuterium reconsidered. *Science*, 238:1702–1704.

Grinspoon, D. H. (1997). *Venus Revealed; A new look below the clouds of our mysterious twin planet.* Addison-Wesley.

Gull, T. R., O'Dell, C. R., and Parker, R. A. R. (1974). Water vapour in Venus determined by air born observations of the 0.82 μm band. *Icarus*, 21:213–218.

Hansen, J. E. and Honevier, J. W. (1974). Interpretation of the polarisation of Venus. *J. Atmos. Sci.*, 31:1137.

Hansen, J. E. and Travis, L. (1974). Light Scattering in Planetary Atmospheres. *Space Sci. Rev.*, 16:527–610.

Haus, R. and Titov, D. V. (2000). PFS on Mars Express: preparing the analysis of infrared spectra to be measured by the Planetary Fourier Spectrometer. *Plan. Space Sci.*, 48:1357–1376.

Heathfield, A. E., Newnham, D. A., Ballard, J., Grainger, R. G., and Lambert, A. (1999). Infrared and visible Fourier-transform spectra of sulphuric acid/water aerosols at 230 and 294 K. *Applied Optics*, 38(30):6408–6420.

Hilsenrath, J. (1960). *Tables of Thermodynamic and Transport Properties of Air, Argon, Carbon Dioxide, Carbon Monoxide, Hydrogen, Nitrogen, Oxygen and Steam.* Pergamon, New York.

Hoffman, J. H., Oyama, V. I., and von Zahn, U. (1983). Measurements of the Venus Lower Atmosphere Composition: A Comparison of Results. *Journal of Geophysical Research*, 85(A13):7871–7881.

Houghton, J. T. and Taylor, F. W. (1975). One remote sounding of the upper atmosphere of Venus. *J. Atmos. Sci.*, 32:620–629.

Houghton, J. T., Taylor, F. W., and Rodgers, C. D. (1984). *Remote Sounding of Atmospheres.* Cambridge University Press.

Humlicek, J. (1982). Optimised computation of the Voigt and complex probability functions. *J. Q. S. R. T.*, 27(4):437–44.

Ignatiev, N., Moroz, V. I., Moshkin, B., and collaborators. (1997). Water vapour in the lower atmosphere of Venus: a new analysis of optical spectra measured by entry probes. *Plan. Space Sci.*, 45:427–438.

Ignatiev, N., Moroz, V. I., Zasova, L., and Khatuntsev, I. (1999). Venera 15: Water vapour in the middle atmosphere of Venus. *Adv. Space Sci.*, 23(9):1549–1558.

Imamura, T. and Hashimoto, G. L. (1998). Venus cloud formation in the meridional circulation. *J. Geophys. Res.*, 103(E13):31349–31366.

Irwin, P. G. J. (1997). Temporal and Spatial variations in the Venus Mesosphere retrieved from Pioneer Venus OIR. *Adv. Space Res.*, 19:1169–1179.

Irwin, P. G. J., Calcutt, S. B., and Taylor, F. W. (1997). Radiative transfer models for Galileo NIMS studies of the atmosphere of Jupiter. *Adv. Space Sci*, 19(8):1149–1158.

Irwin, P. G. J. and Taylor, F. W. (1996). The diurnal variability of water vapour above the clouds of Venus. Unpublished manuscript.

James, E. P., Toon, O. B., and Schubert, G. (1997). A Numerical Microphysical Model of the Condensational Venus Cloud. *Icarus*, 129:147–171.

Janssen, M. A. and Klein, M. J. (1981). Constraints on the composition of the Venus atmosphere from Microwave Measurements near 1.35 cm wavelength. *Icarus*, 46:58–69.

Jenkins, J. M., Steffes, P. G., Hinson, D. P., Twicken, J. D., and Tyler, G. L. (1994). Radio occultation studies of the Venus atmosphere with the Magellan spacecraft. 2. Results from the October 1991 experiments. *Icarus*, 110:79–94.

Jones, A. (1976). Optical constants of Sulphuric Acid in the far Infrared. *J. Q. S. R. T.*, 16:1017–1019.

Kamp, L. W. and Taylor, F. W. (1990). Radiative Transfer models of the night side of Venus. *Icarus*, 86:510–529.

Keating, G., Nickolson, J., and Lake, L. (1980). Venus Upper Atmosphere Structure. *J. Geophys. Res.*, 85:7941–7956.

Kliore, A. J. and Patel, I. R. (1980). Thermal Structure of the Atmosphere of Venus from Pioneer Venus Radio Occultations. *J. Geophys. Res.*, 85:7957–7962.

Kliore, A. J. and Patel, I. R. (1982). Thermal Structure of the Atmosphere of Venus from Pioneer Venus Radio Occultations. *Icarus*, 52:320–334.

Knollenberg, R. G. and Hunten, D. M. (1980). The Microphysics of the Clouds of Venus: Results of the Pioneer Venus particle size spectrometer Experiment. *J. Geophys. Res.*, 85(A13):8039–8058.

Koukouli, M. E. (2001). Remote Sensing of Water Vapour in Venus' Middle Atmosphere. Second Year Report, *AOPP*, Oxford University.

Koukouli, M. E. (2002). *Remote sensing of water vapour in Venus' middle atmosphere*. PhD thesis, Atmospheric, Oceanic and Planetary Physics, Oxford University.

Krasnopolsky, V. A. (1986). *Photochemistry of the atmospheres of Mars and Venus*. Physics and Chemistry in Space. Springer-Verlag.

Krasnopolsky, V. A. and Parshev, V. A. (1983). Photochemistry of the Venus atmosphere. In Bougher, S. W., Hunten, D. M., and Phillips, R. J., editors, *Venus*, Space Science Series, pages 431–458. University of Arizona Press.

Krasnopolsky, V. A. and Pollack, J. B. (1984). H_2O -H_2SO_4 system in Venus' clouds and OCS , CO and H_2SO_4 profiles in Venus' troposphere. *Icarus*, 109:58–78.

Kuiper, G. P. and Forbes, F. F. (1967). High altitude spectra from NASA CV 990 Jet. I: Venus, 1 - 2.5 μm, resolution 20 cm^{-1}. *Comm. Lunar Planet. Lab.*, 6:177–189.

Kuiper, G. P., Forbes, F. F., Steinmetz, D. L., and Mitchelll, R. I. (1969). High altitude spectra from NASA CV 990 Jet. II: Water vapour on Venus. *Comm. Lunar Planet. Lab.*, 6:209–228.

Kurucz, R. L. (1991). *The Solar Spectrum, in the Solar Interior and Atmosphere, eds. A.N. Cox, W.C. Livingston, and M. Matthews.* Tucson, University of Arizona Press.

Lacis, A. A. and Oinas, V. (1991). A description of the Correlated-K Distribution Method for Modelling Non Gray gaseous Absorption, Thermal Emission and Multiple Scattering in Vertically Inhomogeneous Atmospheres. *J. Geophys. Res.*, 19:9027–9063.

Le Doucen, R., Cousin, C., Boulet, C., and Henry, A. (1985). Temperature dependence of the absorption in the region beyond the 4.3 μm band head of CO_2. 2: Pure CO_2 case. *Applied Optics*, 24(6):897–906.

Lellouch, E., Clancy, T., Crisp, D., Kliore, A. J., Titov, D., and Bougher, S. W. (1997). Monitoring of Mesospheric Structure and Dynamics. In Bougher, S. W., Hunten, D. M., and Phillips, R. J., editors, *Venus II*, Space Science Series, pages 295–324. University of Arizona Press.

Levenberg, K. (1944). A method for the solution of certain nonlinear problems in least squares. *Quart. Appl. Math.*, 2:164.

Lewis, J. S. (1997). *Physics and Chemistry of the Solar System.* Academic Press.

Lewis, J. S. and Grinspoon, D. H. (1990). Vertical Distribution of Water in the Atmosphere of Venus: A Simple Thermochemical Explanation. *Science*, 249:1273–1275.

Limaye, S. S. and Suomi, V. E. (1981). Cloud motions on Venus: Global structure and organisation. *J. Atmos. Sci.*, 38:1220–1235.

Ma, Q. and Tipping, R. H. (1992). A far wing line shape theory and its application to the water vibrational bands. *J. Chem. Phys.*, 96(12):8655–8663.

Ma, Q., Tipping, R. H., Boulet, C., and Bouanich, J.-P. (1999). Theoretical far-wing line shape and absorption for high-temperature CO_2. *Applied Optics*, 38:599–604.

Manatt, S. L. and Lane, A. L. (1993). A compilation of the absorption cross-sections of SO_2 from 106 to 403 nm. *J. Q. S. R. T.*, 50:267–276.

Marov, M. Y., Lystev, V. E., Lebedev, V. N., Lukashevich, N. L., and Shari, V. P. (1980). The structure and microphysical properties of the Venus Clouds: Venera 9, 10, and 11 data. *Icarus*, 44:608–638.

Marquardt, D. W. (1963). An algorithm for least-squares estimation of nonlinear parameters. *SIAM J. Appl. Math.*, 11:431.

Meadows, V. and Crisp, D. (1996). Ground-based near-infrared observations of the Venus nightside: The thermal structure and water abundance near the surface. *J. Geophys. Res.*, 60:4595–4622.

Mie, G. (1908). Beigrade zur optik trueber medienspeziell kolloidaler metalloesungen. *Ann. Physik.*, pages 377–445.

Moroz, V. I. (2002). Studies of the atmosphere of Venus by means of spacecraft: solved and unsolved problems. *Adv. Space Res.*, 29(2):215–225.

Moroz, V. I., Monshkin, B. E., Ekonomov, A. P., Golovin, Y. M., Gnedykh, V., and Grigor'ev, A. V. (1982). The Venera 13 and Venera 14 spectrophotometry experiments. *Soviet Astronomy Letters*, 8:404–410.

Moroz, V. I., Monshkin, B. E., Ekonomov, A. P., San'ko, N. F., Parfent'ev, N. A., and Golovin, Y. M. (1979a). Venera 11 and 12 descent-probe spectrophotometry: The Venus day side sky spectrum. *Soviet Astronomy Letters*, 5:118–121.

Moroz, V. I., Parfent'ev, N. A., and San'ko, N. F. (1979b). Spectrophotometric experiment on the Venera 11 and Venera 12 descent modules. 2. Analysis of Venera 11 spectra data by layer-addition method. *Cosmic Res.*, 17:601–614.

Moroz, V. I., Spankunch, D., Linkin, V. M., and collaborators. (1986). Venus spacecraft infrared radiance spectra and some aspects of their interpretation. *Applied Optics*, 25(10):1710–1719.

Moroz, V. I., Spankunch, D., Titov, D. V., Schafer, K., Dyachkov, A. V., Dohler, W., Zasova, L. V., Oertel, D., Linkin, V. M., and Nopirakowski, J. (1990). Water vapour and sulphur dioxide abundances at the Venus cloud tops from the Venera-15 infrared spectrometry data. *Adv. Space Res.*, 10:(5)77–(5)81.

Moskalenko, N. I. and Parzhin, S. N. (1981). Investigation of absorption spectra of carbon dioxide under high pressures. Proceedings of the 6th All Union symposium on the propagation of Laser Radiation in the Atmosphere (in Russian). *IOA SO AN SSSR*, pages 110–113. Tomsk.

Mukhin, L., Gel'man, B. G., Lamonov, N. I., Mel'nikov, V. V., Nenarokov, D. F., Okhotnikov, B. P., and Khokhlov, V. N. (1982). Venera 13 and Venera 14 gas-chromatography analysis of the Venus atmosphere composition. *Soviet Astronomy Letters*, 8:399–403.

Na, C. Y. and Esposito, L. W. (1997). Is disulphur monoxide a second absorber on Venus? *Icarus*, 125:364–368.

Na, C. Y., Esposito, L. W., and Skinner, T. E. (1990). International ultraviolet explorer observation of Venus SO_2 and SO. *J. Geophys. Res.*, 95(D6):7485–7491.

Newman, M., Schubert, G., Kliore, A. J., and Patel, I. R. (1984). Zonal winds in the Middle Atmosphere of Venus from Pioneer Venus Radio Occultation Data. *J. Atmos. Sci.*, 41(12):1901–1913.

Nicolet, M. (1989). Solar spectral irradiances with their diversity between 120 and 900 nm. *Plan. Space Sci.*, 37(10):1249–1289.

Niedziela, R. F., Norman, M. L., DeForest, C. L., Miller, R. E., and Worsnop, D. R. (1999). A temperature- and composition-dependent study of H_2SO_4 aerosol optical constants using Fourier Transform and Tunable Diode laser infrared spectroscopy. *J. Phys. Chem. A*, 103:8030–8040.

Oertel, D., Moroz, V. I., Nopirakowski, J., Linkin, V. M., Jahn, H., and collaborators (1990). The Venera 15 and 16 Infrared Experiment. I. Methodics and first results. *Verroeffentilichungen des Forschungbereicks Geo- und Kosmowissenschaften*, 18:9–26.

Owen, T. (1967). Water vapour on Venus - A Dissent and Clarification. *Astrophys. J.*, 150:121–123.

Oyama, V. I., Carle, G. C., Woeller, F., B., P. J., Reynolds, R. T., and Graig, R. A. (1980). Pioneer Venus Chromatography of the Lower Atmosphere of Venus. *J. Geophys. Res.*, 82(A13):7891–7902.

Palmer, K. F. and Williams, D. (1975). Optical constants of sulphuric acid: application to the clouds of Venus? *Applied Optics*, 14:208–219.

Phillips, R., Bullock, M. A., and Hauck, S. (2001). Climate and Interior Coupled Evolution on Venus. *Geophys. Res. Let.*, 28(9):1779–1782.

Pollack, J., Dalton, J. B., Grinspoon, D., Wattson, R., Freedman, R., Crisp, D., Allen, D., Bézard, B., de Bergh, C., Giver, L., Ma, Q., and Tipping, R. (1993). Near Infrared Light from Venus' Night side: A spectroscopic analysis. *Icarus*, 103:1–42.

Pollack, J. B., Toon, O. B., Whitten, R. C., Boese, R., Tomasko, M., Esposito, L., Travis, L., and Wiedman, D. (1980). Distribution and source of the UV absorption in Venus' atmosphere. *J. G. R.*, 85(A13):8141–8150.

Polyakov, A. V., Timofeev, Y. M., Tonkov, M. V., and Filippov, N. N. (1998). Effect of spectral line mixing on atmospheric transmission functions in CO_2 absorption bands. *Atmospheric and Oceanic Physics*, 34(3):318–327.

Press, W. H., Teukolksy, S., Vetterling, W. T., and Flannery, B. (1995). *Numerical Recipes: The Art of Scientific Computing.* Cambridge University Press.

Remsberg, E. E., Lavery, D., and Crawford Jr, B. (1974). Optical constants for Sulphuric and Nitric Acids. *J. Chem. End. Data*, 19(3):263–265.

Revercomb, H. E., Sromovsky, L. A., Suomi, V. E., and Boese, R. W. (1985). Net thermal radiation in the atmosphere of Venus. *Icarus*, 61:521–538.

Rodgers, C. D. (1976). Retrieval of atmospheric temperature and composition from remote measurements of thermal radiation. *Rev. Geophys. Space Phys.*, 14:609–624.

Rodgers, C. D. (1996). Optical Spectroscopic Techniques and Instrumentation for Atmospheric and Space Research II. In Hays, P. B. and Wang, J., editors, *SPIE*, volume 2830, pages 136–147.

Rodgers, C. D. (1998). Information content and optimisation of high spectral resolution remote measurements. *Adv. Space Res.*, 21(3):361–367.

Rodgers, C. D. (2000). *Inverse Methods for Atmospheric Sounding. Theory and Practise.* Word Scientific.

Roos-Serote, M., Drossart, P., Encrenaz, T., Lellouch, E., Carlson, R., Baines, K., Taylor, F. W., and Calcutt, S. (1995). The thermal structure and dynamics of the atmosphere of Venus between 70 and 90 km from the Galileo-NIMS spectra. *Icarus*, 114:300–309.

Rossow, W. B., Del Genio, A. D., Limaye, S. S., Travis, L. D., and Stone, P. H. (1980). Cloud morphology and motions from Pioneer Venus images. *J. Geophys. Res.*, 85:8107–8128.

Rothman, L. S. (1981). AFGL atmospheric absorption line parameters compilation: 1980 version. *Applied Optics*, 20:791–795.

Rothman, L. S., Gamache, R. R., Tipping, R. H., and collaborators (1992). The Hitran molecular database: Editions of 1991 and 1992. *J. Q. S. R. T.*, 48:469–507.

Rothman, L. S., Rinsland, C. P., Goldman, A., Massie, S. T., and collaborators. (1998). The Hitran molecular spectroscopic database and HAWKS (Hitran Atmospheric Workstation): 1996 edition. *J. Q. S. R. T.*, 60.

Salby, M. L. (1996). *Fundamentals of Atmospheric Physics.* Academic Press.

Schofield, J. and Taylor, F. W. (1982). Measurements of the mean, solar-fixed temperature and cloud structure of the middle atmosphere of Venus. *Q. J. R. M. S.*, 109:57–80.

Schofield, J., Taylor, F. W., and McCleese, D. (1983). The global distribution of water vapour in the middle atmosphere of Venus. *Icarus*, 52:263–278.

Schorn, R. A., Barker, E. S., Gray, L. D., and Moore, R. C. (1969). High-precision spectroscopic studies of Venus II. The water vapour variations. *Icarus*, 10:98–104.

Schubert, G. (1980). General circulation and the dynamical state of the Venus atmosphere. In Bougher, S. W., Hunten, D. M., and Phillips, R. J., editors, *Venus*, Space Science Series, pages 681–765. University of Arizona Press.

Seiff, A. (1983). Thermal Structure of the Atmosphere of Venus. In Bougher, S. W., Hunten, D. M., and Phillips, R. J., editors, *Venus*, Space Science Series, pages 215–279. University of Arizona Press.

Seiff, A., Kirk, D. B., Young, R. E., Blanchard, R. C., Findlay, J. T., Kelly, G. M., and Sommer, S. C. (1980). Measurements of thermal structure and thermal contrasts in the atmosphere of Venus and related dynamical observations: Results from the four Pioneer Venus probes. *J. Geophys. Res.*, 85:7903–7933.

Smith, W. L. (1970). Iterative solution of the radiative transfer equation for temperature and absorbing gas profile of an atmosphere. *Applied Optics*, 9:19393–1999.

Staley, D. O. (1970). The Adiabatic Lapse Rate in the Venus Atmosphere. *J. Atmos. Sci.*, 27:219–223.

Steele, H. M. and Hamill, P. (1981). Effects of temperature and humidity on the growth and optical properties of sulphuric acid-water droplets in the stratosphere. *J Aerosol Sci*, 12:517–528.

Strow, L. L. and Reuter, D. (1988). Effect of line mixing on atmospheric brightness temperatures near 15 μm. *Applied Optics*, 27.

Surkov, Y., Ivanova, V., Pudov, A., Pavlenko, V. A., Davydov, N. A., and Sheinin, D. (1982). Venera 13 and Venera 14 measurements of the water vapour content in the Venus atmosphere. *Soviet Astronomy Letters*, 8:411–413.

Surkov, Y., Shcheglov, O., Ryvkin, M., Davydov, N. A., Sheinin, D., and Zhitnikov, D. E. (1986). Vega 1, 2 humidity profiles for the Venus atmosphere. *Soviet Astronomy Letters*, 12:73–77.

Taylor, F. W. (1974). Remote Temperature Sounding in the Presence of Cloud by Zenith Scanning. *Applied Optics*, 13(7):1559–1566.

Taylor, F. W. (1975). Interpretation of Mariner 10 Infrared Observations of Venus. *J. Atmos. Sci.*, 32:1005–1017.

Taylor, F. W. (1988). *The Physics of the Planets*, chapter : The Dynamics of the Atmosphere of Venus, pages 143–159. John Wiley & Sons.

Taylor, F. W. (1997). *Encyclopedia of Planetary Sciences*, chapter Venus: Atmosphere, pages 890–895. Chapman and Hall.

Taylor, F. W. (2002). Some fundamental questions concerning the circulation of the atmosphere of Venus. *Adv. Space Res.*, 29(2):227–231.

Taylor, F. W., Beer, R., Chahine, M., Diner, D. J., Elson, L. S., Haskins, R., McCleese, D. J., Martonchik, J. V., Reichley, P., Bradley, S. E., Delderfield, J., Schofield, J. T., Farmer, C. B., Froidevaux, L., Leung, J., Gille, J. C., and Coffrey, M. T. (1980). Structure and meteorology of the middle atmosphere of Venus: Infrared remote sensing from the Pioneer Orbiter. *J. Geophys. Res.*, 85:7936–8006.

Taylor, F. W., Diner, D. J., Elson, L. S., Hanner, M. S., McCleese, D. J., Martonchik, J. V., Reichley, P., Houghton, J. T., Delderfield, J., Schofield, J. T., Bradley, S. E., and Ingersoll, A. P. (1979a). Infrared remote sounding of the middle atmosphere of Venus from the Pioneer Orbiter. *Science*, 203:779–781.

Taylor, F. W., Diner, D. J., Elson, L. S., McCleese, D. J., Martonchik, J. V., Delderfield, J., Bradley, S. E., Schofield, J. T., Gille, J. C., and Coffrey, M. T. (1979b). Temperature, cloud structure and dynamics of Venus middle atmosphere by infrared remote sensing from Pioneer Orbiter. *Science*, 205:65–67.

Taylor, F. W., Hunten, D. M., and Ksanfomality, L. V. (1983). The thermal balance of the middle and upper atmosphere of Venus. In Bougher, S. W., Hunten, D. M., and Phillips, R. J., editors, *Venus*, Space Science Series, pages 650–680. University of Arizona Press.

Taylor, F. W., Vescelus, F. E., Locke, J. R., Foster, P. B., Beer, R., Houghton, J. T., Delderfield, J., and Schofield, J. T. (1979c). Infrared radiometer for the Pioneer Venus Orbiter. 1. Instrument Description. *Applied Optics*, 18:3893–3900.

Tikhonov, A. N. (1963). On the solution of incorrectly stated problems and a method of regularisation. *Dokl. Acad. Nauk. SSSR*, 122:2530.

Tisdale, R. T., Glandorf, D. L., Toldert, M. A., and Toon, O. B. (1998). Infrared optical constants of low temperature H_2SO_4 solutions representative of stratospheric sulfate aerosols. *J. Geophys. Res.*, 103(D19):25353–25370.

Titov, D. V. (1995). Radiative Balance in the Mesosphere of Venus from the Venera 15 Infrared Spectrometer Results. *Adv. Space Res.*, 15(4):473–477.

Titov, D. V. and Haus, R. (1997). A fast and accurate method of calculation of gaseous transmission functions in planetary atmospheres. *Planet. Space Sci.*, 45(3):369–377.

Tobiska, W. K., Woods, T., Eparvier, F., Viereck, R., Floyd, L., Bouwer, D., Rottman, G., and White, O. R. (2000). The Solar2000 empirical solar irradiance model and forecast tool. *J. Atm. Solar Terr. Phys.*, 62:1233–1250.

Traub, W. A. and Carleton, N. P. (1975). Observations of O_2, H_2O and HD in planetary atmospheres. In Woszczyk, A. and Iwaniszewska, C., editors, *Exploration of the Planetary System*, pages 223–228. Dordrecht: Reidel.

Travis, L. D. (1978). Nature of the atmospheric dynamics on Venus from power spectrum analysis of Mariner 10 images. *J. Atmos. Sci.*, 35:1584–1595.

Twomey, S. (1963). On the numerical solution of Fredholm integral equation of the first kind by the inversion of the linear system produced by quadrature. *J. Ass. Comput. Mach.*, 10:97.

Twomey, S., Herman, B., and Rabinoff, R. (1977). An extension to the Chahine method of inverting the radiative transfer equation. *J. Atmos. Sci.*, 34:1085.

Ustinov, E. A. (1991). Inverse problem of thermal sensing: 3. Reconstructing the vertical profile of the mixing ratio of a minor gaseous component. *Kosmicheskie Issledovaniya*, 29(2):289–297.

Valdes, P. J. (1984). *Large scale waves in the atmosphere of Venus.* PhD thesis, Atmospheric Physics Department, Oxford University.

von Zahn, U., Kumar, S., Niemann, H., and Prinn, R. (1983). Composition of the Venus Atmosphere. In Bougher, S. W., Hunten, D. M., and Phillips, R. J., editors, *Venus*, Space Science Series, pages 299–430. University of Arizona Press.

Walterscheid, R. L., Schubert, G., Newmann, M., and Kliore, A. J. (1985). Zonal winds and the angular-momentum balance of Venus' Atmosphere within and above the clouds. *J. Atmos. Sci.*, 42(19):1982–1990.

Winick, J. R. and Stewart, I. F. (1980). Photochemistry of SO_2 in Venus' upper cloud layers. *J. Geophys. Res.*, 85:7849–7860.

Woo, R., Armstrong, W. J., and Kliore, A. J. (1982). Small-scale turbulence in the atmosphere of Venus. *Icarus*, 52:335–345.

Yamamoto, G., Tanaka, M., and Aoki, T. (1969). Rotational Line Widths of Carbon Dioxide Bands. *J.Q.R.S.T*, 9:371–382.

Yamamoto, M. and Tanaka, K. (1997). Formation and maintenance of the 4-day circulation in the Venus middle atmosphere. *J. Atmos. Sci.*, 54.

Young, L., Young, A., and Zasova, L. V. (1984). A new interpretation of the Venera 11 Spectra of Venus. The 0.94 μm water band. *Icarus*, 60:138–151.

Yung, Y. L. and DeMore, W. B. (1982). Photochemistry of the Stratosphere of Venus; Implications for Atmospheric Evolution. *Icarus*, 51:199–247.

Zasova, L. V., Khatountsev, I. A., Moroz, V. I., and Ignatiev, N. I. (1999). Structure of the Venus middle atmosphere: Venera 15 Fourier Spectrometry data revisited. *Adv. Space Res.*, 23(9):1559–1568.

Zasova, L. V., Krasnopolsky, V. A., and Moroz, V. I. (1981). Vertical distribution of SO_2 in upper cloud layer of Venus and origin of UV absorption. *Adv. Space. Res.*, 1:31.

Zasova, L. V., Moroz, V. I., Esposito, L. W., and Na, C. Y. (1993). SO_2 in the middle atmosphere of Venus: IR measurements from Venera 15 and comparison to UV data. *Icarus*, 105:92–109.

Zasova, L. V., Moroz, V. I., and Linkin, V. M. (1996). Venera-15,16 and VEGA mission results as sources for improvements of the Venus reference atmosphere. *Adv. Space Sci.*, 17:(11)171–(11)180.